SPIN TRANSPORT STUDIES IN GRAPHENE

JAYAKUMAR BALAKRISHNAN

DEPARTMENT OF PHYSICS

NATIONAL UNIVERSITY OF SINGAPORE

(2013)

SPIN TRANSPORT STUDIES IN GRAPHENE

JAYAKUMAR BALAKRISHNAN

(*M.Sc. Physics, Indian Institute of Technology Madras*)

A THESIS SUBMITTED

FOR THE DEGREE OF DOCTOR OF PHILOSOPHY

DEPARTMENT OF PHYSICS

NATIONAL UNIVERSITY OF SINGAPORE

(2013)

DECLARATION

I hereby declare that the thesis is my original work and it has been written by me in its entirety. I have duly acknowledged all the sources of information which have been used in the thesis.

This thesis has also not been submitted for any degree in any university previously.

Jayakumar Balakrishnan

ACKNOWLEDGEMENTS

I would like to thank Prof. Barbaros Özyilmaz, my supervisor, for his patient guidance and constant support throughout the duration of my research. Working in his group is a wonderful experience that will keep me motivated for the years to come. I would like to sincerely thank all my '*Gurus*', whose blessings have helped me to reach this memorable phase in life.

I am also grateful to Dr. Zheng Yi, Dr. Xu Xiangfan and Dr. Manu Jaiswal for their support and guidance during the early years of chaos and confusion. More importantly, I owe them my gratitude for making me understand the importance of the minute details and tricks while performing low temperature transport measurements. I am also grateful to Prof. A. H. Castro Neto, Prof. M. A. Cazalilla and Dr. Aires Ferreira for the stimulating discussions and theoretical help.

My sincere thanks to Mr. Gavin Kok Wai Koon, Mr. Ahmet Avsar and Mr. Yuda Ho; whose constant support has made this work possible and helped me to achieve the goals set for my Ph.D. I would also like to thank Prof. Gernot Güntherodt, Prof. Bernd Beschoten, Dr. Mihaita Popinciuc, Mr. Frank Volmer and Mr. Tsung-Yeh Yang from the RWTH AACHEN University for their help in the fabrication and characterization of spin-valve devices during the initial stages of my work.

I also thank my colleagues Dr. Ni GuangXin, Dr. Zeng Minggang, Dr. Xie Lanfei, Dr. Surajit Saha, Dr. Ajit Patra, Ms. Zhang Kaiwen, Mr. Zhao Xiangming, Mr. Orhan Kahya, Mr. Alexandre Pachoud, Mr. Toh Chee Tat, Mr. Henrik Anderson, Mr. Wu Jing, Mr. Jun Yu, Dr. Ajay Soni, Mr. Ibrahim Nor, Mr. Zhang Shujie, Mr. Ang Han Siong, Dr. Raghu, Dr. J. H. Lee and all other members of the lab, who were all there at each phase and have constantly helped me during my research works. I would like to have a special mention of *late* Mr. Tan, our workshop manager, who was always there to help us with a gentle smile.

I would also like to thank my friends Ram Sevak, Vinayak, Suresh, Pranjal, KMG, Sumit, Ashwini, Manoj, Vaibhav, Amar and all others who have made my stay in Singapore a memorable one. Finally, I would like to thank my parents, my sister and my brother-in-law, who have always backed me with my decisions and encouraged me to follow my dreams, without which I would never have reached this point in life.

Table of Contents

Abstract

The work described in this thesis is an attempt to understand the spin transport properties of graphene - the weakly spin-orbit coupled two dimensional allotrope of carbon. In the first half of the thesis we make an effort to understand the spin relaxation mechanisms in monolayer and bilayer graphene. For this, four-terminal spin valve devices are characterized in the non-local geometry and a correlation between the charge and spin parameters has been drawn. Our systematic analysis shows that, unlike monolayer graphene where the spin relaxation is due to a direct consequence of momentum scattering, in bilayer graphene the spin dephasing occurs due to the precession of spins under the influence of local spin-orbit fields between momentum scattering. The role of intrinsic and extrinsic factors that could lead to such contrasting results is discussed.

The second half of the thesis focuses on enhancing the spin-orbit interaction in graphene by introducing adatoms. Our pioneering experiments in graphene samples decorated with adatoms, demonstrate a three orders of magnitude increase in spin-orbit interaction strength while preserving the unique transport properties of intrinsic graphene. In such samples, we realize for the first time room-temperature non-local spin Hall effect at zero applied magnetic fields. Moreover, the methods employed for the introduction of adatoms, specifically the metallic adatoms, in graphene can easily be generalized for any metal, and would thus allow for the future realization of a graphene-based two dimensional topological insulator state.

List of Figures

List of Tables

Chapter 1

Introduction

The development of quantum mechanics in the early half of the twentieth century has enabled a deeper understanding of the fundamental particles that constitute matter. The electrons, the first understood elementary particle, with a negative elementary electric charge and half-integer intrinsic angular momentum (spin) plays an important role in the current technological developments. Depending on the fundamental property which is being manipulated, two closely related but independent fields have emerged: (1) electronics, where the charge of electron is manipulated for logical operations and transistor functionalities and (2) spintronics, where the electron's intrinsic angular momentum, called spin, is manipulated. The electron's spin angular momentum (in units of $\hbar$) can have two values of 1/2 (spin-up) or -1/2 (spin-down) when placed in a magnetic field, allowing binary logical operations. The aim of this chapter is to give a short introduction on the developments in the emerging field of spintronics. At the end of the chapter an outline of this thesis with short summaries on each chapter is provided.

1.1 Spintronics: an overview

Spintronics [1] refers to the study of the electrical, optical and magnetic properties of materials, due to the presence of non-equilibrium spin populations. In a broader sense, spintronics is the study of spin phenomena like spin-orbit, hyperfine and/or exchange interactions. Such insights into spin interactions allow us to learn more about the fundamental processes leading to spin relaxation and/or spin dephasing in metals, semiconductors and semiconductor heterostructures [2].

The first observations of the effects of electron spins on the charge transport can be dated back to 1857 [3, 4], even before the discovery of electrons (J.J. Thomson 1897). The observation that the resistance of the ferromagnet relies on the relative angle between the charge current direction and the magnetization direction in the ferromagnet [3, 4], termed as the anisotropic magneto resistance (AMR), has since been an important topic of study [5, 6]. After the discovery of electrons in 1897 and the development of quantum mechanics in the early half of the 20th century [7], the fundamental studies in understanding the puzzling observations in the line spectra of atoms led to the proposal of an intrinsic angular momentum for electrons by Uhlenbeck and Goudsmit in 1925 [8, 9]. This intrinsic angular momentum, known as spin interacts with magnetic field and attains quantized values of 1/2 or -1/2. Since these quantized values of 1/2 or -1/2 can be used in a similar way to the Boolean logical operations based on binary numbers 0 and 1, a new field where the spin degree of freedom of electron is utilized for the realization of spin based electronic applications has emerged [1, 2, 10–12]. The potential applications of spintronics range from spin field effect transistors [13], magnetic random access memories [14], spin-based light

emitting diodes (LED's) [15] to topological quantum computations [10]. However, an effective utilization of the spins for information processing requires three important criteria to be satisfied: (1) the injection of spin polarized current into the material of interest, metals, semiconductors etc., (2) an ideal material with a long spin relaxation length in which the injected spins can diffuse, and (3) a detector for the spins [2].

One of the first realistic proposals for the injection of spins came from Aronov and Pikus in 1976 where they proposed the electrical spin injection as a method to create non-equilibrium spin population in non-magnetic materials [16, 17]. Experimentally the electrical spin injection in metals was realized by Johnson and Silsbee in 1985 in single crystal aluminum [18–20]. However, until 1988 the field of spintronics remained of interest for fundamental studies only. In 1988-89 two groups led by Albert Fert in France and Peter Grünberg in Germany(Nobel Prize in Physics 2007) discovered the giant magnetoresistance in a ferromagnet/metal/ferromagnet heterostructure [21–25]. It was shown that the relative orientation of the magnetization in the ferromagnetic layers determined the electrical resistance of the heterostructure. The change in the resistance between parallel and anti-parallel configurations of the magnetization in the ferromagnetic layers could be greater than 100%; hence the name giant magneto resistance (GMR). These discoveries were later followed by the demonstration of GMR-based magnetic read heads in commercially available hard drives. The GMR-based magnetic read head is one of the first and foremost applications of spintronics till date.

The discovery of the GMR also triggered the renewed interest for new spin-dependent electron transport in metals as well as in semiconductor heterostructures. Notable

among these phenomena were (1) the tunneling magneto resistance (TMR) in magnetic tunnel junctions [26–28], (2) the electrical injection of spins into a non-magnetic medium (metals and semi-conductors) employing a four terminal non-local lateral spin-valve geometry [29–32], and (3) the creation of non-equilibrium spin population in metals and semi-conductors by the spin Hall and inverse spin Hall effects [33–36]. Specifically, the spin transport in semiconductors attracted much attention due to their unique properties such as the presence of a band gap which allows the injection and detection of spins via optical means. For instance, the experimental demonstration of the spin Hall effect was first reported in GaAs semiconductor by spatially resolving the Kerr rotation of the reflected light from the samples [35]. However, a demerit of the semiconductor and metal spintronics is the low spin relaxation length of charge carriers due to the enhanced spin-flip scattering induced by the high spin-orbit coupling strength. This calls for new materials where the spin-orbit coupling can be manipulated with minimal compensation of the spin relaxation length.

An ideal source of materials which could allow such long spin relaxation length are the organic conductors like carbon nanotubes [37] and graphene [6]. Carbon being a light element ($Z = 6$), the intrinsic spin-orbit coupling ($\propto Z^4$) is weak and hence the dominant spin dephasing mechanism due to spin-orbit coupling is also weak [39]. This allows fora spin relaxation length of the order of 100μm in these materials [40, 41]. Moreover, it is also easy to functionalize these carbon-based materials with reactive elements like hydrogen and fluorine [42] and also by metallic adatoms [43]. Such controlled additions of adatoms are predicted to enhance the spin-orbit coupling in graphene without affecting its long spin relaxation length. In this thesis I will discuss our recent results in understanding the spin transport properties of graphene and

functionalized graphene.

1.2 Thesis Outline

The main focus of this thesis is to understand and study the spin transport properties in the newly discovered perfect 2D material "Graphene" and its chemically/physically functionalized derivatives. For this, we first utilize the non-local spin-valve geometry with a Ferromagnet (Co)/Tunneling barrier (MgO)/Graphene/Tunnel barrier(MgO)/ Ferromagnet (Co) structure. The aim of these studies are to understand and contrast the fundamental spin relaxation/scattering mechanisms in single- and bi-layer graphene. As a next step we manipulate the electron spins in graphene via the spin Hall effect. Besides being of interest from a fundamental physics perspective, this technique will also allow the transport and detection of spins without the need for any magnetic elements. This is of utmost importance for future applications since it allows manipulation of spins by the simple application of a voltage. However, due to the low spin-orbit coupling of carbon atoms, this effect is feasible only at ultra-low temperatures in graphene and necessitates new methods to enhance the spin-orbit coupling in graphene.

Among the different approaches proposed, the decoration of graphene with adatoms holds a lot of promise. Here, the graphene spin-orbit coupling can be enhanced in two different ways: (1) by chemical functionalization of graphene with adatoms like hydrogen and fluorine [44] and (2) by the introduction of metallic adatoms like copper (Cu) or gold (Au) which due to its proximity to the graphene lattice allows electron tunneling from graphene to the adatoms and back resulting in a local enhancement of

the spin-orbit coupling strength [43]. Our aim in this work will be to see the predicted enhancement in spin-orbit coupling in graphene by the introduction of adatoms. For this we take hydrogen, gold and copper as the model systems. A brief outline for the individual chapter in this thesis is given below:

Chapter 2: The basic concepts essential for understanding the spin transport in non-magnetic materials is introduced. The chapter will focus on the theoretical background required for understanding the non-local spin transport measurements in the conventional lateral spin-valve geometry. This will be followed by an introduction to the spin Hall and inverse spin Hall effects. After discussing these basic spin transport theory, a brief introduction to graphene and graphene spintronics is provided.

Chapter 3: This chapter will focus on the basic experimental techniques required to perform the spin transport measurement in the spin-valve as well as in the spin Hall geometry. This includes graphene sample preparation, identification of single and bi-layer graphene, device fabrication and characterization.

Chapter 4: The experimental results on the spin transport in graphene spin-valves are discussed. The main focus of this chapter will be to differentiate the spin transport in single- and bi-layer graphene with emphasis given to identify the dominant spin scattering mechanism in bilayer graphene.

Chapter 5: This chapter discusses the controlled functionalization of graphene with adatoms like hydrogen to enhance the otherwise weak spin-orbit coupling in graphene by the conversion of the sp^2 to sp^3 hybridization of the graphene lattice. Such enhancement of the spin-orbit coupling is experimentally confirmed by demonstrating room temperature spin Hall effect.

Chapter 6: Similar to hydrogenation, the spin-orbit coupling in graphene can also be enhanced by introducing metallic adatoms like copper (Cu), gold (Au) or silver (Ag). In this chapter, our present efforts towards the enhancement of graphene's spin-orbit strength by metal decoration will be discussed.

Chapter 7: The conclusion and future perspectives of the work presented in this thesis will be discussed.

Bibliography

[1] S. A. Wolf, D. D. Awschalom, R. A. Buhrmann, J. M. Daughton, S. von Molnár, M. L. Roukes, A. Y. Chtchelkanova, and D. M. Treger, Science **294**, 1488 (2001).

[2] J. Fabian, A. Matos-Abiague, C. Ertler, P. Stano, I. Zutic, Acta Physica Slovaca **57**, 565 (2007).

[3] W. Thomson, Philos. Trans. R. Soc. London **146**,649 (1856).

[4] W. Thomson, Proc. R. Soc. **8**, 546 (1857).

[5] J. Smit, Physica **16**, 612 (1951).

[6] T. G. S. M. Rijks, R. Coehoorn, M. M. de Jong, and W. J. M. de Jonge, Phys. Rev. B **51**, 283 (1995).

[7] P. A. M. Dirac. *The Principles of Quantum Mechanics*, Oxford University Press (1958).

[8] G. Uhlenbeck and S. Goudsmit, Naturwissenschaften **47**, 264 (1925).

[9] G. Uhlenbeck and S. Goudsmit, Nature **117**, 264 (1926).

[10] D. D. Awschalom, D. Loss, and N. Samarth, *Semiconductor Spintronics and Quantum Computation*, Springer Verlag, Berlin (2002).

[11] G. A. Prinz, Science **282**, 1660 (1998).

[12] I. Zutic, Journal of Superconductivity **15**, 5 (2002).

[13] S. Datta and B. Das, Appl. Phys. Lett. **56**, 665 (1990).

[14] J. Akerman, Science **308**, 508 (2005).

[15] V. F. Motsnyi, J. De Boeck, J. Das, W. Van Roy, G. Borghs, and V. I. Safarov, Appl. Phys. Lett. **81**, 265 (2002).

[16] A. G. Aronov and G. E. Pikus, Fiz. Tech. Poluprovdn. **10**, 1177 (1976).

[17] E. I. Rashba, Journal of Superconductivity **15**, 13(2002).

[18] M. Johnson and R. H. Silsbee, Phys. Rev. Lett. **55**, 1790 (1985).

[19] M. Johnson and R. H. Silsbee, Phys. Rev. B **37**, 5312 (1988).

[20] M. Johnson and R. H. Silsbee, Phys. Rev. B **37**, 5326 (1988).

[21] M. N. Baibich, J. M. Broto, A. Fert, F. N. V. Dau, F. Petroff, P. Etienne, G. Creuzet, A. Friedrich, and J. Chazelas, Phys. Rev. Lett. **61**, 2472 (1988).

[22] G. Binash, P. Grünberg, F. Saurenbach, and W. Zinn, Phys. Rev. B **39**, 4828 (1989).

[23] M. A. M. Gijs and G. E. W. Bauer, Advances in Physics **46**, 285 (1997).

[24] J. -P. Ansermet, J. Phys.:Condens. Matter **10**, 6027 (1998).

[25] J. Bass and W. P. Pratt Jr., J. Mag. Magn. Mater. **200**, 274 (1999).

[26] R. Meservey, P. M. Tedrow and P. Flude, Phys. Rev. Lett. **25**, 1270 (1970).

[27] R. Meservey and P. M. Tedrow, Physics Reports **238**, 173 (1994).

[28] P. Flude, Adv. Phys. **22**, 667 (1973).

[29] F. J. Jedema, A. T. Filip, and B. J. van Wees, Nature **410**, 345 (2001).

[30] F. J. Jedema, H. B. Heersche, A. T. Filip, J. J. A. Baselmans and B. J. van Wees, Nature **416**, 713 (2002).

[31] F. J. Jedema, M. S. Nijboer, A. T. Filip and B. J. van Wees, Phys. Rev. B **67**, 85319 (2003).

[32] N. Tombros, S. J. vab der Molen and B. J. van Wees, Phys. Rev. B **73**, 233403 (2006).

[33] M. I. Dyakonov and V. I. Perel, Phys. Lett. A **35**, 459 (1971).

[34] J. E. HIrsch, Phys. Rev. Lett. **83**, 1834-1837 (1999).

[35] Y. K. Kato, R. C. Myers, A. C. Gossard and D. D. Awschalom, Science **306**, 1910 (2004).

[36] J. Wunderlich, B. Kaestner, J. Sinova and T. Jungwirth, Phys. Rev. Lett. **94**, 047204 (2005).

[37] S. Iijima, Nature **354**, 56 (1991).

[38] K. S. Novoselov, A. K. Geim, S. V. Morozov, D. Jiang, Y. Zhang, S. V. Dubonos, I. V. Grigorieva, A. S. Firsov, Science **306**, 666 (2004).

[39] I. Zutic, J. Fabian, and S. Das Sarma, Rev. Mod. Phys. **76**, 323 (2004).

[40] L. E. Hueso, J. M. Pruneda, V. Ferrari, G. Brunell, J. P. Valdes-Herera, B. D. Simons, P. B. Littlewood, E. Artacho, A. Fert and N. D. Mathur, Nature **445**, 410 (2007).

[41] B. Dlubak, M.-B. Martin, C. Deranlot, B. Servet, S. Xavier, R. Mattana, M. Sprinkle, C. Berger, W. A. De Heer, F. Petroff, A. Anane, P. Seneor and A. Fert, Nat. Phys. **8**, 557 (2012).

[42] K. P. Loh, Q. L. Bao, P. K. Ang, J. X. Yang, J. Mater. Chem **20**, 2277 (2010).

[43] W. Conan, H. Jun, A. Jason, F. Marcel, and W. Ruqian, Phys. Rev. X **1**, 021001 (2011).

[44] A. H. Castro Neto and F. Guinea, Phys. Rev. Lett. **103**, 026804 (2009).

Chapter 2

Basic Concepts and Theory

2.1 Introduction

In this chapter a brief discussion on the basic theory of electrical spin injection and detection will be discussed. The main emphasis of this chapter will be the spin transport in the diffusive regime where the Boltzmann transport formalism is applicable. Since the focus of this thesis is on the spin transport in graphene in the diffusive regime, the basic properties of graphene that are relevant for the presented study will also be discussed. The following works were consulted extensively and used as a guide for the preparation of this chapter: (1) Jedema, PhD thesis [1], (2) N. Tombros PhD thesis [2], (3) I. Zutic "Spintronics: Fundamentals and applications" [3], (4) J. Fabian "Semiconductor spintronics" [4] and (5) A. H. Castro Neto "The electronic properties of graphene" [5].

2.2 Spin transport: Basic theory

In metals and semiconductors the electrons undergo scattering due to the presence of disorder, impurities or phonons. The resultant motion of electrons is equivalent to a random walk problem in one dimensions [4]. The relation between the resultant average velocity of the electrons to the applied electric field and system parameters like the mean free path and average scattering time (momentum relaxation time) is obtained in the standard Drude formalism [6]. Here, our aim is to review a similar theoretical formalism for the spins within the diffusive transport framework [4]. For this, consider a system with an electron density n such that $n_\uparrow$ is the density of spin-up electrons and $n_\downarrow$ is the density of spin-down electrons, then

$$n = n_\uparrow + n_\downarrow \tag{2.2.1}$$

while the spin density s is given by

$$s = n_\uparrow - n_\downarrow \tag{2.2.2}$$

In the diffusive regime the spin-up and spin-down electrons can also be considered to be performing random walks due to collisions. In such scattering process the spins are allowed to flip (spin-up to spin-down or vice-a-versa) and if f is the probability that a spin flips in the time τ, then the spin flip rate is f/τ. Now to understand the time evolution of the density of the spin states, let us assume that at time t and at position x, the density of spin-up electrons $n_\uparrow(x,t)$ is given by the densities at x-l and x+l in the time interval t-τ. If p_+ and p_- are the probabilities for the spin-flip process at x-l and x+l, the spin-up density around (x,t) is

$$\begin{aligned} n_\uparrow(x,t) = n_\uparrow(x-l,t-\tau)(1-f)p_+ + n_\uparrow(x+l,t-\tau)(1-f)p_- \\ +n_\downarrow(x-l,t-\tau)fp_+ + n_\downarrow(x+l,t-\tau)fp_- \end{aligned} \tag{2.2.3}$$

Taylor expansion of the equation (2.2.3) around (*x,t*) for infinitesimal l and τ by retaining terms up to $O(l^2)$ and $O(\tau)$ gives,

$$\begin{aligned} n_\uparrow(x,t) = n_\uparrow(x,t)(1-f)p_+ - l(1-f)\frac{\partial n_\uparrow}{\partial x}p_+ + \frac{1}{2}l^2(1-f)\frac{\partial^2 n_\uparrow}{\partial x^2}p_+ \\ -\tau(1-f)\frac{\partial n_\uparrow}{\partial t}p_+ + n_\uparrow(x,t)(1-f)p_- + l(1-f)\frac{\partial n_\uparrow}{\partial x}p_- \\ +\frac{1}{2}l^2(1-f)\frac{\partial^2 n_\uparrow}{\partial x^2}p_- - \tau(1-f)\frac{\partial n_\uparrow}{\partial t}p_- + n_\downarrow(x,t)fp_+ \\ -lf\frac{\partial n_\downarrow}{\partial x}p_+ + \frac{1}{2}l^2 f\frac{\partial^2 n_\downarrow}{\partial x^2}p_+ - \tau\frac{\partial n_\downarrow}{\partial t}p_+ + n_\downarrow(x,t)fp_- \\ +lf\frac{\partial n_\downarrow}{\partial x}p_- + \frac{1}{2}l^2 f\frac{\partial^2 n_\downarrow}{\partial x^2}p_- - \tau\frac{\partial n_\downarrow}{\partial t}p_- \end{aligned} \tag{2.2.4}$$

The actual spin flip probability within the time limit τ is of the order of 10^{-6}, *i.e.*, $f << 1$. Also $p_+ + p_- = 1$ and $p_+ - p_- = \Delta p$. Substituting these conditions into equation (2.2.4) gives the relation for the spin-up density at (*x,t*) as

$$n_\uparrow(x,t) = n_\uparrow(x,t)(1-f) - l\Delta p\frac{\partial n_\uparrow}{\partial x} + \frac{1}{2}l^2\frac{\partial^2 n_\uparrow}{\partial x^2} - \tau\frac{\partial n_\uparrow}{\partial t} + n_\downarrow f \tag{2.2.5}$$

The drift-diffusion equation for $n_\uparrow$ can thus be rewritten as

$$\frac{\partial n_\uparrow}{\partial t} = \frac{1}{2}\frac{l^2}{\tau}\frac{\partial^2 n_\uparrow}{\partial x^2} - \frac{l}{\tau}\frac{\partial n_\uparrow}{\partial x} - \frac{f}{\tau}(n_\uparrow - n_\downarrow) \tag{2.2.6}$$

Similarly for $n_\downarrow$

$$\frac{\partial n_\downarrow}{\partial t} = \frac{1}{2}\frac{l^2}{\tau}\frac{\partial^2 n_\downarrow}{\partial x^2} - \frac{l}{\tau}\frac{\partial n_\downarrow}{\partial x} - \frac{f}{\tau}(n_\downarrow - n_\uparrow) \tag{2.2.7}$$

Since the total spin density $s = n_\uparrow - n_\downarrow$, subtracting equations (2.2.6) and (2.2.7) gives the spin diffusion equation for s

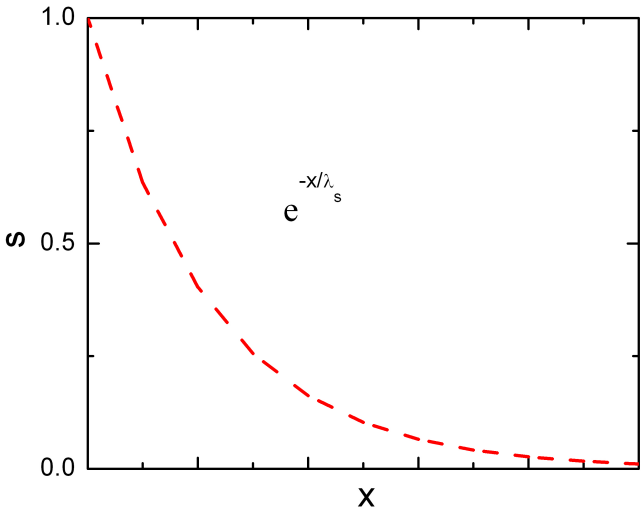

Figure 2.1: Decay of the spin density s as a function of the position x. Here at $x = 0$ the spin density is normalized to 1 and as the distance increases from $x = 0$ the spins start to decay with a characteristic length scale λ_s

$$\frac{\partial s}{\partial t} = D\frac{\partial^2 s}{\partial x^2} - v_d\frac{\partial s}{\partial x} - \frac{s}{\tau_s} \tag{2.2.8}$$

where $D = \frac{1}{2}\frac{l^2}{\tau}$ is the diffusion coefficient, $v_d = \frac{l}{\tau} = \mu E$ is the drift velocity of electrons in applied electric field E, μ is the mobility of the charge carriers, and $\frac{1}{\tau_s} = \frac{2f}{\tau}$ is the spin relaxation/dephasing length. Since our focus is on the diffusion of spins in a medium, the spin drift-diffusion equation (2.2.8) can be solved by neglecting the drift term.

2.2.1 Spin diffusion without drift

The spin diffusion equation (2.2.8) neglecting the drift term is given by

$$\frac{\partial s}{\partial t} = D\frac{\partial^2 s}{\partial x^2} - \frac{s}{\tau_s} \tag{2.2.9}$$

Now at time t=0 the spin density s at (x,t) =(x,0) is given by

$$s(x,0) = S_0\delta(x) \tag{2.2.10}$$

where S_0 is the total spin density at t=0. In the steady state, i.e. $\frac{\partial s}{\partial t} = 0$, the solution to equation (2.2.9) gives

$$\begin{aligned} D\frac{\partial^2 s}{\partial x^2} &= \frac{s}{\tau_s} \\ s(x) &= s_0 e^{-\frac{x}{\lambda_s}} \end{aligned} \tag{2.2.11}$$

where λ_s is the spin relaxation length defined as $\sqrt{D\tau_s}$, and clearly shows that the spin density decays exponentially with x with the characteristic length scale λ_s. The length scale λ_s tells us how far an electron spin can travel in the medium before its initial spin direction gets randomized.

2.3 Spin injection and detection via non-local spin valves

In the previous section we have seen that in the diffusive transport regime the spin density decays exponentially with the characteristic length scale given by its spin relaxation length λ_s. In this section, we will review how such a spin density can be introduced and detected in a non-magnetic material by electrical transport measurements.

2.3.1 Electrical spin injection into a non-magnetic material

By the electrical spin injection we mean the creation of non-equilibrium population of up and down spins in the material. This can be achieved by the introduction of a ferromagnetic material as the source of the spins, since in a ferromagnet due to exchange splitting [7,8], the density of states as well as the Fermi velocity for the spin-up and spin-down sub-bands become different. This results in different conductivities for the spin-up and spin-down electrons and hence in the generation of spin polarized current $j_{\uparrow,\downarrow}$, [9–15]

$$j_{\uparrow,\downarrow} = \frac{\sigma_{\uparrow,\downarrow}\partial\mu_{\uparrow,\downarrow}}{e\partial x} \tag{2.3.1}$$

where $\sigma_{\uparrow,\downarrow} = e^2 N_{\uparrow,\downarrow} D_{\uparrow,\downarrow}$ is the spin up and spin down conductivity, e is the electric charge, $\mathrm{N}_{\uparrow,\downarrow}$ is the spin dependent density of states at the Fermi energy and $\mathrm{D}_{\uparrow,\downarrow} = \frac{1}{3} v_{F\uparrow,\downarrow} l_{e\uparrow,\downarrow}$ is the spin dependent diffusion coefficient with Fermi velocity $v_{F\uparrow,\downarrow}$ and electron mean free path $l_{e\uparrow,\downarrow}$ for spin-up and spin down electrons and $\mu_{\uparrow,\downarrow}$ is the electrochemical potential of the spin species defined as

$$\mu = \mu_{ch} - eV \tag{2.3.2}$$

Here, μ_{ch} is the chemical potential which by definition is the energy needed to add one electron to the system and accounts for the kinetic energy of the electrons, and eV is the potential energy the electrons experience due to an electric field E. Since the spin-up and spin down current and conductivities are different, the bulk spin polarization in the ferromagnet can be defined as

$$P = \frac{\sigma_\uparrow - \sigma_\downarrow}{\sigma_\uparrow + \sigma_\downarrow} = \frac{j_\uparrow - j_\downarrow}{j_\uparrow + j_\downarrow} \tag{2.3.3}$$

where $j_\uparrow - j_\downarrow = j_s$ is the spin current, $j_\uparrow + j_\downarrow = j$ is the total charge current and

$\sigma_\uparrow + \sigma_\downarrow = \sigma$ is the total conductivity. The relation for the spin current equation (2.3.1) can now be rewritten as

$$j_\uparrow = (1+P)\frac{\sigma \partial \mu_\uparrow}{2e\partial x} \tag{2.3.4}$$

and

$$j_\downarrow = (1-P)\frac{\sigma \partial \mu_\downarrow}{2e\partial x} \tag{2.3.5}$$

From the above relations, it is clear that the variation in the electrochemical potential of the up and down spins would result in the generation of a spin polarized current and this can be achieved either by varying the density of spin polarized electrons (∇n) or by the application of an electric field E=-∇V.

2.3.2 Detection of the decaying spins

As discussed, in a diffusive material, the injected spin decay exponentially with a characteristic length scale given by the spin relaxation length λ_s and time scale given by the spin relaxation time τ_s. The first electrical detection scheme based on spin-charge coupling was proposed by Johnson and Silsbee [16]. In a spin-charge coupling a non-magnetic material with non-equilibrium spin population when in contact with a ferromagnet produces electrical current, thus allowing the electrical detection of spins. A second method is to use optical methods where spin polarized electrons recombine with the unpolarized holes to emit circularly polarized light. The spins can also be detected by using the spin-valve effect [17]. In the spin-valve effect, the injected spins from the ferromagnet electrode into the non-magnetic material can be detected by using a second ferromagnet. Here, the relative orientation of magnetization of the injector and detector ferromagnetic electrodes is important for the reliable detection

of the diffusing spins.

2.3.2.1 Detection of spins by spin-valve effect:

A simple spin-valve geometry consists of two ferromagnetic electrodes in contact with a non-magnetic material (see figure 2.2(a)). Initially the magnetizations of both the ferromagnetic electrodes are aligned parallel to each other. When an electric current is passed through the ferromagnet, spins are injected into the non-magnetic material which diffuse following the decay equation (2.2.11) for spins towards the second ferromagnet. Now a parallel magnetic field is swept across the sample such that the magnetization of one of the ferromagnetic electrodes switches direction. To make sure that only one of the electrodes switches the magnetization first, we design the electrodes with different widths so that the switching fields are different, since $B_c \propto 1/w$, where B_c is the switching field and w is the width of the electrodes. For simplicity, let us assume the magnetization of the detector electrode has switched to the opposite direction. Now the diffusing spin reaching the detector electrode will see a higher resistance due to the magnetization switching resulting in a change in the chemical potential of the second ferromagnetic electrode. This change in the chemical potential will be measured change in resistance which will be proportional to the spin accumulation underneath the ferromagnetic electrode. This method, thus, gives a direct measure of the spin accumulation in the non-magnetic medium. However, in the two terminal spin-valve measurements since the charge current and spin current flow in the same direction, sometimes the spin signal gets overshadowed by spurious effects like the Hall effects, anisotropic magnetoresistance [18], interference effects [19] and magneto-coulomb effects [20, 21]. These effects could also mimic the spin signal and it becomes difficult to separate the spin accumulation signal from the spurious signals.

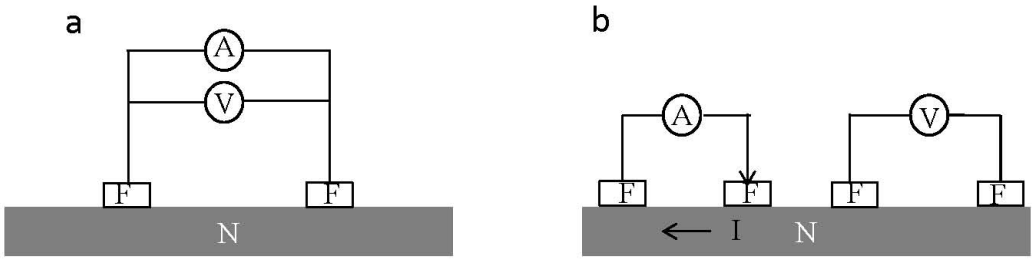

Figure 2.2: Measurement schematics for (a) a two terminal spin-valve device and (b) a four terminal non-local spin-valve device. The current and voltage probes are marked in the schematics.

2.3.3 Four terminal non-local spin-valve geometry

In order to separate any contribution from the charge current flow to the measured spin signal, Jedema *et al.* [22], introduced the four terminal non-local spin-valve geometry. In the non-local spin-valve geometry the charge current path is separated from the spin current path, thus enabling the detection of pure spin currents. Figure 2.2(b) shows a typical non-local spin-valve device with the measurement configuration. Here, among the four electrodes at least the two centre electrodes should be ferromagnetic with different widths so that the switching fields for these electrodes are different. The spin-valve devices presented in this thesis, however, have all the four electrodes as ferromagnets but with different widths. As shown in the figure 2.2(b), the charge current is passed between the first two ferromagnetic electrodes while the non-local signal is measured across the third and fourth electrodes marked with symbol V. A typical non-local signal measured for a graphene based non-local spin-valve is shown in figure 2.3

However, this simple non-local geometry works only when the contact resistance(R_c) of the ferromagnet-non-magnetic material (F/N) interface is much less than the resistance of the non-magnetic medium (R_N) and that of the ferromagnet (R_F) and both

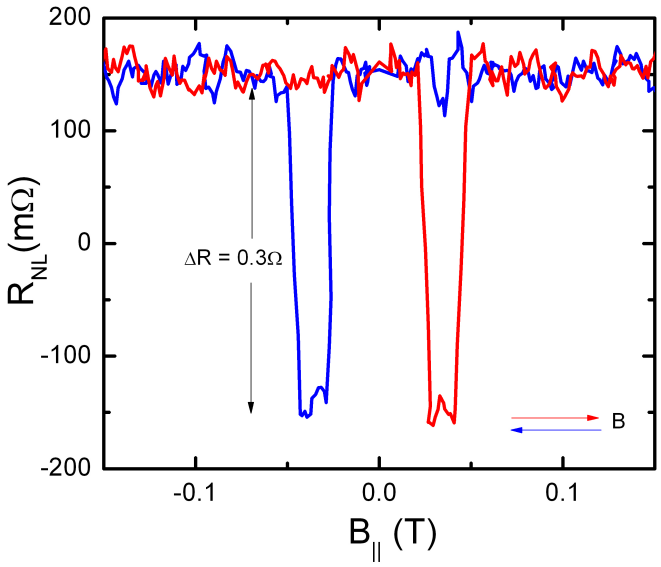

Figure 2.3: A typical non-local signal measured for a graphene based spin-valve.

the non-magnetic medium and the ferromagnet have comparable resistances.i.e.

$$R_c << R_N, R_F \tag{2.3.6}$$

and

$$R_N \approx R_F \tag{2.3.7}$$

For this condition, the spin injection efficiency P_j given by

$$P_j = \frac{R_F}{R_N + R_F} P_{\sigma F} \approx P_{\sigma F} \tag{2.3.8}$$

is high and comparable to the bulk polarization of the ferromagnet.

2.3.4 Conductivity mismatch and tunnel barriers

In the previous section, we saw that for the effective spin injection and detection in the spin-valve geometry depends on two important factors: (1) the relative magnitude of the interface resistance to that of the resistance of the ferromagnet and the non-magnetic medium and (2) on the relative magnitude of the ferromagnet and non-magnet resistance (conductance). In general, the conductance/conductivity of the ferromagnet and the non-magnetic medium for the spin transport might not be comparable [23,24] and this necessitates alternate methods for effective spin injection. Here, the introduction of a thin layer of an insulating material (I) between the ferromagnet (F) and the non-magnetic medium (N) is found to increase the magnitude of the measured spin-signal due to the following reasons [25].

(1) The tunnel barrier (I) provides high spin dependent resistance at the F/N interface and enhances the spin polarization of the injected tunneling current into the non-magnetic medium by overcoming the conductivity mismatch between the ferromagnet and the non-magnetic medium.

(2) The high spin dependent resistance of the tunnel barrier also prevents the back flow of the injected spins into the ferromagnet and allows the spins to diffuse in the non-magnetic medium. Thus the spin detection through the tunnel barrier is ideal since the measured voltage will predominantly be due to the spin accumulation in the non-magnetic medium and not due to the spin relaxation in the ferromagnetic detector. Thus the spin transport measurement using the F/I/N/I/F configuration for injection and detection probes the spin relaxation happening due to the spin scattering process in the non-magnetic medium.

2.3.4.1 F/I/N/I/F spin-valve

Consider an infinite non-magnetic metal strip (N) to which a ferromagnet (F) is contacted via a tunnel barrier (I). Let this position be denoted by $x = 0$. The non-equilibrium density of up and down spins injected from the ferromagnet to the non-magnetic medium decays exponentially as it diffuses along the strip and at $x \to \pm\infty$ the total spin imbalance in the non-magnetic medium is fully neutralized due to the spin flip scattering in the medium. Let $\tau_{s,\uparrow,\downarrow}$ be the average time for an up spin to flip to a down spin and $\tau_{s,\downarrow,\uparrow}$ the average time for a down spin to flip to an up spin. If $n_\uparrow$ and $n_\downarrow$ represents the density of the up and down spins in the non-magnetic medium, then the requirement that the total number of particles (n) in the system is conserved leads to the condition

$$\frac{1}{e}\nabla j_\uparrow = -\frac{n_\uparrow}{\tau_{s,\uparrow,\downarrow}} + \frac{n_\downarrow}{\tau_{s,\downarrow,\uparrow}} \tag{2.3.9}$$

and

$$\frac{1}{e}\nabla j_\downarrow = \frac{n_\uparrow}{\tau_{s,\uparrow,\downarrow}} - \frac{n_\downarrow}{\tau_{s,\downarrow,\uparrow}} \tag{2.3.10}$$

At steady state when there is no net spin scattering, the relation (2.3.9) and (2.3.10) gives

$$\frac{N_\uparrow}{\tau_{s,\uparrow,\downarrow}} = \frac{N_\downarrow}{\tau_{s,\downarrow,\uparrow}} \tag{2.3.11}$$

From equations (2.3.1), (2.3.9), and (2.3.10), the spin diffusion equations can be derived

$$D\frac{\partial^2(\mu_\uparrow - \mu_\downarrow)}{\partial x^2} = \frac{(\mu_\uparrow - \mu_\downarrow)}{\tau_s} \tag{2.3.12}$$

where $\mu_{\uparrow,\downarrow}$ is the chemical potential for up and down spins, D=$D_{\uparrow}D_{\downarrow}(N_{\uparrow}+N_{\downarrow})/(N_{\uparrow}D_{\uparrow}+N_{\downarrow}D_{\downarrow})$ is the spin averaged diffusion coefficient and $1/\tau_s = 1/\tau_{s,\uparrow,\downarrow}+1/\tau_{s,\downarrow,\uparrow}$ is the spin relaxation time. The solution to the above spin diffusion equation is given by

$$\mu_{\uparrow}(x) = \mu_0 exp(-x/\lambda_s) \tag{2.3.13}$$

$$\mu_{\downarrow}(x) = -\mu_0 exp(-x/\lambda_s) \tag{2.3.14}$$

The boundary conditions, for the F/I/N/I/F system with zero spin flip scattering at the interface are

(1) continuity of $\mu_{\uparrow}$, $\mu_{\downarrow}$ at the interface and

(2) conservation of the spin-up ($j_{\uparrow}$) and spin-down ($j_{\downarrow}$) currents at the interface.

Based on the above boundary condition, the equations (2.3.13) and (2.3.14) can be solved for μ_0 employing a simple resistor model for the F/I/N/I/F system [1] as shown in the figure 2.4. From the F/I/N circuit, the spin accumulation at the injector position x=0

$$I_{\uparrow}R^I_{\uparrow} - I_{\downarrow}R^I_{\downarrow} = \frac{2\mu_0}{e} \tag{2.3.15}$$

where we assume that the magnitude of the chemical potential for the up and down spin in the ferromagnet F to be μ_0 but of opposite sign. Here,

$$I_{\uparrow} = \frac{-I}{2} - \frac{\mu_0}{eR_N} \tag{2.3.16}$$

and

$$I_{\downarrow} = \frac{-I}{2} + \frac{\mu_0}{eR_N} \tag{2.3.17}$$

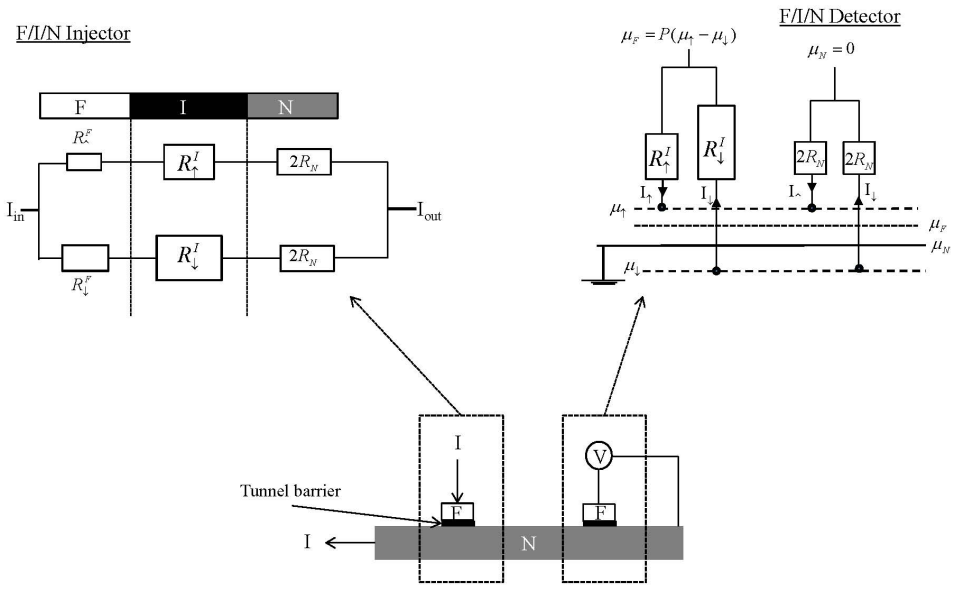

Figure 2.4: Schematics of F/I/N/I/F non-local spin-valve structure. The top left inset shows the resistor model for F/I/N spin injector and the top right inset shows the resistor model for the voltage probe.

From equation (2.3.13) and (2.3.14), we get the spin accumulation at x =0 as

$$\mu_\uparrow - \mu_\downarrow = 2\mu_0 \tag{2.3.18}$$

Equating the relations (2.3.15) with (2.3.18), we can estimate the value for the spin accumulation at $x = 0$ which turns out to be

$$\mu_\uparrow - \mu_\downarrow = 2\mu_0 = \frac{IeR_NP}{1 + 2R_N/(R_\uparrow^I + R_\downarrow^I)} \tag{2.3.19}$$

where $P = \frac{R_\downarrow^I - R_\uparrow^I}{R_\uparrow^I + R_\downarrow^I}$ is the polarization of the current in the non-magnetic material. In general, if the tunnel resistance $(R_\uparrow^I + R_\downarrow^I)$ is much larger than the resistance of the non-magnetic medium, then at x=0

$$\mu_0 = \frac{IeR_NP}{2} = \frac{Ie\lambda_sP}{2A\sigma_N} \tag{2.3.20}$$

where λ_s is the spin relaxation length in N, A is the active area of N and σ_N is the conductivity of N. Now the injected spins in the non-magnetic medium (N) decays as it diffuses through N and is detected by a second ferromagnet. The signal measured across the detector electrode can be calculated as follows. Since the detector electrode probes the voltage (potential), there is no net current flow into the ferromagnetic probe and the potential at the ferromagnet is a weighted average of the $\mu_\uparrow$ and $\mu_\downarrow$ in N.

i.e.

$$\mu_F = \frac{P(\mu_\uparrow - \mu_\downarrow)}{2} \tag{2.3.21}$$

and the measured non-local signal at a distance $x = L$ is given by

$$\begin{aligned} R_N(L) = \frac{V}{I} &= \frac{(\mu_F - \mu_N)}{eI} \\ &= \pm\frac{P(\mu_\uparrow - \mu_\downarrow) - 0}{eI} \\ &= \pm\frac{P^2\lambda_s}{2A\sigma_N} exp(\frac{-L}{\lambda_s}) \end{aligned} \tag{2.3.22}$$

i.e. the measured non-local signal decays exponentially as a function of the distance L between the injector and detector electrodes [26, 27]. Thus, the relevant spin parameters like the spin relaxation length and the spin polarization can be determined experimentally by studying the length dependence of the non-local signal.

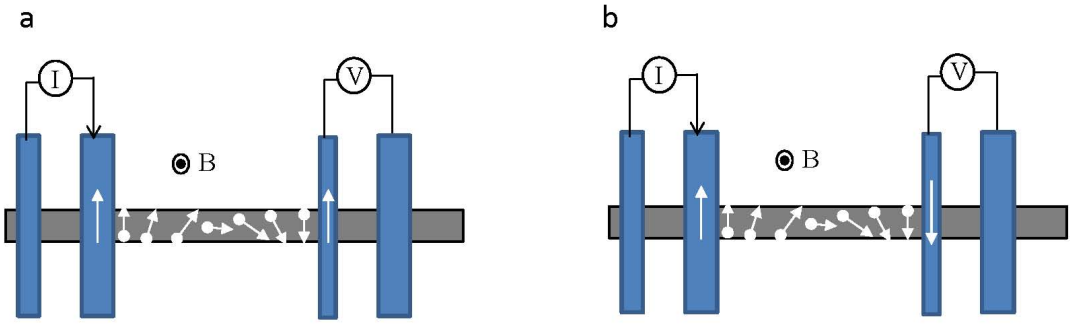

Figure 2.5: Schematics of the spin precession measurement in non-local geometry when both the injector and detector ferromagnets have (a) parallel magnetization and (b) anti-parallel magnetization with the external magnetic field applied perpendicular to the initial direction of the spin.

2.4 Electron spin precession in an external magnetic field

An alternate and unambiguous method to confirm the spin signal in a non-magnetic medium N is to study the precession of the diffusing spins in an external magnetic field applied perpendicular ($B_\perp$) to the initial spin direction [28]. The $B_\perp$ field will exert a torque on the spins because of which the spin angular momentum vector S precess (Larmor precession) about the applied field. The torque T is given by

$$T = -\mu_B B_\perp sin\theta \tag{2.4.1}$$

and the precession frequency, Larmor frequency is given by

$$\omega_L = \frac{-g\mu_B B_\perp}{\hbar} \tag{2.4.2}$$

where g is the g-factor for electrons, μ_B is the Bohr magneton and $g\mu_B/2$ is the spin magnetic moment associated with the spin angular momentum S (S= 1/2) and $\hbar$ is

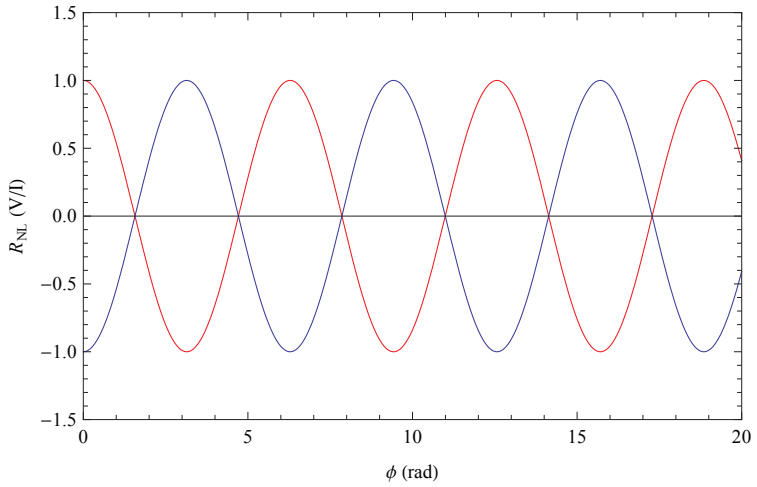

Figure 2.6: Modulation of the spin signal in an external magnetic field due to spin precession in the ballistic transport regime. The red and blue curve represents the spin signal modulation for the relative parallel and anti-parallel magnetization between the injector and detector electrodes.

the reduced Planck's constant.

2.4.1 Spin precession in ballistic transport regime

When a perpendicular field is applied to the initial direction of the spin the measured spin signal will be modulated due to the precession of the spin. The external magnetic field, $B_{\perp}$, changes the initial direction of the spin by an angle $\phi = \omega_L t = \frac{-g\mu_B B_{\perp}}{\hbar} t$ (here t is the time of flight of electrons from injector to detector) and the detector electrode detects by projecting this modified spin direction on its magnetization direction, i.e. the detector electrode sees the parallel component ($\cos\phi$) of the spins on its magnetization direction. In the ballistic transport regime, assuming no back-scattering of electrons at the interface, the measured output signal will be a perfect modulation of the cosine function ($\cos\phi$) as shown in figure 2.6

2.4.2 Spin precession in diffusive transport regime

In the diffusive transport scenario, the time of flight t for the spins to reach the detector from the injector is not unique, i.e. the diffusing electrons can take different paths to reach the detector electrode. Such a spread in the diffusion time implies a spread in the precession angle $\phi = \omega_L t$. The probability that the electrons injected at $x = 0$ is present at $x =$ L without spinflip at time t is given by the distribution $(\rho(x,t))$ [1, 4]

$$\rho(L,t) = \sqrt{1/4\pi Dt}\ e^{(-L^2/4Dt)} \tag{2.4.3}$$

where $\rho(L,t)$ is proportional to the number of electrons per unit volume that will be present at the detector electrode after a diffusion time t.

Due to the distribution of the electron transit time in diffusive transport the spin precession angle for the electrons is also different. When this difference becomes comparable to the Larmor period the average spin reaching the detector electrode will be zero and the spin signal vanishes. In addition to the decay of the spin signal due to the distribution of the spin diffusion time, the spin flip process should also be considered. The probability that the electron spin has not flipped within a time period t is given by exp(-t/τ_s) and hence the total probability for finding the spin at a distance $x = L$ after a time t is

$$\rho(L,t)e^{(-t/\tau_s)} = \sqrt{1/4\pi Dt}\ e^{(-L^2/4Dt)}\ e^{(-t/\tau_s)} \tag{2.4.4}$$

Now to calculate the measured voltage across the detector electrodes we first determine the number of spin-polarized electrons ($n_\uparrow$-$n_\downarrow$) arriving at the detector. This can be estimated by the summation of all injected spins arriving at the detector.

$$n_\uparrow - n_\downarrow = \frac{IP}{eA} \int_0^\infty \rho(t) cos(\omega_L t) e^{(-t/\tau_s)} dt \tag{2.4.5}$$

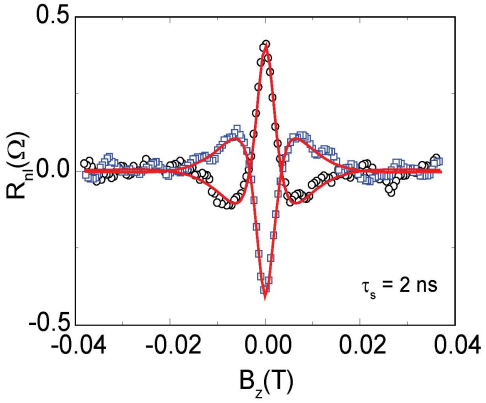

Figure 2.7: Modulation of the spin signal in an external magnetic field due to spin precession in the diffusive transport regime for graphene spin-valves. The red curve represents the fit to the data points.

where IP/e is the injection rate and $\cos(\omega_L t)$ is the precession around the perpendicular axis. Since $\mu_\uparrow$-$\mu_\downarrow = \frac{2}{N(E_F)}(n_\uparrow$-$n_\downarrow)$ and V, the measured voltage is P($\mu_\uparrow$-$\mu_\downarrow$)/e, the output voltage for the parallel and anti-parallel configuration of the injector and detector electrodes becomes

$$V(B_\perp) = \pm\frac{IP^2}{e^2 N(E_F) A}\int_0^\infty \rho(t) cos(\omega_L t) e^{(-t/\tau_s)} dt \tag{2.4.6}$$

From equation (2.4.6) it is clear that the spin precession signal has both the oscillatory and decay component which dampens the oscillation. Hence, to see the sign reversal of the spin signal in a precession measurement, the spread in the precession angle should be much smaller than π, while the average precession angle is much larger than π. A typical spin precession signal for a graphene based non-local spin-valve device is shown in figure 2.7

2.5 Spin relaxation mechanisms

The diffusion of spins in a non-magnetic medium is always accompanied by spin flip scattering processes. The process of spin scattering results in the damping of the spin signal as it travels along the non-magnetic medium and hence it is important to understand the fundamental reasons behind such scattering events. There are four main scattering mechanisms identified that could cause spin flip/dephasing in a non-magnetic medium. They are Elliott-Yafet, D'yakonov-Perel, Bir-Aronov-Pikus and hyperfine interactions [3, 4].

2.5.1 Elliott-Yafet spin scattering

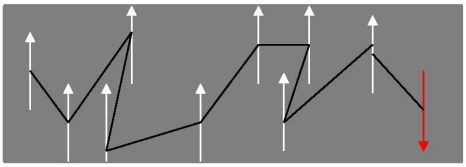

Figure 2.8: Schematics for Elliott-Yafet spin scattering. Here, the momentum scattering by impurities or phonons has a finite probability to flip the electron spin.

In the Elliott-Yafet (EY) mechanism [29, 30] the spin relaxation occurs as a consequence of the momentum scattering of the conduction electrons with phonons or impurities. Due to spin-orbit coupling the eigenstates of the electron wavefunctions are a mixture of both spin up and spin down states.

The probability for the electron's spin to flip increases with each momentum scattering and thus the faster the momentum scattering the faster the relaxation of spins. i.e. in the EY mechanism the spin relaxation rate is proportional to the momentum relaxation rate

$$\frac{1}{\tau_s} \propto \frac{1}{\tau_p} \tag{2.5.1}$$

The EY mechanism is found to be more dominant in semiconductors with a centre of symmetry such as silicon.

2.5.2 D'yakonov-Perel spin scattering

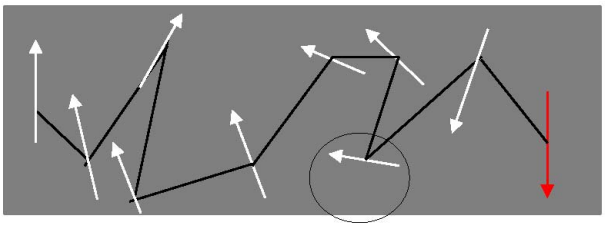

Figure 2.9: Schematics for D'yakonov-Perel spin scattering. Here, the electron spin precess about the momentum dependent magnetic field.

The D'yakonov-Perel scattering [31] is found to be dominant in semiconductors without a centre of symmetry, for e.g. semiconductors with zinc blende structure such as GaAs, where the inversion symmetry is broken by the presence of two distinct atoms in the Bravis lattice. The lack of inversion symmetry makes the momentum states of spin-up and spin-down electrons to be non-degenerate. Such spin splitting due to inversion asymmetry manifests itself as a momentum dependent magnetic field ($B(k)$) about which the electron spins precess with a Larmor frequency, $\Omega(k) = (e/m)B(k)$. This intrinsic magnetic field is as a result of the spin-orbit coupling in the material. When a moving electron gets scattered by impurities or phonons, the momentum dependent magnetic field experienced by the electron also changes both in magnitude and direction, i.e. the electron spins precession axis and direction changes and the spin relaxation happens between the momentum scattering events. The more the momentum scattering events, the less the spin relaxation

$$\tau_s \propto \frac{1}{\tau_p} \tag{2.5.2}$$

2.5.3 Bir-Aronov-Pikus spin scattering

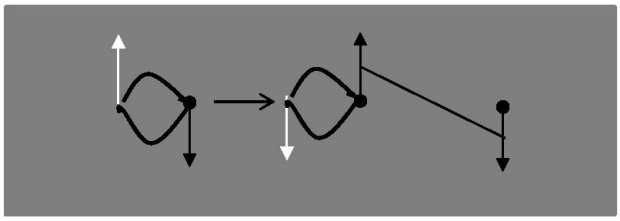

Figure 2.10: Schematics for Bir-Aronov-Pikus spin scattering.Here, the electron exchanges spin with holes of opposite spin, which then undergoes spin relaxation via Elliott-Yafet scattering.

In heavy p-doped semiconductors the spin relaxation can occur by scattering followed by a spin exchange between electrons and holes [32]. The exchange interaction given by the Hamiltonian

$$H = A\mathbf{S}.\mathbf{J}\delta(r) \tag{2.5.3}$$

where A is the exchange integral between conduction and valence bands, J is the angular momentum operator, S is the spin operator and r is the relative position of electrons and holes. An electron with up spin will exchange its spin with down spin hole. Since the holes in semiconductors relax their spin fast due to the high spin-orbit coupling and thus acts as a reservoir for the electrons to lose their spins. In general, the Bir-Aronov-Pikus (BAP) mechanism coexists with EY and DP mechanism. However, the three mechanisms can be identified based on their density and temperature dependences. BAP mechanism dominates in heavy p-doped semiconductors at low temperatures while at high temperatures the DP mechanism dominates due to its increased importance at large electron densities.

2.5.4 Spin scattering due to hyperfine interaction

The hyperfine interaction is the magnetic interaction between electron spins and nuclei spin. In general this interaction is dominant for spin decoherance of localized electrons in quantum dots [3, 4]. This interaction is weak in metals and semiconductors.

2.6 Spin-orbit coupling

Spin-orbit coupling (SOC) refers to the interaction between an electron's linear momentum with its spin angular momentum [33]. Such a coupling between the electron's momentum and its spin state is quite important since it will allow the manipulation of the electron spin without the need for an external magnetic field and the strength of the SOC will also determine the spin relaxation in the material. These two factors are essential for the manifestation of spin Hall effect, which occurs due to the spin dependent scattering induced by the enhanced SOC in the material. Since, the focus of the second half of this thesis will be on the enhancement of the SOC in graphene by functionalization and the manifestation of the spin Hall effect in such functionalized graphene, a basic idea on the evolution of the SOC in individual atoms (taking hydrogen as an example) as well as in solids will be discussed.

2.6.1 Spin-orbit coupling: atomic picture

In an atom the electrons orbit around the nucleus and the system can be represented by a Hamiltonian (H) consisting of a kinetic energy (K.E) part due to the electron's momentum and a potential energy(P.E) part due to the Coulomb interaction between the electrons and the nucleus [33, 34]. i.e.

$$H = K.E + P.E = \frac{\mathbf{p}^2}{2m^*} - e\phi(r) = \frac{-\hbar^2}{2m^*}\nabla^2 - \frac{Ze^2}{r} \tag{2.6.1}$$

where $\mathbf{p}$ is the momentum operator given by $\frac{-\hbar^2}{2m^*}\nabla^2$ and $\phi(r)$ is the Coulomb potential experienced due to the positive nucleus and is given by $\frac{Ze}{r}$.Here, m* is the rest mass of electron, e is the charge of electron and Z is the atomic number. For simplicity, let us consider the case of hydrogen atom with Z = 1. In the rest frame of electron, the electron orbiting the nucleus transforms to a system where the electron sees the nucleus orbiting around it with a velocity $\mathbf{v_p}$ =$-\mathbf{p}/2\mathrm{m}^*$. This motion of the nucleus produces a magnetic field

$$B_{SO} = \frac{1}{c}\mathbf{v_p} \times \mathbf{E}(\mathbf{r}) \tag{2.6.2}$$

Since $\mathbf{E}(\mathbf{r})$= (-1/e)∇V(r) and ∇V(r) = $\mathrm{e}^2\mathbf{r}/\mathrm{r}^3$, the equation (2.6.2) can be rewritten as

$$B_{SO} = \frac{-1}{2m^*ec}\mathbf{p} \times \nabla\mathbf{V}(\mathbf{r}) = \frac{-e}{2m^*c}\frac{\mathbf{p} \times \mathbf{r}}{r^3} \tag{2.6.3}$$

This magnetic field interacts with the spin of the electron via the Zeeman interaction

$$H_{SO} = -\mu_\mathbf{s}.\mathbf{B_{SO}} = \frac{e}{2m^*c}\mu_\mathbf{s}.\frac{\mathbf{p} \times \mathbf{r}}{r^3} \tag{2.6.4}$$

Here, $\mu_\mathbf{s}$ is the magnetic moment of the electron spin in vacuum and is given by

$$\mu_\mathbf{s} = -\frac{g\mu_B\mathbf{S}}{\hbar} \tag{2.6.5}$$

where g is the electron g-factor = 2, μ_B is the Bohr magneton = $\frac{e\hbar}{2m^*c}$, $\mathbf{S}$ is the spin angular momentum and $\mathbf{r} \times \mathbf{p} = \mathbf{L}$ is the orbital angular momentum.

Substituting the values for $\mu_{\mathbf{s}}$ and $\mathbf{p} \times \mathbf{r}$, we get

$$H_{SO} = \frac{g\mu_B^2}{\hbar^2}\frac{\mathbf{S}.\mathbf{L}}{r^3} \tag{2.6.6}$$

The equation (2.6.6) thus represents the coupling of electron's spin and its orbital angular momentum about the nucleus in vacuum and is known as the spin-orbit coupling. The above equation can also be written in a more generalized form by using equations (2.6.2), (2.6.3) and (2.6.4) as

$$\begin{aligned} H_{SO} &= \frac{g\mu_B^2}{\hbar^2}\frac{\mathbf{S}.\mathbf{L}}{r^3} \\ &= -\frac{g}{\hbar^2}\frac{e^2\hbar^2}{4m^{*2}c^2}\frac{\mathbf{S}.\mathbf{p}\times\mathbf{r}}{r^3} \\ &= -\frac{ge^2}{4m^{*2}c^2}\frac{\mathbf{S}.\mathbf{p}\times\nabla\mathbf{V}(\mathbf{r})}{e^2} \\ &= -\frac{g\hbar}{4m^{*2}c^2}\mathbf{S}.\mathbf{k}\times\nabla\mathbf{V}(\mathbf{r}) \\ &= -\frac{g\hbar^2}{8m^{*2}c^2}\sigma.\mathbf{k}\times\nabla\mathbf{V}(\mathbf{r}) \\ &= \lambda_{SO}\ \sigma.(\mathbf{k}\times\nabla\mathbf{V}(\mathbf{r})) \end{aligned} \tag{2.6.7}$$

where λ_{SO} is the spin-orbit coupling strength in vacuum, λ_{SO} = -3.7×10^{-6} $\mathring{A}^2$,σ is the Pauli spin matrices, and $\mathbf{k} = \mathbf{p}/\hbar$ is the electron wave vector.

2.6.1.1 Dependence of SOC strength on the atomic number

In the previous section we calculated the spin-orbit coupling for atomic hydrogen. Now, it will be interesting to see how this SOC strength depends on the atomic number Z. It should be noted that since the Coulomb potential is proportional to Z, it is evident that the SO strength should be proportional to Z. Moreover, the average value for the factor ($1/r^3$) in equation (2.6.4) also depends on Z as

$$< \frac{1}{r^3} >= \int \Psi^* \frac{1}{r^3} \Psi r^2 dr d\Omega \propto Z^3 \tag{2.6.8}$$

for an atomic wavefunction Ψ . Hence, the total spin-orbit coupling strength will depend on the atomic number as Z^4 [35].

2.6.2 Spin-orbit coupling in solids

The spin-orbit coupling in a material without any magnetic impurities can be derived as follows [34]. If V_{SO} represents the spin-orbit potential and V_r represents the normal impurity potential, then the total potential $V_{tot} = V_{SO} + V_r$ creates an electric field $\mathbf{E}(\mathbf{r})$ given by $\mathbf{E}(\mathbf{r}) = -(1/e)\nabla V_{tot}(r)$. When a free conduction electron moving with a velocity $\mathbf{v} = (\hbar/i)\nabla/m^*$, encounters this field, it experiences an effective magnetic field given by $\mathbf{B_{eff}}(\mathbf{r}) = -(1/m^*c)\mathbf{p} \times \mathbf{E}(\mathbf{r})$, which in turn introduces a spin-orbit coupling given by

$$H_{SO}(r) \propto \sigma.\mathbf{B_{eff}}(\mathbf{r}) \tag{2.6.9}$$

Here, the effective magnetic field B_{eff} includes contributions from the materials' band structure and also from impurities present in the system. Thus, we can say that the B_{eff} could be determined by two different physical mechanisms. The intrinsic mechanism, which is due to the spin-related band structure of the material, and the extrinsic mechanism which is due to the impurities present in the system.

2.6.3 Spin dependent scattering due to spin-orbit coupling

2.6.3.1 Intrinsic spin-orbit coupling: Dresselhaus and Rashba spin-orbit interaction

The contribution of the intrinsic effect to spin-orbit coupling (SOC) was first proposed by Karplus and Luttinger in 1954 to explain the observed anomalous Hall effect (AHE) in ferromagnets [36]. This effect is related to the spin-dependent band structure of the materials and is prominent in systems without inversion symmetry. In general, there are two important types of inversion asymmetry (1) the Dresselhaus inversion asymmetry - due to the bulk inversion asymmetry, and (2) the Rashba inversion asymmetry - due to the structural inversion asymmetry.

The Hamiltonian for the linear Dresselhaus and Rashba coupling in a 2D system can be written as [37]

$$H_D = \frac{\hbar^2 k^2}{2m} + \beta(k_x\sigma_x - k_y\sigma_y) \tag{2.6.10}$$

and

$$H_R = \frac{\hbar^2 k^2}{2m} + \alpha(k_x\sigma_y - k_y\sigma_x) \tag{2.6.11}$$

It should be noted that for the Rashba coupling the effective magnetic field (B_{eff}) is perpendicular to $\mathbf{k}$ while for the Dresselhaus term it has a more complicated dependence. The intrinsic mechanism can be explained qualitatively as discussed below: Consider a 2D system where the electrons' spins are confined to the plane. Now when an external electric field is applied along the x direction the Fermi surface gets displaced in the x direction in k-space. This means that the $\mathbf{k}$ dependent intrinsic magnetic field shifts to $\mathbf{B_{eff}}(\mathbf{k}) \rightarrow \mathbf{B_{eff}}(\mathbf{k} + \mathbf{\Delta k})$ which realigns the spins out of the magnetic field direction. The field $\mathbf{B_{eff}}(\mathbf{k} + \mathbf{\Delta k})$ exerts a torque on the spins and

aligns them back to the field direction. If we consider two electrons in the opposite side of the Fermi surface ($\pm\ k_y$), the field $\mathbf{B_{eff}}(\mathbf{k}+\mathbf{\Delta k})$ points in the opposite direction enabling the creation of a z-polarized spin current in the y-direction.

2.6.3.2 Extrinsic spin-orbit coupling

In the extrinsic spin-orbit interaction, the spin-dependent scattering of electrons occurs due to the presence of impurities or defects in the material. The extrinsic spin scattering mechanism has been classified into two distinct types: (1) skew scattering and (2) side-jump scattering mechanisms.

2.6.3.3 Skew scattering

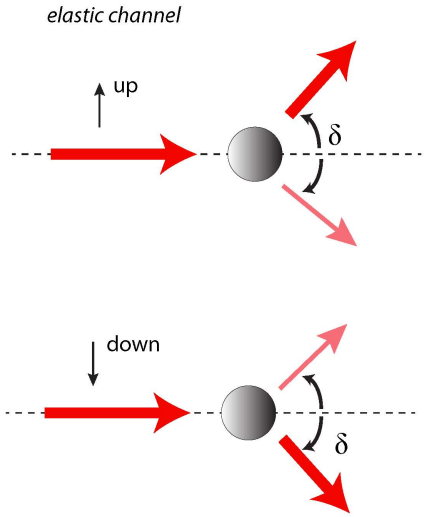

Figure 2.11: The trajectory for the spin-up and spin-down electrons after skew scattering. The angle δ represents the angle at which the electrons get deflected.

The first mathematical investigation on the scattering of an incoming wave of electrons by nuclei was carried out by Nevil Mott in 1929 by a double scattering method

[38]. Based on the spin-orbit interaction term discovered by Dirac, Mott showed that for an incoming beam of electrons with spin polarization P, the detectors placed at opposite sides of the beam measured different scattering densities. This asymmetrical scattering of electrons thus provided an unambiguous evidence for the existence of the free electron spin and is known as the skew scattering [38–40]. In a simple way the skew scattering can be understood from the electron-impurity collisions. An electron passing through an impurity potential V(r) with a velocity **v** experiences an electric field $\mathbf{E}(\mathbf{r}) = \nabla V(r)$. In the rest frame of the electron, the moving charge induces an effective magnetic field $\mathbf{B_{eff}} = -\frac{\mathbf{v}\times\mathbf{E}}{c^2}$. This spin-orbit-induced magnetic field exerts a spin-dependent force proportional to the gradient of the Zeeman energy,

$$F = 2\mu_B \nabla(\mathbf{S}.\mathbf{B}) \tag{2.6.12}$$

such that the force at one end of the dipole will be slightly greater than the opposing force at the other end of the dipole. This leads to a spin current along the orthogonal direction. Here, the rate of spin separation is proportional to the rate of collision between the electrons and the impurities. That is, the skew scattering resistivity is linearly proportional to the Drude resistivity, $\rho_{SS} \propto \rho_{xx}$. Figure 2.11 shows the schematics for the skew scattering which is characterized by an angle δ; the angle at which the electrons get deflected from their initial path due to spin dependent scattering. However, the skew scattering will not lead to a charge separation in the orthogonal direction due to the equal population of spin-up and spin-down electrons in a non-magnetic material. This spin accumulation at the sample edges gives rise to the spin Hall effect (SHE).

2.6.3.4 Side-jump

A different scattering of spins due to spin-orbit coupling, called the side-jump spin scattering, was proposed by Berger in 1970 [41]. The origin of the side-jump scattering

can be traced back to the anomalous velocity operator in systems with spin-orbit interaction, and is defined as the sideways displacement of the center of mass of an electron wave packet due to collisions with the impurity potential [42]. A schematic showing the side-jump scattering is shown in figure 2.12. In a system with spin-orbit potential, the total impurity potential is given by $V_{tot} = V_{SO} + V_r$. The one-electron Hamiltonian for this system is then [34]

$$H = \sum_{k,\sigma} \xi_k a^{\dagger}_{k\sigma} a_{k\sigma} + \sum_{k,k'} \sum_{\sigma,\sigma'} V^{\sigma,\sigma'}_{tot,k,k'} a^{\dagger}_{k'\sigma'} a_{k\sigma} \tag{2.6.13}$$

In equation (2.5.13), the first term represents the kinetic energy of the electrons with

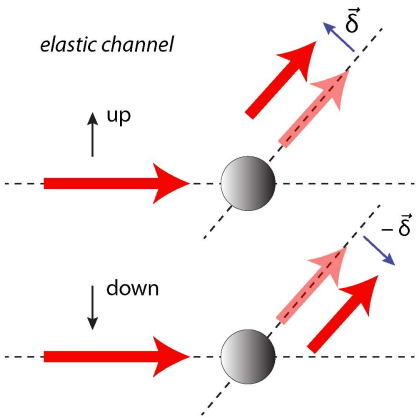

Figure 2.12: The trajectory for the spin-up and spin-down electrons after side-jump scattering. The vector $\vec{\delta}$ represents the opposite sideways displacement of the electrons with up and down spins.

energy ξ_k and the second term represents the total impurity potential for the localized impurities and can be rewritten in the form

$$V^{\sigma,\sigma'}_{totk,k'} = V_{imp}[\delta_{\sigma'\sigma} + i\lambda^{eff}_{SO}\sigma_{\sigma'\sigma}.(\mathbf{k} \times \mathbf{k}')] \sum_i e^{i(\mathbf{k}-\mathbf{k}').\mathbf{r_i}} \tag{2.6.14}$$

The velocity of the electron in this impurity potential can be calculated from the velocity operator $\mathbf{v} = d\mathbf{r}/dt = (1/i\hbar)[\mathbf{r}, \mathbf{H}(\mathbf{k})]$. In the momentum space the operator for

$\mathbf{r}= \mathrm{i}\nabla_k$. Now the velocity can be estimated by taking the matrix elements between the scattering states $\left|\mathbf{k}^{\dagger}\sigma\right\rangle$

$$\mathbf{v}_{\mathbf{k}}^{\sigma} = \left\langle \mathbf{k}^{\dagger}\sigma \right| \hat{\mathbf{v}} \left| \mathbf{k}^{\dagger}\sigma \right\rangle = \frac{\hbar \mathbf{k}}{m^*} + \omega_{\mathbf{k}}^{\sigma} \tag{2.6.15}$$

where the second term $\omega_{\mathbf{k}}^{\sigma}$ represents the anomalous velocity due to the spin-orbit term and is

$$\omega_{\mathbf{k}}^{\sigma} = \frac{\lambda_{SO}^{eff}}{\hbar} \sum_i \left\langle \mathbf{k}^{\dagger}\sigma \right| \sigma \times \nabla V(\mathbf{r} - \mathbf{r_i}) \left| \mathbf{k}^{\dagger}\sigma \right\rangle \tag{2.6.16}$$

The side jump displacement can be determined by integrating the equation (2.6.14). Here, it is important to note that the electron displacement is along the direction given by $\sigma \times \nabla V(\mathbf{r} - \mathbf{r_i})$ and is evident that the direction of the scattering is spin dependent. Moreover, the side jump resistivity scales quadratically with the Drude resistivity $\rho_{SJ} \propto \rho_{xx}^2$.

The difference in the resistivity dependence of the skew scattering and side jump mechanism can be used to differentiate the dominant mechanism in a material. For instance the skew scattering mechanism dominates when ρ_{xx} is small and also at low temperatures and at low impurity concentration, while the side jump mechanism dominates when ρ_{xx} is large and at high temperatures and at higher impurity concentrations. However, in an experiment both contributions may be present and the measured dependence of the transverse resistivity would be a linear combination of both the contributions i.e.

$$\rho_{xy} = A\rho_{xx} + B\rho_{xx}^2 \tag{2.6.17}$$

where A and B are constants.

2.7 Spin Hall Effect

In the above section, we found that the spin-orbit interaction in solids can introduce spin-dependent scattering of electrons. There are two important physical phenomena arising due to the spin-orbit interaction in solids; (1) the anomalous Hall effect (AHE) in ferromagnetic materials [43, 44] and (2) the spin Hall effect (SHE) in paramagnetic materials [45, 46]. Both these effects could originate either from the extrinsic skew scattering and side-jump mechanisms or the intrinsic mechanism due to the band-structure contribution. Since in this thesis the aim is to study the spin Hall effect in functionalized graphene, the focus of this section will be the SHE in paramagnetic materials.

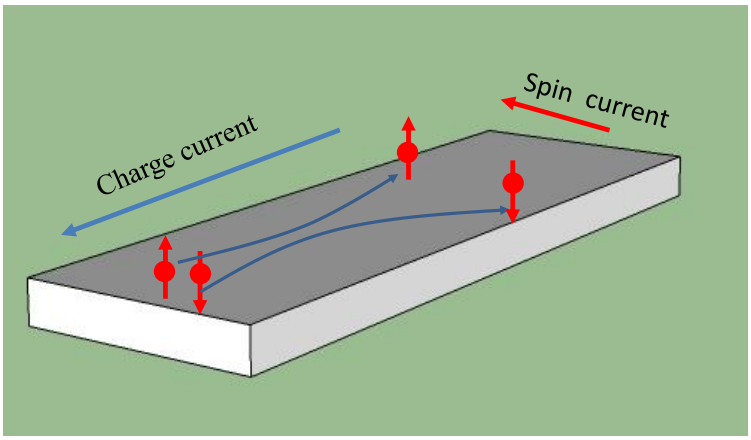

Figure 2.13: The trajectory for the spin-up and spin-down electrons due to spin Hall effect. The longitudinal charge current induces transverse spin accumulation

In paramagnetic materials when an unpolarized charge current is introduced by the application of an electric field, the spin-orbit interaction induces a spin Hall current and causes spin accumulation in the paramagnetic material in a direction perpendicular to the charge current (see figure 2.13).

2.7.1 Generation and detection of spin currents via SHE

Theoretically the possibility of orienting the spins with charge current (SHE) was first proposed by M. I. D'yakonov and V. I. Perel 1971 [45] and later independently by Hirsch in 1999 [46]. The first experimental detection of SHE was reported in 2004 in n-doped GaAs and InGaAs thin films by Kato *et al.* in both strained and unstrained thin films [47]. Here, the detection of the spin accumulation at the sample edges was performed by optical Kerr rotation spectroscopy and the experiments clearly demonstrated that the spin Hall effect observed in the strained samples depended weakly on the crystal direction and suggested the importance of extrinsic mechanism for the observed SHE. Soon after the first experimental demonstration, SHE was also demonstrated in p-doped GaAs using an electroluminescence method, where the orientation of the circularly polarized light reversed at the opposite edges of the sample indicating the presence of opposite spins at the sample edges [48]. The observed phenomenon was claimed to be intrinsic since the effect only depends weakly on the disorder in the system. Recently, SHE in n-doped GaAs [49], n-type ZnSe [50] semiconductors has been realized.

2.7.2 Electrical detection of spin currents

For the detection of SHE in a metallic system, the optical methods employed for semiconductors are not ideal. This is because in metallic systems the spin relaxation length is much smaller when compared to semiconductors. This means that the spin accumulation lies within the spin relaxation length scale and hence the large optical beams with spot sizes in the order of micrometers are unable to resolve the spin separation. The solution is to employ the inverse spin Hall effect, where the spin current induces a orthogonal charge current which can be measured as a Hall voltage.

The various methods employed to introduce spin currents in metals are

(1)*Ferromagnetic resonance induced spin − pumping* : In ferromagnetic resonance-based spin-pumping experiments the interfacial spins are pumped into the non-magnetic medium due to the precession of the ferromagnet's magnetization by the application of a microwave stimuli frequency matching the ferromagnetic resonance of the system [51, 52]. In ferromagnetic resonance experiments, the transfer of the spin angular momentum from the ferromagnet to the non-magnetic metal, a spin current is generated in the metal. The large spin-orbit coupling in the metal allows the conversion of the injected spin current into an electrical voltage by inverse spin Hall effect. This method has successfully been used to induce spin transport in metals like Au, Mo, Nb, Pd, Pt, PtCu, PtAu [51, 53–60] and recently in semiconductors like GaAs [61] and p-type Si [62].

(2)*Spin injection via ferromagnet* : Similar to the spin-valve devices, the injection of spin-polarized current to the non-magnetic metal is achieved by using a ferromagnetic electrode connected to the metal non-locally (see figure 2.14) . The spin polar-

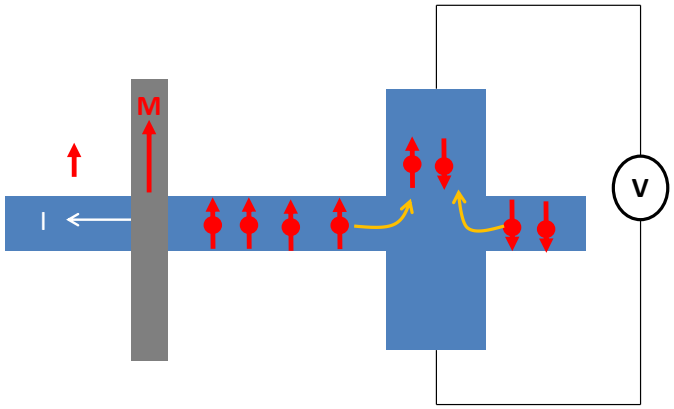

Figure 2.14: Schematics showing the measurement configuration for the detection of the spin accumulation by non-local inverse spin Hall effect. Here the spin is injected into the normal metal using a ferromagnet with magnetization M.

ized current from the ferromagnet diffuses into the non-magnetic metal and results in the generation of the electrical voltage due to the inverse spin Hall effect. This experiment was first demonstrated in Aluminum by Valenzuela and Tinkham [16,63,65–69].

(3)$Non-local\ H-bar\ geometry$: In the non-local H-bar geometry, the spin current is generated by the spin Hall effect and the detection of the diffusing spins in the material is done by invoking the inverse spin Hall effect (see figure 2.15) [70–72]. These

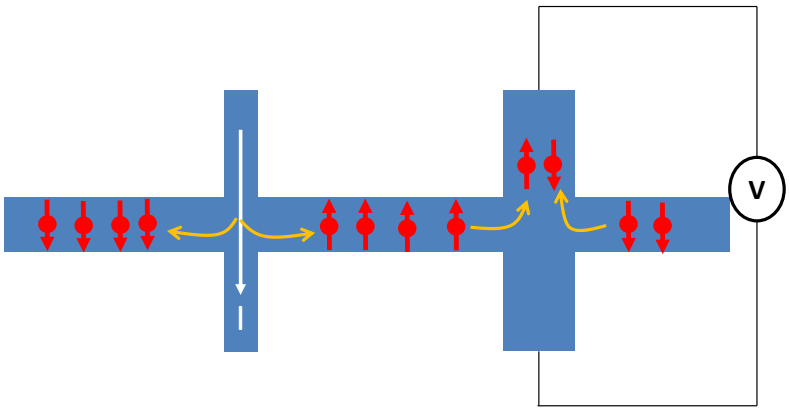

Figure 2.15: Schematics showing the measurement configuration for the injection and detection of the spin accumulation by non-local H-bar geometry. Here the spin separation is generated in the normal metal by spin Hall effect while the detection is realized by the inverse spin Hall effect.

experiments have successfully been performed by the group of Molenkamp in HgTe quantum wells where the helical nature of the spin polarized counter-propagating edge channels was demonstrated for the first time experimentally [73, 74].

2.7.3 Non-local spin detection in the diffusive regime using H-bar geometry

Consider an infinite narrow strip *i.e.* -∞< x <+∞ and -w/2< y <+w/2, where w is the width of the sample. In such a system, the spin accumulation generated by the spin Hall effect evolves according to the diffusion equation [71]

$$D_s \partial^2 s(x,y) - \Xi(x,y) - \frac{s(x,y)}{\tau_s} = 0 \tag{2.7.1}$$

where s is the z-component of the spin density, D_s is the spin diffusion coefficient, τ_s is the spin relaxation length, and Ξ represents the spin current due to the spin Hall effect and is given by

$$\Xi(x,y) = \sigma_s \delta\left(y - \frac{1}{2}w\right) E_{x,+}(x) - \sigma_s \delta\left(y + \frac{1}{2}w\right) E_{x,-}(x), \tag{2.7.2}$$

where σ_s is the spin Hall conductivity and $E_{x,\pm}$ *(x)* is the electric filed at the boundaries of the sample. The above equations can be solved by the inverse Fourier transform method to get the net spin current in the system

$$J_s(x) = \frac{I\sigma_s w}{2\sigma\lambda_s} e^{-|x|/\lambda_s}. \tag{2.7.3}$$

The spin current J_s*(x)* induces a non-local voltage across the detector electrodes by the inverse spin Hall effect and is given by

$$\delta V(x) = \frac{\gamma J_s(x)}{\sigma} = \frac{I\gamma\sigma_s w}{2\lambda_s \sigma^2} e^{-|x|/\lambda_s} \tag{2.7.4}$$

Here γ is the charge current generated due to the spin current (spin Hall coefficient) and is related to the spin conductivity σ_s and charge conductivity σ by the relation

$$\gamma = \frac{\sigma_s}{\sigma} \tag{2.7.5}$$

Substituting the relation for γ into equation (2.7.4) allows us to write the non-local response as a transresistance

$$R_{NL} = \frac{\delta V(x)}{I} = \frac{1}{2}\gamma^2 \frac{w}{\sigma\lambda_s} e^{-|x|/\lambda_s} \tag{2.7.6}$$

From equation (2.7.6) it is clear that the dependence of the non-local signal on the device parameters like length and width can be used to extract the spin parameters: spin relaxation length λ_s and the spin Hall coefficient γ. Here the measured non-local signal decays exponentially with length for a constant width while it increases linearly with width for a constant length.

2.7.4 Magnetic field dependence of the non-local signal

In the presence of an in-plane magnetic field the spin diffusion equation (2.7.1) is modified to [71]

$$D_s\partial^2 s(x,y) - \Xi(x,y) - \frac{s(x,y)}{\tau_s} + [\omega_{\mathbf{B}} \times \mathbf{s}] = 0 \tag{2.7.7}$$

where ω_B is the Larmor precession frequency. The solution to the above relation gives the net spin current in the channel to be

$$J_s(x) = \frac{I\sigma_s w}{2\sigma} Re\left[\sqrt{1+i\omega_B\tau_s}/\lambda_s e^{-\sqrt{1+i\omega_B\tau_s}|x|/\lambda_s}\right] \tag{2.7.8}$$

and the non-local transresistance to be

$$R_{NL} = \frac{\delta V(x)}{I} = \frac{1}{2}\gamma^2 \frac{w}{\sigma} Re\left[\sqrt{1+i\omega_B\tau_s}/\lambda_s e^{-\sqrt{1+i\omega_B\tau_s}|x|/\lambda_s}\right]. \tag{2.7.9}$$

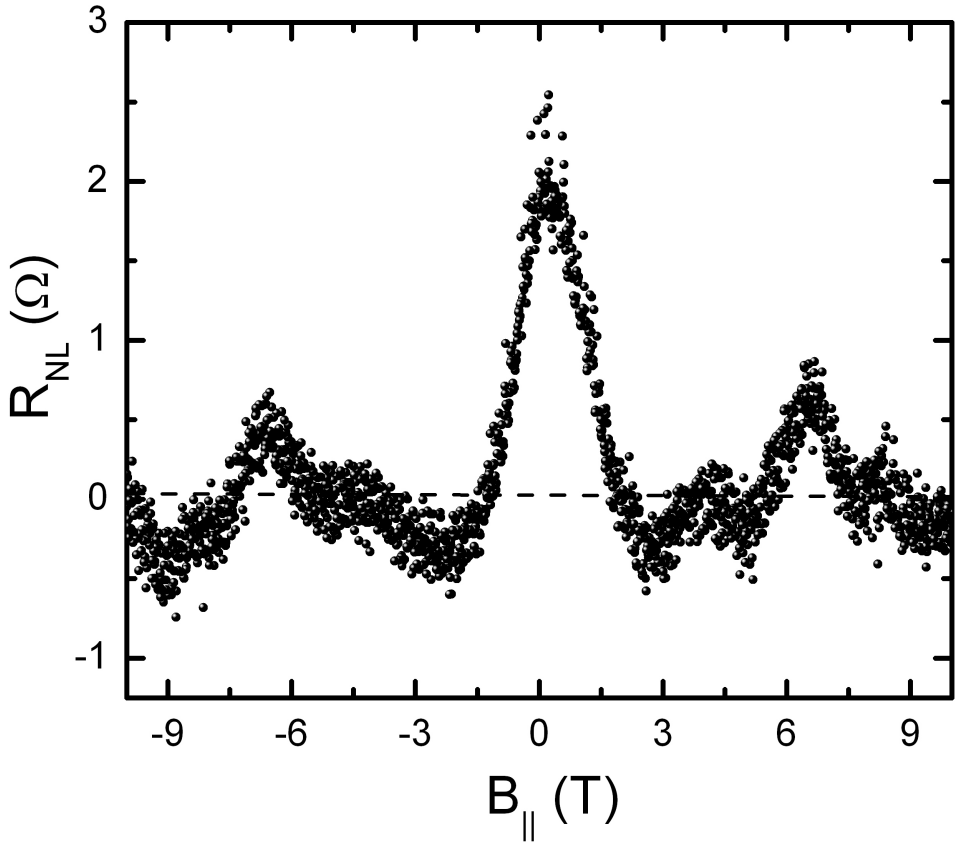

Figure 2.16: In-plane magnetic field dependence of the non-local spin Hall signal. The damped oscillatory behaviour of the non-local signal is a clear signature for the spin precession in the medium.

The equation (2.7.9) can be simplified for higher fields as

$$R_{NL} = \frac{1}{\sqrt{2}}\gamma^2\frac{w}{\sigma}\sqrt{\omega_B\tau_s/2}\; Sin\left(\frac{\sqrt{\omega_B\tau_s}|x|}{\sqrt{2}\lambda_s} + \frac{\pi}{4}\right)e^{-\sqrt{\omega_B\tau_s}|x|/\sqrt{2}\lambda_s}. \tag{2.7.10}$$

From the simplified equation for the non-local signal it is clear that the in-plane magnetic field modulates the non-local signal with multiple sign changes and damping. The oscillatory behaviour of the non-local spin Hall signal thus gives the unambiguous

confirmation for the measured transresistance to be of spin origin. Figure 2.16 shows a typical magnetic field dependence of the non-local signal for a weakly hydrogenated graphene sample.

2.8 Graphene

Graphene is the two dimensional array of carbon atoms arranged in a honeycomb lattice [5, 75–77]. Since graphene is only one atom thick, this material can be considered as the perfect 2D material ever discovered. Graphene forms the basis for all other carbon allotropes, and, hence, understanding the electronic properties of graphene is crucial. Some of the interesting properties of this wonder material are:

1. Its low energy excitations are massless Dirac fermions and hence at low energies this system mimics the physics of quantum electrodynamics for massless fermions.

2. The massless Dirac fermion nature of its charge carriers can be transmitted with probability one across a classically forbidden region - known as Klein-paradox.

3. Under certain conditions these Dirac fermions are immune to localization effects.

4. Being only one atom thick, graphene is highly structurally and electronically flexible allowing chemical and structural modifications, thus enabling the creation of graphene-based magnetic and superconducting systems.

5. Since carbon atoms have low atomic number, the spin-orbit coupling in graphene is very weak and thus would allow spin transport over large distances of the order of hundreds of micrometer even at room temperature.

In the following section, a brief review on the electronic and spintronic properties of graphene will be presented.

2.8.1 Electronic properties of graphene

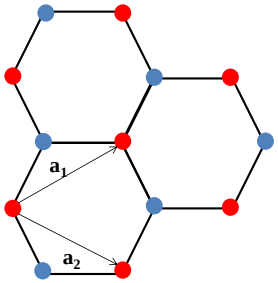

Figure 2.17: Lattice structure of graphene with two interpenetrating triangular lattices.

The honeycomb structure of graphene is made of a triangular lattice with a basis of two atoms per unit cell, designated as A and B (see figure 2.17). The 2D lattice vectors for this system in real space are given by [5, 77]

$$\mathbf{a_1} = \frac{a}{2}\left(3, \sqrt{3}\right) \qquad and \qquad \mathbf{a_2} = \frac{a}{2}\left(3, -\sqrt{3}\right) \tag{2.8.1}$$

where a= 1.42$\mathring{A}$ is the nearest neighbour carbon-carbon distance. In the reciprocal lattice space this leads to two inequivalent points, Dirac points, at the corners of the Brillouin zone and they are given by

$$\mathbf{K} = \left(\frac{2\pi}{3a}, \frac{2\pi}{3\sqrt{3}a}\right) \qquad and \qquad \mathbf{K'} = \left(\frac{2\pi}{3a}, -\frac{2\pi}{3\sqrt{3}a}\right) \tag{2.8.2}$$

These Dirac points play a role similar to the Γ points in direct band gap semiconductors like GaAs and play an important role in the electronic transport of graphene. The electronic band dispersion of graphene was first calculated by Wallace in 1947 within the tight binding model.

2.8.1.1 Band structure of graphene

Graphene has four valence electrons, out of which three form bonds with the three neighbouring carbon atoms in the plane. These three electrons forming co-planar bonds will not play any role in the conductivity while the fourth un-bonded electron determines the conductivity of graphene [75]. The wave functions for the bonded electrons in graphene can be written as

$$\frac{1}{\sqrt{3}}\left(\psi_c(2s) + \sqrt{2}\psi_c(\sigma_i 2p)\right) \tag{2.8.3}$$

where $\psi_c(2s)$ is the $2s$ wavefunction of carbon and $\psi_c(\sigma_i 2p)$ are the 2p wave functions of carbon which are in the direction σ_i joining the neighbouring carbon atoms in the plane. The fourth unbonded electron in the $2p_z$ state, which determines the conductivity in graphene, is perpendicular to the plane of the lattice. Thus graphene can be modelled as a system with one conduction electron in the $2p_z$ state. If *X(r)* is the normalized $2p_z$ orbital wave function for an isolated carbon atom, in the tight binding approximation, the wavefunction can be written as

$$\Psi = \phi_1 + \lambda\phi_2 \tag{2.8.4}$$

where

$$\phi_1 = \sum_A exp\left[2\pi i \mathbf{k}.\mathbf{r_A}\right] X(r - r_A) \tag{2.8.5}$$

and

$$\phi_2 = \sum_B exp\left[2\pi i \mathbf{k}.\mathbf{r_B}\right] X(r - r_B) \tag{2.8.6}$$

Here, the first and second sums are over all the lattice points generated from A and B respectively. In order to get the energy dispersion relation, the equations (2.8.5) and (2.8.6) are substituted in the relation (2.8.4) and multiply by ϕ_1 and ϕ_2 respectively, integrate and finally eliminate the λ from the resulting two equations.

i.e.

$$\begin{aligned}\langle\phi_1|\,H\,|\Psi\rangle &= \langle\phi_1|\,H\,|\phi_1\rangle + \lambda\,\langle\phi_1|\,H\,|\phi_2\rangle \\ &= \int \phi_1^* H \phi_1 d\tau + \lambda \int \phi_1^* H \phi_2 d\tau \\ &= H_{11} + \lambda H_{12}\end{aligned} \tag{2.8.7}$$

Similarly,

$$\begin{aligned}\langle\phi_2|\,H\,|\Psi\rangle &= \langle\phi_2|\,H\,|\phi_1\rangle + \lambda\,\langle\phi_2|\,H\,|\phi_2\rangle \\ &= \int \phi_2^* H \phi_1 d\tau + \lambda \int \phi_2^* H \phi_2 d\tau \\ &= H_{21} + \lambda H_{22}\end{aligned} \tag{2.8.8}$$

Since HΨ = EΨ,we also have

$$\begin{aligned}\langle\phi_1|\,H\,|\Psi\rangle &= E\,\langle\phi_1|\phi_1\rangle + E\lambda\,\langle\phi_1|\phi_2\rangle \\ &= E\int \phi_1^*\phi_1 d\tau + E\lambda \int \phi_1^*\phi_2 d\tau \\ &= E\int \phi_1^*\phi_1 d\tau \qquad\qquad \because \int \phi_1^*\phi_2 d\tau = 0 \\ &= EN\end{aligned} \tag{2.8.9}$$

and

$$\begin{aligned}\langle\phi_2|\,H\,|\Psi\rangle &= E\,\langle\phi_2|\phi_1\rangle + E\lambda\,\langle\phi_2|\phi_2\rangle \\ &= E\int \phi_2^*\phi_1 d\tau + E\lambda \int \phi_2^*\phi_2 d\tau \\ &= E\lambda\int \phi_2^*\phi_2 d\tau \qquad\qquad \because \int \phi_2^*\phi_1 d\tau = 0 \\ &= E\lambda N\end{aligned} \tag{2.8.10}$$

where $\int\phi_1^*\phi_1\ d\tau = \int\phi_2^*\phi_2\ d\tau =$ N is equal to the number of unit cells in the crystal since there is no overlap of the p_z wave functions centered at different atoms.

Combining equations (2.8.7), (2.8.8), (2.8.9) and (2.8.10), we get two equations

$$\begin{aligned} H_{11} + \lambda H_{12} &= EN \\ H_{21} + \lambda H_{22} &= E\lambda N \end{aligned} \tag{2.8.11}$$

which can be rewritten as a secular equation $\begin{vmatrix} H_{11} - EN & H_{12} \\ H_{21} & H_{22} - EN \end{vmatrix} = 0$ and gives

$$E = \frac{1}{2N}\left[H_{11} + H_{22} \pm ((H_{11} - H_{22})^2 + 4|H_{12}|^2)^{\frac{1}{2}}\right]. \tag{2.8.12}$$

By symmetry $H_{11} = H_{22}$ and also defining ${H_{11}}^{\dagger} = {H_{22}}^{\dagger} = \frac{H_{11}}{N} = \frac{H_{22}}{N}$ and ${H_{12}}^{\dagger} = \frac{H_{12}}{N}$, we get

$$E = H_{11}^{\dagger} \pm \left|H_{12}^{\dagger}\right| \tag{2.8.13}$$

The relation for energy E can be calculated by evaluating ${H_{11}}^{\dagger}$ and ${H_{12}}^{\dagger}$.

Now,

$$\begin{aligned} H_{11}^{\dagger} &= \frac{1}{N} H_{11} \\ &= \frac{1}{N} \sum_{A,A'} exp\left[-2\pi i \mathbf{k}.(\mathbf{r_A} - \mathbf{r_{A'}})\right] \\ &\qquad \times \int X^*(\mathbf{r} - \mathbf{r_A}) H X(\mathbf{r} - \mathbf{r_{A'}}) d\tau \end{aligned} \tag{2.8.14}$$

Considering only the nearest neighbour interaction among intrasublattice atoms (A-A or B-B), the above integral can be solved giving,

$$H_{11}^{\dagger} = E_0 - 2\gamma_0' \left(cos(2\pi k_y a) + 2cos(\sqrt{3}\pi k_x a) cos(\pi k_y a)\right) \tag{2.8.15}$$

where E_0 is the energy of an electron on the $2p_z$ state in carbon and ${\gamma_0}'$ is the next-nearest neighbour (intrasublattice A-A or B-B) hopping amplitude given by

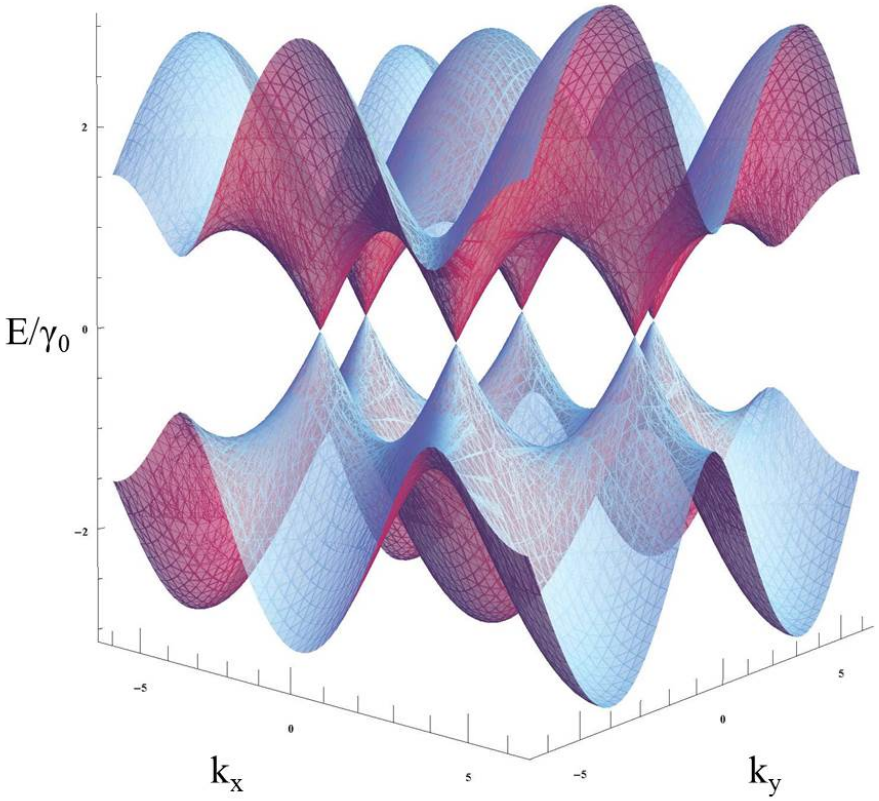

Figure 2.18: Energy-momentum dispersion relation for graphene.

$$\gamma_0' = \int X^*(r-\rho')(U-V)X(r)d\tau \;\; > 0 \; and \; \rho' = \mathbf{AA} = \mathbf{a_1} \tag{2.8.16}$$

Similarly, $H_{12}{}^{\dagger}$ can be solved to get

$$\begin{aligned} H_{12}^{\dagger} &= -\gamma_0 \left(exp[-2\pi i k_x (a/\sqrt{3})] + 2cos(\pi k_y a).exp[2\pi i k_x (a/2\sqrt{3})] \right) \\ |H_{12}|^2 &= \gamma_0^2 \left(1 + 4cos^2(\pi k_y a) + 4cos(\pi k_y a)cos(\sqrt{3}\pi k_x a) \right) \end{aligned} \tag{2.8.17}$$

The total energy E is

$$\begin{aligned} E_{\pm}(\mathbf{k}) &= H_{11}^{\dagger} \pm \left| H_{12}^{\dagger} \right| \\ &= E_0 - 2\gamma_0' \left(cos(2\pi k_y a) + 2cos(\sqrt{3}\pi k_x a)cos(\pi k_y a) \right) \\ &+ \gamma_0 \sqrt{\left(1 + 4cos^2(\pi k_y a) + 4cos(\pi k_y a)cos(\sqrt{3}\pi k_x a) \right)} \end{aligned} \tag{2.8.18}$$

Since $\cos^2(\theta) = \frac{1+cos(2\theta)}{2}$, the above equation can be simplified to

$$E_{\pm}(\mathbf{k}) = \pm\gamma_0\sqrt{3 + f(\mathbf{k})} - \gamma_0' f(\mathbf{k})$$
$$where \tag{2.8.19}$$
$$f(\mathbf{k}) = 2cos(2\pi k_y a) + 4cos(\sqrt{3}\pi k_x a)cos(\pi k_y a)$$

Close to the Dirac point ($\mathbf{k} \to \mathbf{K} + \mathbf{q}$, where $\mathbf{q} << \mathbf{K}$), the value of $\gamma_0' << \gamma_0$ ($0.02\gamma_0 \leq \gamma_0' \leq 0.2\gamma_0$) and hence the terms involving γ_0' can be neglected and the energy dispersion becomes [5, 75, 77]

$$|E_{\pm}(\mathbf{q}) - E_0| = \pm\sqrt{3}\pi\gamma_0 a|\mathbf{q}| = \pm\hbar v_F|\mathbf{q}| \tag{2.8.20}$$

i.e. graphene has a linear energy-momentum dispersion relation close to the Dirac point. This linear relation implies that

1. The conduction and valence bands intersect at q =0 with no energy gap, *i.e.* graphene behaves like a zero band-gap semiconductor with linear dispersion relation.

2. The Fermi velocity v_F calculated from the tight binding parameters $v_F = \frac{3\gamma_0 a}{2\hbar}$ gives a value of 10^8 cm/s

3. The existence of two equivalent but distinct sub-lattices leads to the existence of two linear branches of graphene dispersion relation indicating a pseudospin quantum number analogous to electron spin, *i.e.* graphene has a pseudospin index in addition to orbital and spin index. Thus the Schrodinger equation for the graphene carriers near the Dirac point becomes

$$-i\hbar v_F \sigma.\nabla\Psi(\mathbf{r}) = E\Psi(\mathbf{r}) \tag{2.8.21}$$

where σ is the vector of Pauli matrices and $\Psi(\mathbf{r})$ is the 2D spinor wavefunction corresponding to the pseudospin symmetry intrinsic to graphene.

4. The cyclotron mass defined as

$$m^* = \frac{1}{2\pi}\left[\frac{\partial A(E)}{\partial E}\right] \tag{2.8.22}$$

depends on the carrier density n. Since A(E), the area in k-space, is given by $\pi \mathrm{q(E)}^2 = \pi \frac{E^2}{v_F^2}$, the cyclotron mass for graphene is

$$m^* = \frac{\hbar\sqrt{\pi}}{v_F}\sqrt{n}. \tag{2.8.23}$$

The $\sqrt{n}$ dependence also implies that the charge carriers in graphene behave like massless Dirac fermions.

5. The zero band-gap nature of graphene allows the simple tuning of the Fermi-level with a gate voltage that not only allows the control of the carrier density but also the continuous control of the nature of the charge carriers (hole or electron). This enables the estimation of the charge carrier density from the gate capacitance C as

$$n = \frac{C}{e}V_g = \alpha V_g \tag{2.8.24}$$

For a SiO_2 gate with 300 nm thickness, $\alpha = 7.2\times10^{10}/(\mathrm{cm}^2\mathrm{V})$.

2.8.2 Electronic properties of bilayer graphene

Bilayer graphene can be considered as an intermediate system between the single layer graphene and bulk graphite. The system by itself is quite interesting because the integer quantum Hall effect is different from that of single layer graphene and also a gap can be opened in this system by the mere application of a perpendicular electric field, which is not possible in single layer graphene. Although, there could be different staking order for the bilayer graphene, the most common stacking order is the AB stacking, similar to the one seen in bulk graphite.

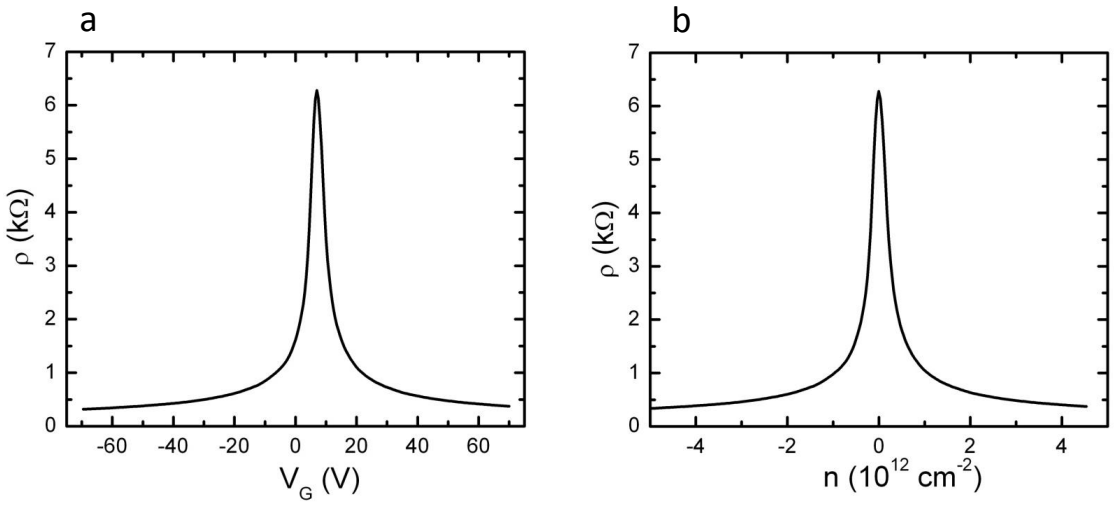

Figure 2.19: (a) Gate voltage tuning of the graphene's Fermi energy and (b) the same graph shown as a function of the charge carrier density n. The charge carrier density is calculated using equation (2.8.24).

2.8.2.1 Band structure of bilayer graphene

Similar to the single layer graphene, the tight-binding model can be used to determine the band structure of graphene [5, 77, 78]. Considering the AB stacking for bilayer graphene, the low wavelength low energy electronic structure of bilayer graphene can be described by the relation

$$E_{\pm}^2(q) = \left[V^2 + \hbar^2 v_F^2 q^2 + \gamma_\perp^2 \pm (4V^2\hbar^2 v_F^2 q^2 + \gamma_0^2\hbar^2 v_F^2 q^2 + \gamma_\perp^4/4)^{1/2}\right] \tag{2.8.25}$$

where $\gamma_\perp$ is the effective interlayer hopping energy and γ_0 and v_F are the intra layer hopping energy and Fermi velocity for the single layer graphene. For $V << \gamma_0$, equation 2.8.25, can be expanded as

$$E_{\pm}(q) = \pm[V - (2\hbar^2 v_F^2 V q^2)/\gamma_\perp + v_F^4 q^4/(2\gamma_\perp^2 V)] \tag{2.8.26}$$

From equation 2.8.26, it is clear that bilayer graphene has a gap at $q^2 \approx (2V^2/\hbar^2 {v_F}^2)$. i.e. the gap in the bilayer system depends on the applied bias voltage and for V =

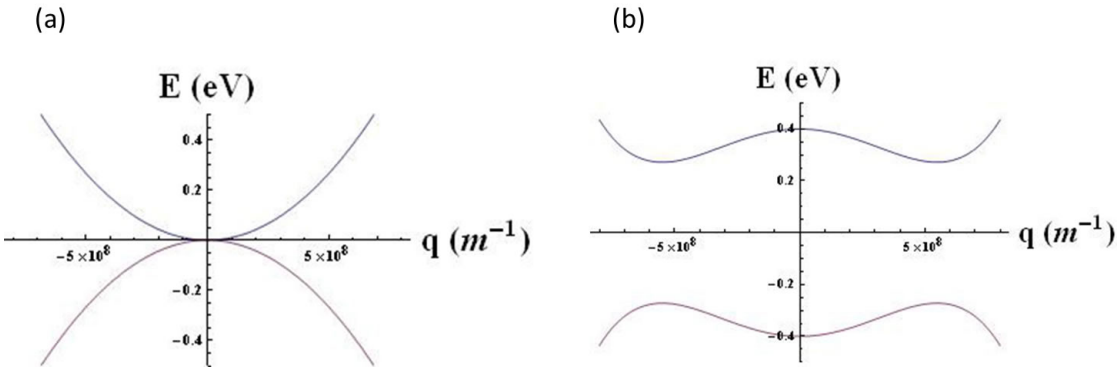

Figure 2.20: The band structure of graphene (a) without bias field i.e. V = 0 and (b) with bias field V $\neq$ 0. Here $\gamma_\perp = 0.4$ eV

0, the bilayer graphene is a gapless semiconductor with parabolic dispersion relation for small q given by

$$E_\pm(q) = \hbar^2 v_F^2 q^2/\gamma_\perp \tag{2.8.27}$$

The possibility of a band gap opening in bilayer graphene with the application of a bias voltage and the distinct parabolic band dispersion differentiates bilayer graphene from the monolayer graphene. Since bilayer graphene has a parabolic band dispersion similar to semiconductors, a comparison can be made between these systems.

2.8.2.2 Semiconductors and bilayer graphene: A comparison

The important differences between a 2D semiconductor and graphene are

1. 2D semiconductor systems have a large band gap ($>$ 1eV) while bilayer graphene is gapless at zero bias voltage with parabolic dispersion where the carriers change from electrons to hole at the Dirac or charge neutrality point, which makes graphene always metallic in nature.

2. Graphene systems, both single- and bi-layer systems, are chiral, while 2D semiconductors are non-chiral.

3. Graphene systems are the ideal 2D systems while 2D semiconductors are quasi-2D systems with average thickness of the order of ~ 5 nm. A 2D semiconductor loses its 2D nature at high carrier densities when higher sub bands are populated.

2.8.3 Graphene spintronics

Since graphene is made of carbon atoms, the intrinsic spin-orbit coupling, which has power law dependence ($\propto Z^4$), see section (2.5.1), is very weak. This implies that the spin dependent scattering due to the SO interaction is very weak and hence the spin diffusion/relaxation length should be comparatively large [79–83]. A second important reason for graphene to have long spin relaxation length is the weak hyperfine interactions. Only less than 1% of the carbon atoms consist of the C13 isotope of carbon which has a nuclear spin, and, hence the effect of the nuclear spins on the graphene spin transport is very weak.

Theoretically, spin relaxation length's of the order of 100μm has been predicted in graphene [82]. However, initial results in graphene spin transport showed spin relaxation length's of the order of 1 μm, and this has been attributed to additional spin dephasing due to factors like (1) the presence of adatoms like hydrogen, and (2) contribution from the surface optical phonons of the underlying substrate [82, 84–86]. Recent results have shown that utilizing an ultra flat substrate like boron nitride would enhance the observed spin relaxation length to the order of 10μm [87, 88]. Most importantly, the group of Albert Fert has shown that the predicted 100μm spin relaxation length could be reached by using ultra clean and high mobility epitaxial graphene samples [89].

2.8.3.1 Spin relaxation in graphene

Identifying the spin relaxation mechanism in graphene seems to be a herculean task. The initial experimental evidence pointed to the importance of the EY spin scattering mechanism in single layer graphene and multilayer graphene [90, 91, 94–96]. However, later experiments on bilayer graphene, discussed in this thesis, showed a completely unexpected result of DP spin scattering as the dominant spin dephasing mechanism [92, 93]. Later theoretical models developed based on these results suggest that the DP mechanism could be the dominant mechanism along with contributions from EY and spin-orbit interactions from random Rashba fields [82, 102–104]. A complete and thorough understanding of the relevant scattering mechanism in graphene is still lacking. However, in general, the spin scattering rate can be written as a combination of both EY and DP mechanisms as follows

$$\frac{1}{\tau_s} = \frac{1}{\tau_s^{EY}} + \frac{1}{\tau_s^{DP}} \tag{2.8.28}$$

Here,

$$\frac{1}{\tau_s^{EY}} = \frac{\Delta_{EY}^2}{\epsilon_F^2}\frac{1}{\tau_p} \tag{2.8.29}$$

and

$$\frac{1}{\tau_s^{DP}} = \frac{4\Delta_{DP}^2}{\hbar^2}\tau_p \tag{2.8.30}$$

where $\frac{1}{\tau_s^{EY}}$ is the spin scattering rate for the EY mechanism, $\frac{1}{\tau_s^{DP}}$ is the spin scattering rate for the DP mechanism, Δ_{EY} and Δ_{DP} are the spin-orbit coupling strength for EY and DP scattering, and τ_p is the momentum relaxation time. Substituting the equations 2.8.29 and 2.8.30, the relation 2.8.28 can be rewritten as

$$\frac{\epsilon_F^2\tau_p}{\tau_s} = \Delta_{EY}^2 + \frac{4\Delta_{DP}^2}{\hbar^2}\epsilon_F^2\tau_p^2 \tag{2.8.31}$$

The above relation can be used to fit the experimental data to determine the spin scattering rate specific to EY and DP mechanisms as shown in reference [97]

Since much work has already been performed on monolayer graphene [94–96,98–101], the aim of this work will be to understand the spin transport in graphene bilayers [105]. It should be noted that the differences in the bilayer graphene band structure with the possibility of a band gap opening, discussed in section 2.8.2, in principle could also result in a different spin scattering in bilayer graphene and, hence, studying the spin transport in this system will be important both from a fundamental and application point of view. We will also focus our effort in understanding the spin transport properties in graphene by enhancing its otherwise weak spin orbit coupling strength by functionalization.

Bibliography

[1] F. J. Jedema, Ph.D Thesis, University of Groningen (2002).

[2] N. Tombros, Ph.D Thesis, University of Groningen (2008).

[3] I. Zutic, J. Fabian, and S. Das Sarma, Rev. Mod. Phys. **76**, 323 (2004).

[4] J. Fabian, A. Matos-Abiague, C. Ertler, P. Stano, and I. Zutic, Acta. Phys. Slov. **57**, 565 (2007).

[5] A. H. Castro Neto, F. Guinea, N. M. R. Peres, K. S. Novoselov and A. K. Geim, Rev. Mod. Phys. **81**, 109 (2009).

[6] N. W. Ashcroft and N. D. Mermin, *Solid State Physics*,

[7] S. Gasiorowicz, *Quantum Physics*, John Wiley & Sons, Inc., (1974).

[8] M. Karplus and R. N. Porter, *Atoms and Molecules* (1970).

[9] N. F. Mott, Proc. Roy. Soc. **153**,669 (1936)

[10] N. F. Mott, Proc. Roy. Soc. **156**, 368 (1936)

[11] N. F. Mott, Adv. Phys. 13,325 (1964).

[12] I. A. Campbell, A. Fert, and A. R. Pomeroy, Phil. Mag. **15**, 977 (1967).

[13] A. Fert and I. A. Campbell, J. de Physiqye, Colloques **32**, C1 (1971).

[14] A. Fert and I. A. Campbell, J. Phys. F **6**, 849 (1976).

[15] P. C. van Son, H. van Kempen and P. Wyder, Phys. Rev. Lett. **58**, 2271 (1987).

[16] M. Johnson and R. H. Silsbee, Phys. Rev. Lett. **55**, 1790 (1985).

[17] J. Nogues and I. K. Schuller, J. Mag. Mag. Mater. **192**, 203 (1999).

[18] B. W. Alphenaar, S. Chakraborty and K. Tsukagoshi, *Electron Transport in Quantum Dots*, Ch-11, (2003).

[19] H. T. Man and A. F. Morpurgo, Phys. Rev. Lett. **95**, 026801 (2005).

[20] K. Ono, H. Shimada and Y. Ootuka, J. Phys. Soc. Jpn **67**, 2852 (1998).

[21] H. Shimada, K. Ono and Y. Ootuka, J. Appl. Phys. **93**, 8259 (2003).

[22] F. J. Jedema, A. T. Filip and B. J. van Wees, Nature **410**, 345 (2001).

[23] G. Schmidt, D. Ferrand, L. W. Molenkamp, A. T. Filip, and B. J. van Wees, Phys. Rev. B **62**, R4790 (2000).

[24] A. T. Filip, B. H. Hoving, F. J. Jedema, B. J. van Wees, B. Dutta, and G. Borghs, Phys. Rev. B **62**, 9996 (2000).

[25] E. I. Rashba, Phys. Rev. B **62**, R16267 (2000).

[26] M. Johnson, Phys. Rev. Lett. **70**, 2142 (1993).

[27] F. J. Jedema, H. B. Heersche, A. T. Filip, J. J. A. Baselmans and B. J. van Wees, Nature **416**, 713(2002).

[28] M. Johnson and R. H. Silsbee **37**, 5312 (1988).

[29] R. J. Elliott, Phys. Rev. **96**, 266(1954).

[30] Y. Yafet, *Solid State Physics* **14**, ed. F. Seitz and D. Turnbull (1963).

[31] M. I. D'yakonov and V. I. Perel, Sov. Phys. Solid State **13**,3023 (1972).

[32] G. L. Bir, A. G. Aronov and G. E. Pikus, Zh. Eksp. Teor. Fiz **69**, 1382 (1975); Sov. Phys. JETP **42**, 705 (1976).

[33] J. J. Sakurai and S. F. Tuan,*Modern Quantum Mechanics*, Addison-Wesley (1985).

[34] S. Takahashi, H. Imamura,and S. Maekawa,*Concepts in Spin Electronics*, Ed. S. Maekawa, 343 (2006).

[35] E. S. Garlid, Ph. D Thesis, The University of Minnesota (2010).

[36] R. Karplus and J. M. Luttinger, Phys. Rev. **95**, 1154 (1954).

[37] R. Winkler, *Spin-Orbit Coupling Effects in Two-Dimensional Electron and Hole Systems* (Springer 2003).

[38] N. F. Mott, Proc. Roy. Soc. Lon. Ser. A **124**, 425 (1929).

[39] N. F. Mott and H. S. W. Massey, *The Theory of Atomic Collisions*, Clarendon Press, Oxford (1965).

[40] J. Smit, Physica **24**, 39 (1958).

[41] L. Berger, Phys. Rev. B **2**, 4559 (1970).

[42] E. I. Rashba, Semiconductors **42** (2008).

[43] E. H. Hall, Philos. Mag. **10**, 301 (1880).

[44] A. W. Smith and R. W. Sears, Phys. Rev. **34**, 1466 (1929).

[45] M. I. D'yakonov and V. I. Perel, Phys. Lett. A **35**, 459 (1971).

[46] J. E. Hirsch, Phys. Rev. Lett. **83**,1834 (1999).

[47] Y. K. Kato, R. C. Myers, A. C. Gossard and D. D. Awschalom, Science **306**, 1910 (2004).

[48] J. Wunderlich, B. Kaestner, J. Sinova and T. Jungwirth, Phys. Rev. Lett. **94**, 047204 (2005).

[49] N. P. Stern, D. W. Steuerman, S. Mack, A. C. Gossard, D. D. Awschalom, Nat. Phys. **4**, 843 (2008).

[50] N. P. Stern, S. Ghosh, G. Xiang, M. Zhu, N. Samarth and D. D. Awschalom, Phys. Rev.Lett. **97**, 126603 (2006).

[51] H. Y. Inoue, K. Harii, K. Ando, K. Sasage, E. Saitoh, J. App. Phys. **102**, 083915 (2007).

[52] M. V. Costache, S. M. Watts, C. H. van der Wal and B. J. van Wees, Phys. Rev. B **78**, 064423 (2008).

[53] E. Saitoh, M. Ueda, H. Miyajima and G. Tatara, App. Phys. Lett. **88**, 182509 (2006).

[54] K. Harii, K. Ando, K. Sasage and E. Saitoh, Phys. Status Solidi (c) **4**, 4437 (2007).

[55] O. Mosendz, J. E. Pearson, F. Y. Fradin, G. E. W. Bauer, S. D. Bader and A. Hoffmann, Phys. Rev. Lett. **104**, 046601 (2010).

[56] T. Yoshino, Y. Kajiwara, K. Ando, H. Nakayama, T. Ota, K. Uchida, E. Saitoh, J.Phys: Conference Series **200**, 062038 (2010).

[57] K. Ando, H. Nakayama, Y. Kajiwara, D. Kikuchi, K. Sasage, K. Uchida, K. Ikeda and E. Saitoh, J. Appl. Phys. **105**,07C913 (2009).

[58] K. Ando, Y. Kajiwara, S. Takahashi, S. Meakawa, K. Takemoto, M. Takatsu and E. Saitoh, Phys. Rev. B **78**, 014413 (2008).

[59] K. Ando, S. Takahashi, K. Harii, K. Sasage, J. Ieda, S. Maekawa and E. Saitoh, Phys. Rev. Lett. **101**, 036601 (2008).

[60] K. Ando, J. Ieda, K. Sasage, S. Takahashi, S. Maekawa and E. Saitoh, Appl. Phys. Lett. **94**, 262505 (2009).

[61] K. Ando, S. Takahashi, J. Ieda, H. Kurebayashi, T. Trypiniotis, C. H. W. Barnes, S. Maekawa and E. Saitoh, Nat. Mater. **10**, 655 (2011).

[62] K. Ando and E. Saitoh, Nat. Comm. **3**,629 (2012).

[63] S. O. Valenzuela and M. Tinkham, Nature **442**, 176 (2006).

[64] T. Seki, Y. Hasegawa, S. Mitani, S.Takahashi, H. Imamura, S. M. J. Nitta and K. Takanashi, Nat. Mater. **7**, 125 (2008).

[65] T. Kimura, Y. Otani, T. Sato, S. Takahashi and S. Maekawa, Phys. Rev. Lett. **98**, 156601 (2007).

[66] L. Vila, T. Kimura and Y. Otani, Phys. Rev. Lett. **99**, 226604 (2007).

[67] J. Fan and J. Eom, Appl. Phys. Lett. **92**, 142101 (2008).

[68] M. Morota, K. Ohnishi, T. Kimura and Y. Otani, J. Appl. Phys. **105**, 07C712 (2009).

[69] T. Seki, I. Sugai, Y. Hasegawa, S. Mitani and K. Takanashi, Solid state comm. **150**,496 (2010).

[70] G. Mihajlovic, J.E. Pearson, M.A. Garcia, S. D. Bader and A. Hoffmann, Phys. Rev. Lett. **103**, 166601 (2009).

[71] D.A. Abanin, A. V. Shytov, L. S. Levitov and B. I. Halperin, Phys. Rev. B **79**, 035304 (2009).

[72] E. M. Hankiewicz, L. W. Molenkamp, T. Jungwirth, J. Sinova, Phys. Rev. B **70**, 241301(R) (2004).

[73] C. Brune, A. Roth, E. G. Novik, M. Konig, H. Buhmann, E. M. Hankiewicz, W. Hanke, J. Sinova, L. M. Molenkamp, Nat. Phys. **6**, 448 (2010).

[74] C. Brune, A. Roth, H. Buhmann, E. M. Hankiewicz, L. W. Molenkamp, J. Maciejko, X.-L. Qi, S.-C. Zhang, Nat. Phys. **8**, 485 (2012).

[75] P. R. Wallace, Phys. Rev. **71**, 622 (1947).

[76] K.S. Novoselov, A. K. Geim, S. V. Morozov, D. Jiang, Y. Zhang, S. V. Dubonos, I. V. Grigorieva, A. A. Firsov, Science **306**, 666 (2004).

[77] S. Das Sarma, S. Adam, E. H. Hwang, E. Rossi, Rev. Mod. Phys. **83**, 407 (2011).

[78] E. V. Castro, K. S. Novesolov, S. V. Morozov, N. M. R. Peres, J. M. B. Lopes dos Santos, J. Nilsson, F. Guinea, A. K. Geim and A. H. Castro Neto, Phys. Rev. Lett. **99**, 216802 (2007).

[79] C. L. Kane and E. J. Mele, Phys. Rev. Lett. **95**, 226801 (2005).

[80] C. L. Kane and E. J. Mele, Phys. Rev. Lett. **95**,246802 (2005).

[81] H. Min, J. E. Hill, N. A. Sinitsyn, B. R. Sahu, L. Kleinman and A. H. MacDonald, Phys. Rev. B **74**, 165310 (2006).

[82] D. Huertas-Hernando, F. Guinea, A. Brataas, Phys. Rev. B **74**, 155426 (2006).

[83] B. Trauzettel, D. V. Loss and G. Burkard, Nat. Phys. **3**, 192 (2007).

[84] A. H. Castro Neto and F. Guinea, Phys. Rev. Lett. **103**, 026804 (2009).

[85] H. Ochoa, A. H. Castro Neto and F. Guinea, Phys. Rev. Lett. **108**, 206808 (2012).

[86] C. Jozsa, T. Masssen, M. Popinciuc, P. J. Zomer, A. Veligura, H. T. Jonkman and B. J. van Wees, Phys. Rev. B **80**, 241403(R) (2009).

[87] P. J. Zomer, M. H. D. Guimaraes, N. Tombros and B. J. van Wees, Phys. Rev. B **86**, 161416(R) (2012).

[88] T. Maassen, J. J. van den Berg, E. H. Huisman, H. Dijkstra, F. Fromm, T. Seyller and B. J. van Wees **110**, 067209 (2013).

[89] B. Dlubak, M.-B. Martin, C. Deranlot, B. Servet, S. Xavier, R. Mattana, M. Sprinkle, C. Berger, W. A. De Heer, F. Petroff, A. Anane, P. Seneor and A. Fert, Nat. Phys. **8**, 557 (2012).

[90] C. Jozsa, T. Maassen, M. Popinciuc, P. J. Zomer, A. Veligura, H. T. Jonkman and B. J. van Wees, Phys. Rev. B **80**, 241403 (2009).

[91] T. Maassen, E. K. Dejene, M. H. D. Guimaraes, C. Jozsa and B. J. van Wees, Phys.Rev. B **83**, 115410 (2011).

[92] T.-Y. Yang, J. Balakrishnan, F. Volmer, A. Avsar, M. Jaiswal, J. Samm, S. R. Ali, A. Pachoud, M.Zeng, M. Popinciuc, G. Guentherodt, B. Beschoten and B. Oezyilmaz, Phys. Rev. Lett. **107**, 047206 (2011).

[93] W. Han and R. K. Kawakami, Phys. Rev. Lett. **107**, 047207 (2011).

[94] N. Tombros, C. Jozsa, M. Popinciuc, H. T. Jonkman and B. J. van Wees, Nature **448**, 571 (2007).

[95] N. Tombros, S. Tanabe, A. Veligura, C. Jozsa, M. Popinciuc, H. T. Jonkman and B. J. van Wees, Phys. Rev. Lett. **101**, 046601 (2008).

[96] W. Han, W. H. Wang, K. Pi, K. M. McCreary, W. Bao, Y. Li, F. Miao, C. N. Lau and R. K. Kawakami, Phys. Rev. Lett. **102**, 137205 (2009).

[97] P. J. Zomer, M. H. D. Guimaraes, N. Tombros, and B. J. van Wees, Phys. Rev. B **86**, 161416(R) (2012).

[98] W. Han, K. Pi, W. Bao, K. M. McCreary, Y. Li, W. H. Wang, C. N. Lau and R. K. Kawakami, Appl. Phys. Lett. **94**, 222109 (2009).

[99] K. Pi, W. Han, K. M. McCreary, A. G. Swartz, Y. Li, and R. K. Kawakami, Phys. Rev. Lett. **104**, 187201 (2010).

[100] W. Han, K. Pi, K. M. McCreary, Y. Li, J. I. Wong, A. G. Swartz and R. K. Kawakami, Phys. Rev. Lett. **105**, 167202 (2010).

[101] S. Cho, Y.-F. Chen and M. S. Fuhrer, Appl. Phys. Lett. **91**, 123105 (2007).

[102] C. Ertler, S. Konschuh, M. Gmitra, and J. Fabian, Phys. Rev. B **80**, 041405 (2009).

[103] P. Zhang and M. W. Wu, New J. Phys. **14**, 033015 (2012).

[104] P. Boross, B. Dora, A. Kiss, and F. Simon, arXiv:1211.0826.

[105] F. Guinea, New. J. Phys. **12**, 083063 (2010).

Chapter 3

Experimental Techniques

3.1 Introduction

In this chapter the experimental techniques required for the fabrication and characterization of graphene-based devices are described. The initial characterization of graphene is carried out by the optical contrast of the mechanically exfoliated flakes followed by Raman spectroscopy and atomic force microscopy. The details of these techniques are discussed. Since the device features have an average size of the order of a micrometer, the device fabrication requires the use of electron beam (e-beam) lithography to pattern devices on the graphene samples. The details of the device fabrication with e-beam and subsequent processes are also discussed.

3.2 Graphene: sample preparation

The graphene samples for the experiments discussed in this thesis are prepared either by the mechanical exfoliation of graphene from graphite using a scotch tape [1], or by the large area chemical vapour deposition of graphene using methane and hydrogen

as the precursor gas on a thin copper foil [2,10]. The preparation and characterization of these samples are discussed below:

3.2.1 Mechanical Exfoliation

In this method, graphene flakes are isolated by repeated 'peeling off' of graphite using a scotch tape [1]. The thin layers of graphene (mono, bi, tri etc.) are then transferred to a desired substrate (usually Si/SiO_2) by pressing the scotch tape on to the substrate. In general multiple graphene flakes of different thickness ranging from single layer to bulk graphite will be present on the substrate which is then identified by their optical contrast [4]. The observed thickness-dependent optical contrast of graphene flakes can be explained by considering the scenario of normal light incidence from air, with refractive index $\eta_0 = 1$, onto a trilayer structure of graphene/SiO_2/Si. Assuming the thickness of graphene as d_1, where d_1 is given by the out-of-plane extension of the π orbitals for single layer graphene ($d_1 = 0.34$ nm) with a refractive index $\eta_1(\lambda)$, the reflected light intensity can be written as

$$\begin{aligned} I(\eta_1) = |(&r_1 e^{i(\phi_1+\phi_2)} + r_2 e^{-i(\phi_1-\phi_2)} + r_3 e^{-i(\phi_1+\phi_2)} + r_1 r_2 r_3 e^{i(\phi_1-\phi_2)}) \\ &\times (e^{i(\phi_1+\phi_2)} + r_1 r_2 e^{-i(\phi_1-\phi_2)} + r_1 r_3 e^{-i(\phi_1+\phi_2)} + r_2 r_3 e^{i(\phi_1-\phi_2)})^{-1}|^2 \end{aligned} \tag{3.2.1}$$

where

$$\begin{aligned} r_1 &= \frac{\eta_0 - \eta_1}{\eta_0 + \eta_1} \\ r_2 &= \frac{\eta_1 - \eta_2}{\eta_1 + \eta_2} \\ r_3 &= \frac{\eta_2 - \eta_3}{\eta_2 + \eta_3} \end{aligned} \tag{3.2.2}$$

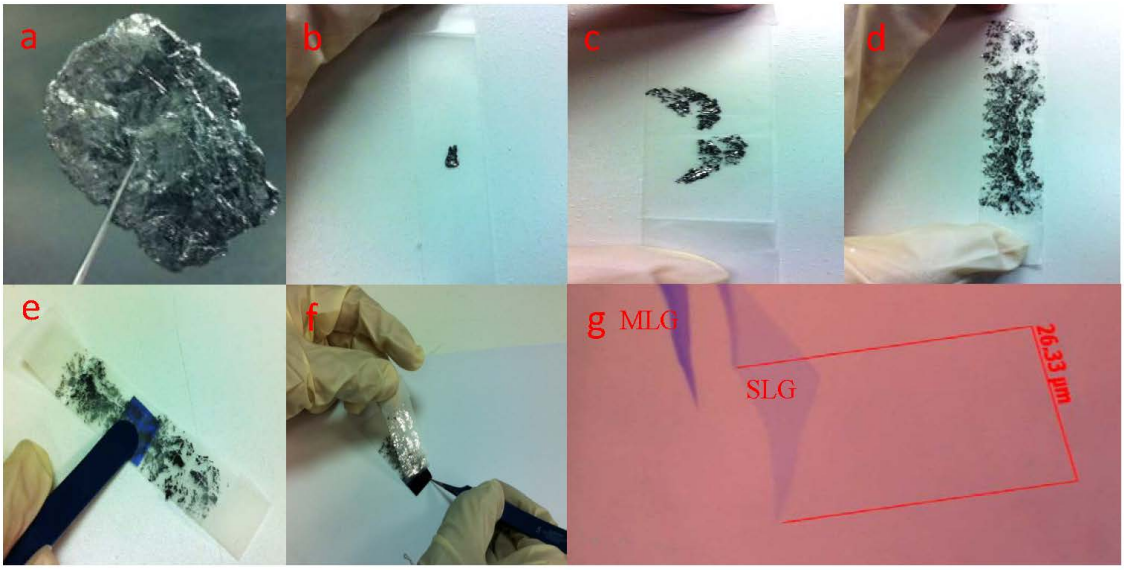

Figure 3.1: Optical image: (a-f) Various steps involved in the mechanical exfoliation of graphene using the 'scotch tape' method and (g) shows the different optical contrast for a single layer mechanically exfoliated graphene (SLG) adjacent to a multilayer graphene flake (MLG) on a 300 nm SiO_2 substrate.

are the relative indices of refraction and

$$\begin{aligned} \phi_1 &= \frac{2\pi\eta_1 d_1}{\lambda} \\ \phi_2 &= \frac{2\pi\eta_2 d_2}{\lambda} \end{aligned} \tag{3.2.3}$$

are the phase shifts due to changes in the optical path. Here, $\eta_1(\lambda)$, $\eta_2(\lambda)$ and $\eta_3(\lambda)$ are the refractive indices for graphene, SiO_2 of thickness d_2 and Si (assumed to be semi-infinite) respectively. Now the contrast C is defined as the relative intensity of the reflected light in the presence and absence of graphene and is given by

$$C = \frac{I(\eta_0 = 1) - I(\eta_1)}{I(\eta_0 = 1)} \tag{3.2.4}$$

and for the normal SiO_2 thickness of 300 nm, the contrast C for monolayer graphene is maximum for the green wavelength range [4] and can be used for the identification

of graphene flakes optically. Figure 3.1 (a-f) shows various steps involved in the mechanical exfoliation of graphene using the 'scotch tape' method and (g) shows the different optical contrast for a single layer mechanically exfoliated graphene (SLG) adjacent to a multilayer graphene flake (MLG) on a 300 nm SiO_2 substrate.

3.2.2 Large area growth of graphene by chemical methods

The mechanical exfoliation gives single layer graphene of few tens of micrometesr on average. However, for many practical applications, for e.g. transparent conducting electrodes for solar cells, touch screen panels, etc., large area graphene is required and hence methods where by scalable growth of graphene could be achieved need to be realized. The chemical growth of graphene using some form of carbon source is one of the plausible methods. The most common chemical methods to produce graphene are

1. Reduction of graphene oxides [5–7]: In the reduction of graphene oxide, graphite flakes are first oxidized which are then suspended in an aqueous solution. The solution is then passed through a membrane which gets covered with graphene sheets. These graphene sheets can then be transferred to a substrate of choice. One drawback of this method is that the obtained graphene film is often non uniform. Also these oxidized films need to be chemically treated to make them electrically conducting.

2. Growth by molecular beam epitaxy (MBE) [8, 9]: The epitaxial growth of graphene is an ideal method for growing high quality monolayer graphene and the films are grown by the thermal decomposition on the (0001) surface of 6H-SiC [8]. Recently, molecular beam epitaxy has also been used to grow graphene on metal surfaces. In this method, a graphite filament source is heated in ultra

high vacuum. As the filament is heated, the carbon atoms sublimate and get deposited on a metallic substrate forming a layer of graphene film [9]. Though the MBE method produces uniform large-area graphene, it requires ultra high vacuum for the synthesis of high quality films.

3. Growth by chemical vapour deposition (CVD) [2, 10, 10–12]: In the chemical vapour deposition method, the graphene films are grown on a metal foil like copper. For a high quality growth of single layer graphene, the copper foil is first heated at high temperature ($\approx$ 1000 C) in the CVD chamber which is then followed by the introduction of the reaction gas mixture of methane CH_4 and hydrogen H_2 for 30 minutes. Finally the sample is cooled down to room temperature in a hydrogen gas environment. The graphene grown on the Cu foil can then be etched away by using a solution of ferric chloride $FeCl_3$ or ammonium persulfate $(NH_4)_2S_2O_8$ and then transferred to any desired substrate.

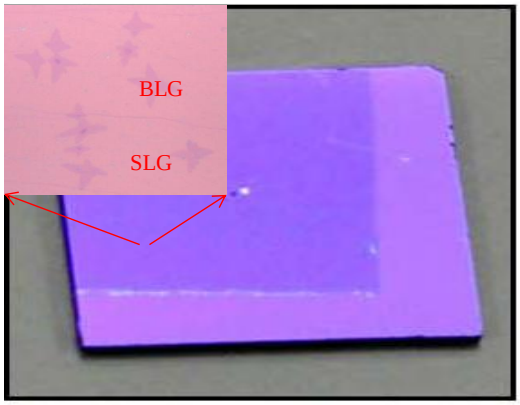

Figure 3.2: Optical image of CVD graphene grown after transferring onto a 300 nm SiO_2 substrate. The inset shows the magnified picture of the CVD graphene samples. In general, there are islands of bilayer graphene flowers in between the single layer graphene region.

The large area graphene samples used in our experiments are grown by the CVD method as explained in reference [10]. An optical picture of the large area CVD

graphene transferred onto a SiO_2 substarte is shown in figure 3.2. The inset in the figure clearly shows that these large area CVD graphene are predominantly of single layer, with some bilayer graphene flowers (5-10 μm in size) in between.

3.3 Graphene: sample characterization

In addition to the optical characterization explained in the previous section [4], the thickness and the quality of the graphene films (exfoliated and CVD) can be determined by Raman spectroscopy and atomic force microscopy (AFM) measurements.

3.3.1 Raman characterization

Raman spectroscopy has been used to study and characterize carbon-based materials [13,14]. For sp^2 carbons like graphene, the Raman spectroscopy gives information about crystalline size, the presence of sp^3 hybridization, chemical impurities, optical energy gap, elastic constants, doping, defects, strain in the sample, number of graphene layers etc. The most prominent features of the graphene Raman spectrum are the G band appearing at wavenumber 1580 cm^{-1} and the 2D band appearing (also known as G$'$ band) at wavenumber 2680 cm^{-1} for a laser excitation energy of 2.41eV. The G band is associated with the doubly degenerate in-plane transverse optical (iTO) and longitudinal optical (LO) phonon mode at the Brillouin zone center. The 2D (G$'$) band, which is sensitive to the number of layers, originates from the second order process involving two iTO phonons near the K point. As a function of the laser excitation energy the 2D band frequency upshifts linearly with the laser energy (E_{laser}) with a slope $\partial\omega_{2D}/\partial E_{laser}$ around 100 cm^{-1}/eV.

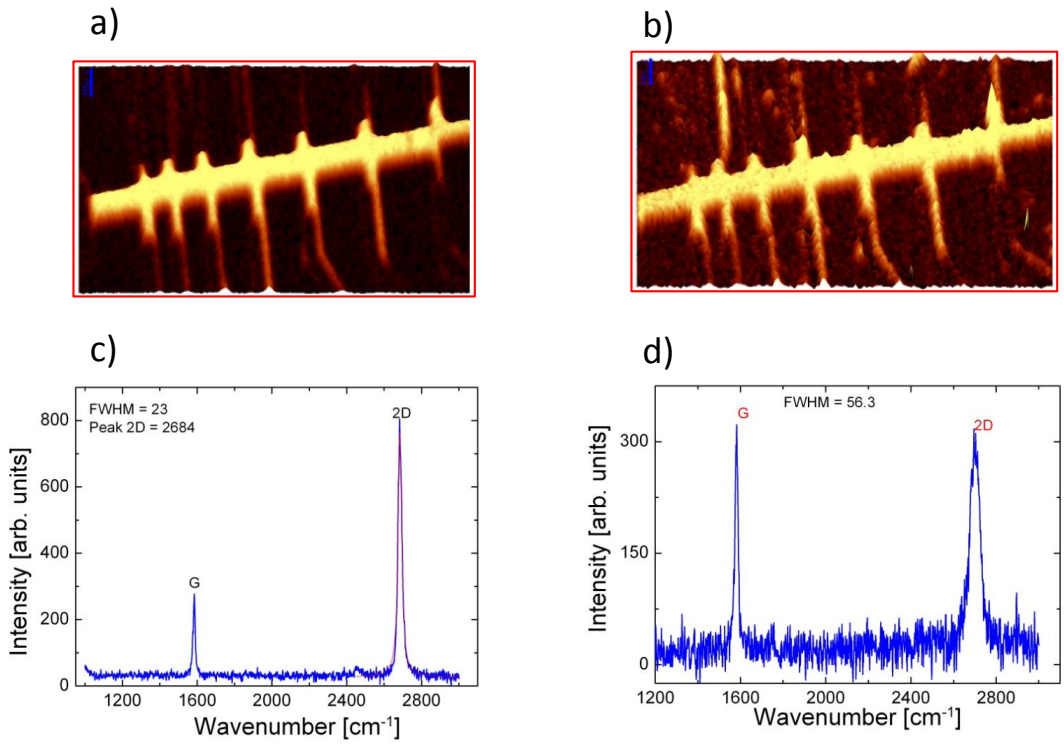

Figure 3.3: Raman mapping for the (a) 2D band and (b) G band for a SLG Hall bar device. (c & d) The Raman spectrum for a SLG and BLG showing G and 2D bands with a characteristic 2D band FWHM $\sim$ 23 cm^{-1} and 56 cm^{-1} respectively.

3.3.1.1 Determining the number of graphene layers

Specific to graphene, the Raman spectrum can be used to identify the number of layers in a sample by analyzing the nature of the 2D band spectrum. Since the present work focuses only on single layer (SLG) and bilayer (BLG) graphene samples, the discussion here will concentrate on how to differentiate single and bilayer graphene by Raman spectroscopy. For SLG, the 2D band shows a single Lorentzian feature with a full width at half maximum (FWHM) of $\sim$ 24 cm^{-1} [13, 14]. Moreover, for SLG the 2D peak intensity is larger than the G peak intensity [13, 14]. In BLG, the interaction between the two graphene layers causes splitting of the π and π^* bands into four bands allowing four different scattering process for phonons. These four scattering

processes give rise to the four Raman peaks in the 2D band of BLG, which can be fitted with four Lorentzians each with a FWHM of 24 cm^{-1}. Also, for BLG, the 2D and G band peak intensities are almost comparable [13, 14]. Figure 3.3 shows the Raman spectra for both SLG and BLG.

3.3.1.2 Determining the quality of graphene: Effect of disorder

The presence of disorder or covalently bonded adatoms (like hydrogen) breaks the crystal symmetry of graphene resulting in the activation of new vibrational modes such as the D-band in the Raman spectrum at wavenumber 1350 cm^{-1} for a laser excitation energy of 2.41 eV [13, 14]. By studying the evolution of the defect D-band intensity with respect to that of the G-band intensity, a rough estimate on the defect density is possible. Such analysis is quite important for our studies of weakly hydrogenated graphene, since this method allows an estimate of the percentage of hydrogenation in our samples. From the ratio of the intensities of the D and G-bands, the spatial separation, and hence the density, of hydrogen atoms can be calculated using the relations [15]

$$L_D^2(nm^2) = (1.8 \pm 0.5) \times 10^{-9} \lambda_L^4 (I_G/I_D) \tag{3.3.1}$$

$$n_i(cm^{-2}) = 10^{14}/(\pi L_D^2) \tag{3.3.2}$$

Figure 3.4 shows the evolution of the D-peak intensity with respect to the G-peak intensity for different percentage of covalently bonded hydrogen atoms on graphene lattice.

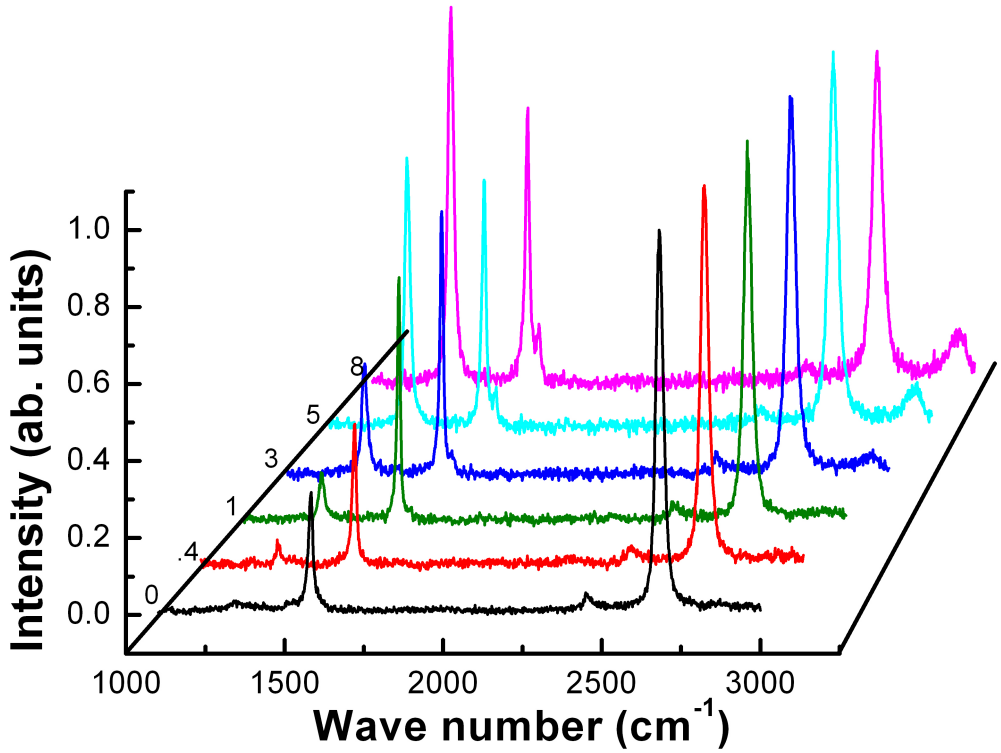

Figure 3.4: Evolution of the D-peak intensity at wavenumber 1350 cm^{-1} with increasing defect density. Here the defects are introduced by progressively hydrogenating the HSQ coated graphene samples by e-beam irradiation. The e-beam dose range from 0-8 mC/cm^2

3.3.2 Atomic Force Microscopy

Atomic force microscopy (AFM) can be used to characterize the surface morphology of graphene samples. Since graphene is only one atom thick, it easily conforms to any substrate on which it sits and hence the smoothness of the substrate is quite important for getting high quality samples. It should be noted that the exfoliation of graphene and the transfer of CVD graphene to SiO_2 by a wet transfer method could inadvertently introduce a thin layer of water ($\approx$ 0.75 nm thick) between the graphene and SiO_2 substrate. Hence AFM measurements performed on single layer graphene samples give a thickness of the order of 1 nm (0.75 nm water layer + 0. 3 nm thickness

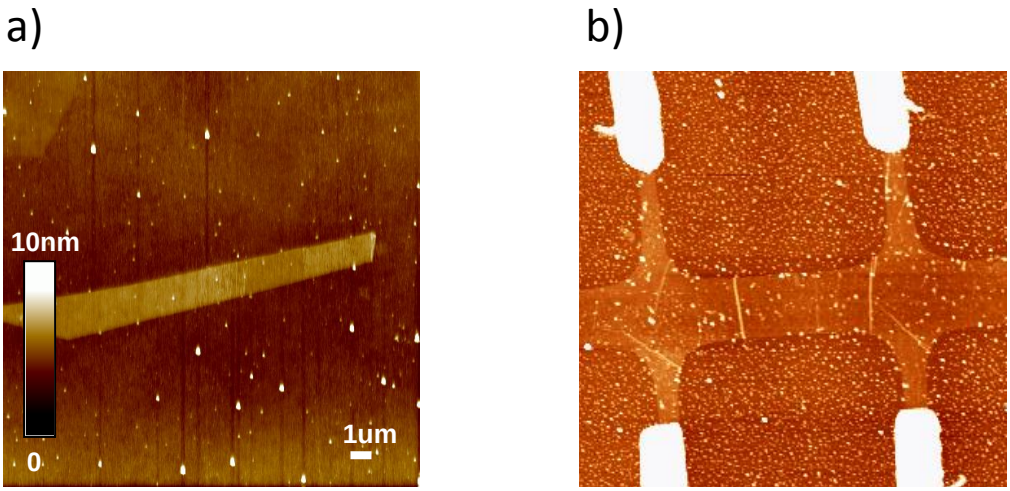

Figure 3.5: Atomic force microscopy (AFM) image of an (a) exfoliated graphene sample on a SiO_2 substrate. (b) CVD graphene sample on a SiO_2 substrate showing the presence of CVD growth specific ripples and wrinkles.

of graphene calculated from the out-of-plane extension of the π orbitals). Figure 3.5 shows the AFM image of graphene samples on a SiO_2 substrate. The AFM, thus, can also be used as an additional tool to the Raman spectroscopy for determining the thickness of the graphene flakes which is directly related to the number of layers.

Specific to the experiments detailed in this thesis, the AFM characterization plays a critical role in determining the quality of the tunnel barrier, MgO in our case, grown for the lateral spin-valve devices which is discussed in detail in the next section.

3.4 Tunnel barrier: Growth and characterization

As discussed in chapter 2, in the spin-valve geometry, to combat the "conductivity mismatch" and to enhance the spin polarization of the injected current into graphene

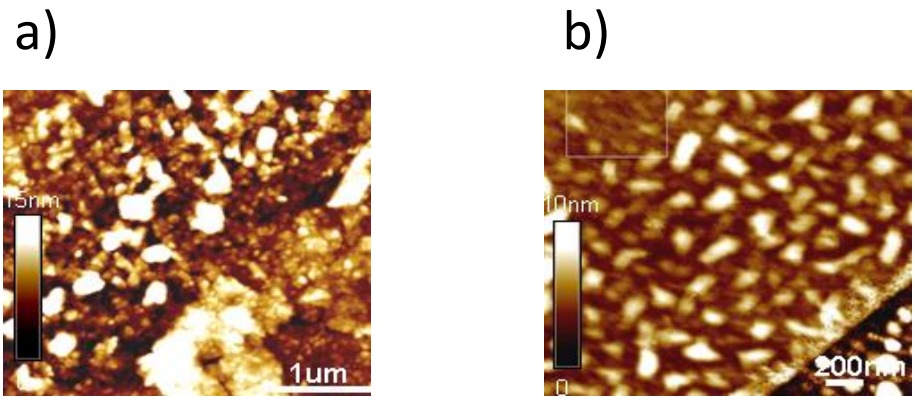

Figure 3.6: Atomic force microscopy (AFM) image of MGO-deposited graphene sample on a SiO_2 substrate. The image clearly shows that (a) without annealing or (b) with annealing only at 100° after MgO deposition results in a non-uniform growth of the tunnel barrier.

(non-magnetic material), a thin insulating layer is introduced between the ferromagnet and the non-magnetic material (graphene in our case). In all the spin-valve experiments discussed in this thesis a layer of magnesium oxide (MgO) 1-2 nm in thickness is used as the tunnel barrier. In the past, most of the research in graphene spin transport focussed on the use of Al_2O_3 tunnel barriers. The drawback with this tunnel barrier is that it requires cooling of the substrate to 77K after the deposition of Al under UHV conditions and subsequent oxidation under an oxygen environment (100mbar) to obtain a uniform Al_2O_3 layer [16]. In addition, the alumina tunnel barriers are amorphous [17]. The MgO tunnel barrier which is crystalline or poly-crystalline in nature, can be grown at room temperature under molecular beam epitaxy (MBE) conditions. It has also been predicted that the coherent tunnelling of electrons occurs in crystalline tunnel barriers, which allows us to expect a high spin polarization of the FM contacts with the MgO tunnel barrier [18].

3.4.1 Optimization of tunnel barrier growth

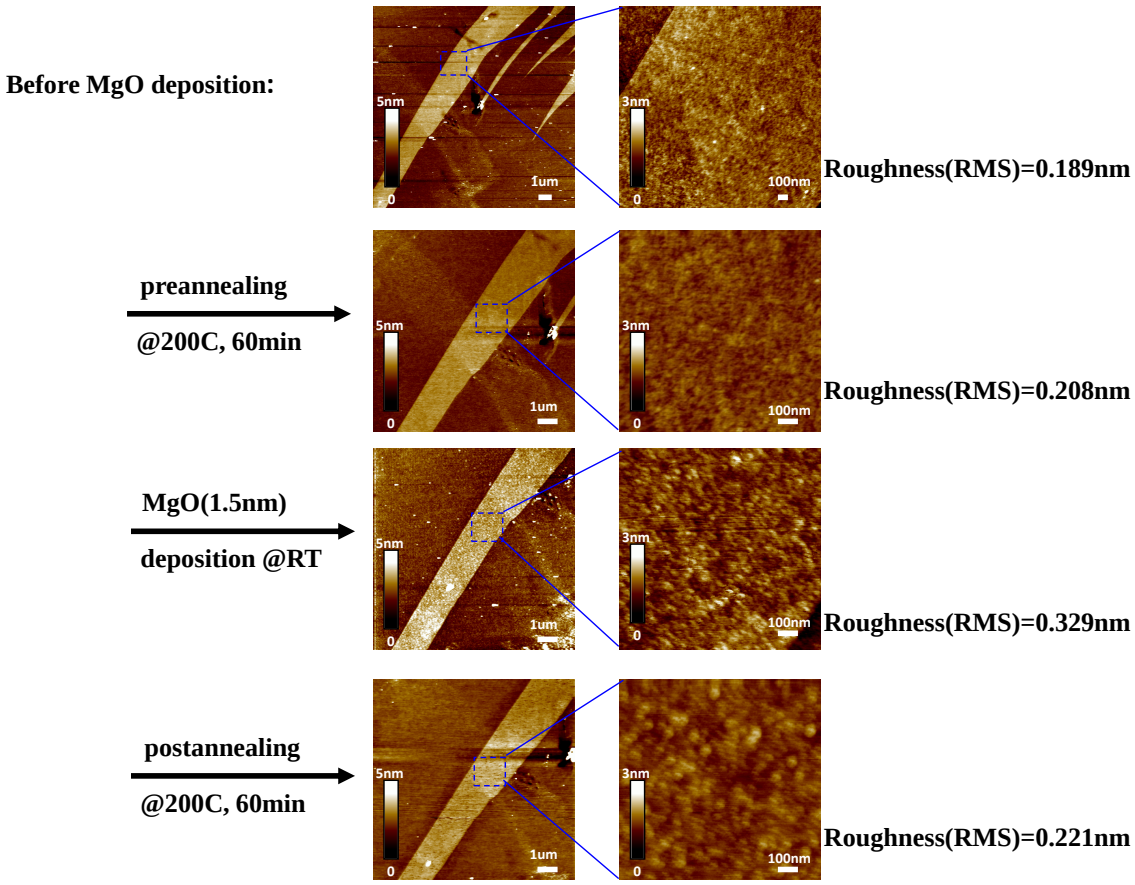

Figure 3.7: Atomic force microscopy (AFM) images showing the sequences and optimal conditions for the deposition of a uniform MGO layer on a graphene sample on a SiO_2 substrate.

The growth of a uniform and thin tunnel barrier depends on various conditions, like annealing of the samples before and after MgO deposition and the substrate temperature during deposition. Figure 3.6 shows the AFM topography image of the MgO-deposited graphene samples. The deposition is performed at room temperature. From the images it is clear that our initial attempts resulted in non-uniform and

discontinuous MgO growth. Based on further experiments, the optimal conditions for the deposition of uniform MgO layer were found to be

1. Pre- and post-annealing the graphene samples for one hour at 200°C in Vacuum (5×10^{-10}mbar)
2. Deposition to be performed at room temperature with deposition rate of 0.007 nm/s

The pre- and post-annealing steps allow a uniform MgO growth with typical thickness of 2nm and roughness of around 0.3nm on the graphene surface (see figure 3.7). Though we do not require TiO, as in ref [27], as a buffer layer for uniform MgO growth, we do see pinholes in our tunnel barrier and our spin transport is across this pinhole tunnel barrier.

3.5 Device Fabrication

Depending upon the type of experiments performed the device fabrication steps vary. In this thesis, there are mainly two types of measurements discussed: (1) the non-local spin-valve measurements, and (2) the spin Hall effect measurements in graphene/or functionalized graphene. Below a short description on the fabrication of devices for these experiments is discussed.

3.5.1 Spin-valves

1. Preparation (by exfoliation or by CVD method), identification and selection of graphene samples on SiO_2 substrate.
2. Deposition of thin layer (1-2 nm) of MgO tunnel barrier

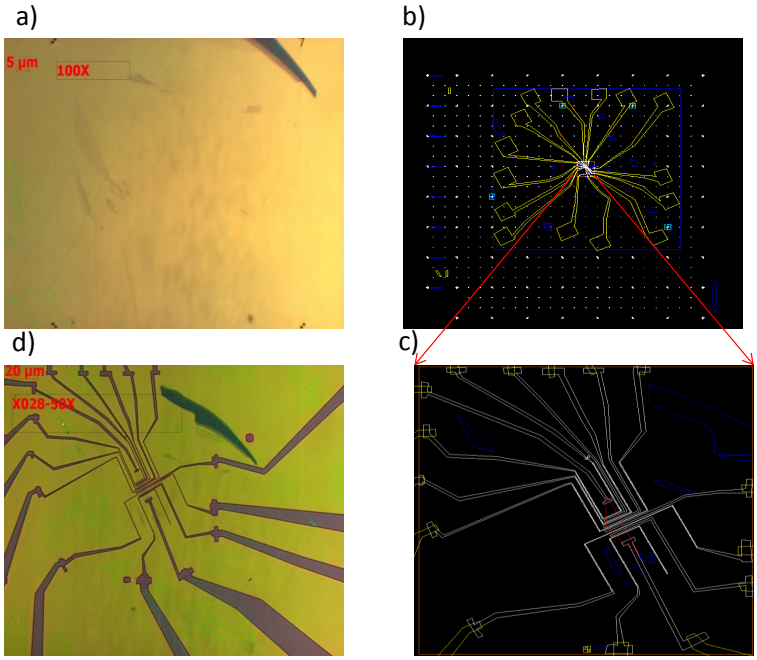

Figure 3.8: Optical images showing (a) the alignment markers adjacent to graphene samples (b & c) the Design CAD file with electrode patterns designed for the specific sample shown in (a) and (d) the final device structure on graphene after e-beam lithography and development.

3. Introducing alignment markers around graphene samples: The first major step in device fabrication is the introduction of alignment markers around the graphene samples. The alignment markers are important since it allows to identify the graphene samples precisely relative to the patterned markers, thus enabling the accurate design and patterning of electrode structures on graphene. For the devices presented in this thesis, the alignment markers around graphene are introduced using e-beam lithography. For this, the MgO/graphene/SiO_2/Si samples are first spin coated uniformly with poly-methyl methacrylate, PMMA (A5-950K), polymer. Now using the e-beam lithography technique, an array of markers is written on the PMMA. Figure 3.8 (a) shows the optical image of a graphene sample after alignment marker patterning.

4. Once the alignment markers are written, optical pictures of the sample at different magnifications are taken. These optical images are then used as a template to design the device electrode structure using Design CAD (see figure 3.8 (b & c)) and the Design CAD files are loaded to the nanometer pattern generator (NPGS) software used in our FEI Nano SEM 230 e-beam lithography machine.

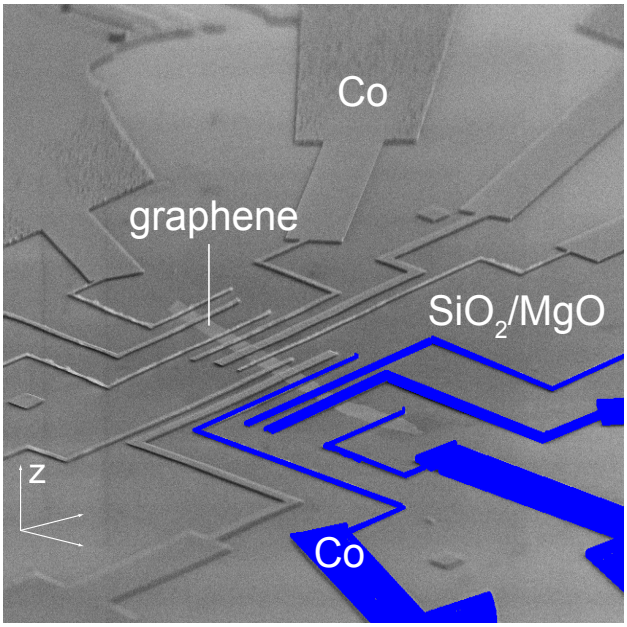

Figure 3.9: Scanning electron microscopy (SEM) image of a graphene spin-valve device after liftoff showing multiple junctions. The electrodes highlighted in blue represent one spin valve junction.

5. Patterning electrodes using e-beam lithography: In the e-beam lithography, electrons with energies in the range 10keV - 100 keV impinge on a sample protected by a polymer resist like PMMA. Here, the path of the e-beam can be controlled using a predefined design of the electrodes loaded on to the NPGS software. This is followed by the development of the resist in an appropriate developer. In our case, we use the positive resist PMMA. Hence, the developer

(Methyl isobutyl ketone (MIBK): Isopropyl alcohol (IPA = 1:1)) removes the exposed area of the resist on the sample while the remaining part of the sample remains covered with PMMA. Figure 3.8 (d) shows the final image of a graphene sample after e-beam lithography and development.

6. Deposition of metals and lift off: Following the e-beam lithography step, the samples are loaded into an e-beam evaporator to deposit Co electrodes. Here the presence of the undeveloped PMMA layer on the sample acts as a mask for the metal deposition. The Co electrodes $\sim$ 40 nm in thickness for our samples are deposited at a rate of 0.010 nm/s which is followed by the deposition of a capping layer of 3 - 5nm Au or Pt (0.005 nm/s deposition rate) to avoid the oxidation of the ferromagnetic Co electrodes. The samples are then immersed in cold Acetone overnight for liftoff of the electrodes. The SEM image of a Co/MgO/graphene/SiO_2/Si sample after lift off is shown in figure 3.9.

3.5.2 Spin Hall devices

The spin Hall device fabrication involves the following steps:

1. Preparation (by exfoliation or by CVD method), identification and selection of graphene samples on SiO_2 substrate.
2. Introducing alignment markers around graphene samples
3. Design the device electrode structure using Design CAD and the Design CAD files are loaded to the nanometer pattern generator (NPGS) software used in our FEI Nano SEM 230 e-beam lithography machine.
4. Patterning electrodes using e-beam lithography followed by development of the PMMA resist using Methyl isobutyl ketone (MIBK): Isopropyl alcohol (IPA) in

the ratio 1:1.

5. Deposition of metals and lift off: Following the e-beam lithography step, the samples are loaded into a thermal evaporator to deposit Chromium and gold (Cr/Au) electrodes. The thin layer (1-5 nm) of Cr is used as a buffer layer for the growth of Au electrodes on graphene, since Au alone does not stick well on the graphene samples. The steps 1 to 5 are identical to the spin-valve device fabrication except for the fact that in the spin Hall device fabrication the deposition of the MgO tunnel barrier as well as cobalt metal are not required. Also, the device geometry for spin Hall samples is different from the spin-valve samples.

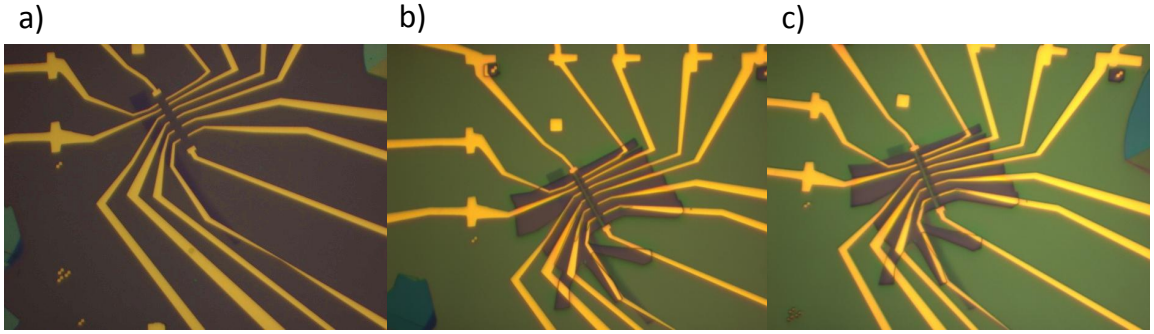

Figure 3.10: The optical images of graphene showing (a) the device after lift-off and prior to etch mask writing (b) the device after writing etch mask to define the Hall bar geometry and (c) the final Hall bar device after O_2 plasma etching of the etch channel.

6. Writing etch mask to pattern the Hall bar device structure: After the successful liftoff of the Cr/Au electrodes, additional e-beam lithography is performed following steps identical to 3 and 4. This additional e-beam step is to open up channels in the PMMA to define the geometry of the graphene samples to a Hall bar which is then followed by the oxygen plasma removal of the exposed graphene area. Figure 3.10 (a) shows the graphene device prior to etch mask

writing and figure 3.10 (b & c) shows the formation of the graphene Hall bar device after etch mask writing and the final device after oxygen plasma etching respectively.

3.6 Device Characterization

The graphene samples prepared (both spin-valves and spin Hall effect samples) are first characterized for the charge transport. For this the samples are glued to a 44-pin chip carrier with silver paste. Here, it is important to align the samples such that the contacts along the length will be aligned parallel to the magnetic field while performing spin-transport measurements later on. The device contact pads as well as the back gate are connected to the chip carrier via wire bonding. We use aluminum wire for wire bonding. The samples are then loaded to a vacuum probe which can be inserted into a variable temperature insert cryostat (1.6 K - 400 K) with magnetic field sweep capability of $\pm$ 9T or $\pm$16T. The basic charge transport measurements are performed with standard a.c. lock-in techniques at low frequencies ($\sim$ 13 Hz) under a four terminal set-up as shown in figure 3.11. The output sinusoidal signal from the lock-in is connected through a measurement box with standard resistors, so that a constant current can be passed to the graphene sample and the output voltage is measured by connecting the voltage terminals to the A and B input of the lock-in. If the output signal is small, the voltage probes can be connected to the lock-in inputs A and B through a pre-amplifier, which amplifies the voltage by 10. The back gate to the graphene sample is applied through a Keithley sourcemeter 6430 as shown in figure 3.11.

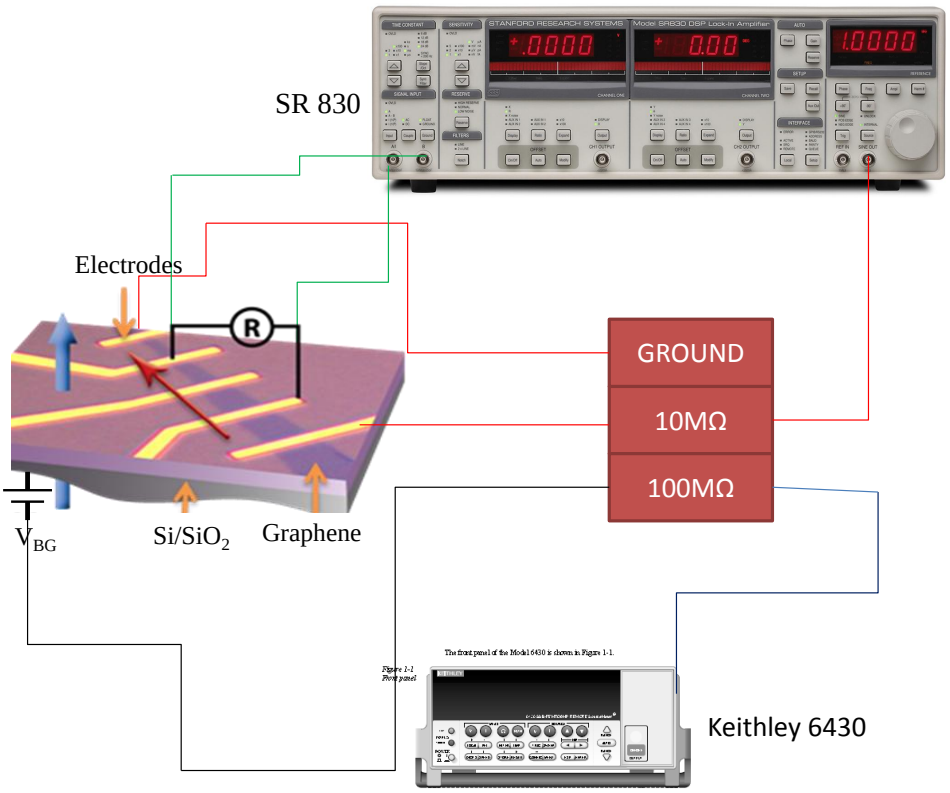

Figure 3.11: Schematics showing the measurement set-up for transport measurement.

3.6.1 Spin transport measurements

For both the spin-valve and spin Hall experiments discussed in this thesis, the measurements are performed employing a four terminal non-local geometry where the charge current path is isolated from the spin current path (see figure 2.5 (b) and figure 2.15). The standard a.c. lock-in technique is again employed for the measurements. Here, the most important aspect is that the samples are loaded onto a rotating probe, so that the field direction can be adjusted to be parallel or perpendicular to the sample by the mere rotation of the sample stage. A picture of the rotating sample holder fixed to the low temperature probe is shown in figure 3.12

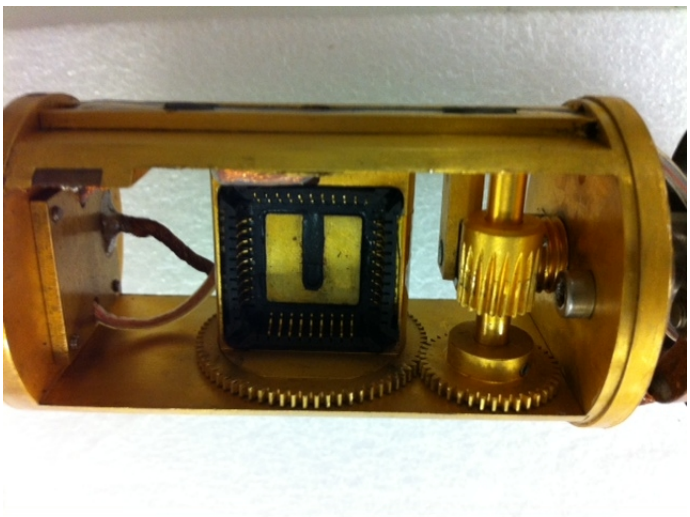

Figure 3.12: The sample holder in the rotating probe. The sample holder can be rotated to align the sample parallel to- or perpendicular to- the direction of the applied magnetic field.

Bibliography

[1] K. S. Novoselov, A. K. Geim, S. V. Morozov, D. Jiang, Y. Zhang, S. V. Dubonos, I. V. Grigorieva, A. S. Firsov, Science **306**, 666 (2004) .

[2] X. Li, W. Cai, J. An, S. Kim, J. Nah, D. Yang, R. Piner, A. Velamakanni, I. Jung, E. Tutuc, S. K. Banerjee, L. Colombo and R. S. Ruoff, Science **324**, 1312 (2009).

[3] S. Bae, H. Kim, Y. Lee, X. Xu, J.-S. Park, Y. Zheng, J. Balakrishnan, T. Lei, H. R. Kim, Y. I. Song,Y.-J. Kim, K. S. Kim, B. Ózyilmaz, J.-H. Ahn, B. H. Hong and S. Iijima, Nat. Nano. **5**, 574 (2010).

[4] P. Blake, E. W. Hill, A. H. Castro Neto, K.S. Novoselov, D. Jiang, R. Yang, T. J. Booth and A. K. Geim, Appl. Phys. Lett. **91**, 063124 (2007).

[5] B. C. Brodie, Phil. Trans. R. Soc. Lond. **149**, 249 (1859).

[6] H. A. Becerril, J. Mao, Z. Liu, R. M. Stoltenberg, Z. Bao and Y. Chen, ACS Nano. **2**, 463 (2008).

[7] H. C. Schniepp, J. L. Li, M. J. McAllister, H. Sai, M. Herrera-Alonso, D. H. Adamson, R. K. Prud'homme, R. Car, D. A. Saville, and I. A. Aksay, J. Phys. Chem. B **110**, 8535 (2006).

[8] C. Berger, Z. Song, T. Li, X. Li, A. Y. Ogbazghi, R. Feng, Z. Dai, A. N. Marchenkov, E. H. Conrad, P. N. First, W. A. de Heer, J. Phys. Chem. B **108**, 19912 (2004).

[9] E. Morean, F. J. Ferrer, D. Vignaud, S. Godey and X. Wallart, Physica status solidi (a) **207**, 300 (2010).

[10] K. S. Kim, Y. Zhao, H. Jang, S. Y. Lee, J. M. Kim, Kwang S. Kim, J.-H. Ahn, P. Kim, J.-Y. Choi and B. H. Hong, Nature **457**, 706 (2009).

[11] I. Jeon, H. Yang, S. H. Lee, J. Heo, D. H. Seo and J. Shin, ACS Nano **5**, 1915 (2011).

[12] J. Kim, M. Ishihara, Y. Koga, K. Tsugawa, M. Hasegawa and S. Iijima, Appl. Phys. Lett. **98**, 091502 (2011).

[13] L. M. Malard, M. A. Pimenta, G. Dresselhaus and M. S. Dresselhaus, Physics Reports **473**, 51 (2009).

[14] A. C. Ferrari, Solid state comm. **143**, 47 (2007)

[15] , L. G. Cancado, A. Jorio, E. H. Martins Ferreira, F. Stavale, C. A. Achete, R. B. Capaz, M. V. O. Moutinho, A. Lombardo,T. S. Kulmala and A. C. Ferrari, Nano Lett. **11**, 3190 (2011).

[16] N. Tombros, C. Jozsa, M. Popinciuc, H. T. Jonkman and B. J. van Wees, Nature **448**, 571 (2007).

[17] S. S. P. Parkin, C. Kaiser, A. Panchula, P. M. Rice, B. Hughes, M. Samant, S.-H. Yang, Nat. Mater. **3** , 862 (2004).

[18] P. Mavropoulos, N. Papanikolaou, and P.H. Dederichs, Phys. Rev. Lett. **85**, 1088 (2000)

[19] W. Han, K. Pi, K. M. McCreary, Y. Li, Jared J. I. Wong, A. G. Swartz and R. K. Kawakami, Phys. Rev. Lett. **105**,167202 (2010).

Chapter 4

Spin Transport Studies in Mono- and Bi-layer Graphene Spin-valves[1]

4.1 Introduction

The pioneering work of Tombros *et al.* [1] demonstrating micrometer long spin relaxation in single layer graphene at room temperature has made this wonder material a promising candidate for spintronics applications. However, most of the spin transport studies have focused on single layer graphene [1–13] while an equally important bilayer graphene has not received much attention. This is surprising since bilayer graphene has unique electronic properties which differ from that of monolayer graphene, *viz.* effective mass of charge carriers, electric field-induced band gap, and also from that of regular two-dimensional (2D) electron gases, for *e.g.* chirality [14, 15]. Moreover, unlike monolayer graphene, bilayer graphene has much more screening from charge impurities and hence scattering (both charge and spin) from such charge impurities is reduced [16]. Since charge and spin transport are highly correlated, it is natural to expect a profound difference in the nature of spin transport in bilayer graphene. The

[1]T-Y. Yang*, J. Balakrishnan* et al, Phys. Rev. Lett. 107, 047206 (2011)

aim of this chapter is to understand and compare the spin transport properties of single- and bi- layer graphene spin valves. The experiments and results discussed in this chapter are performed in collaboration with Prof. Gernot Güntherodt and Prof. Bernd Beschoten from II A Institute of Physics, RWTH Aachen University.

4.2 Characterization of mono- and bi- layer graphene spin-valves

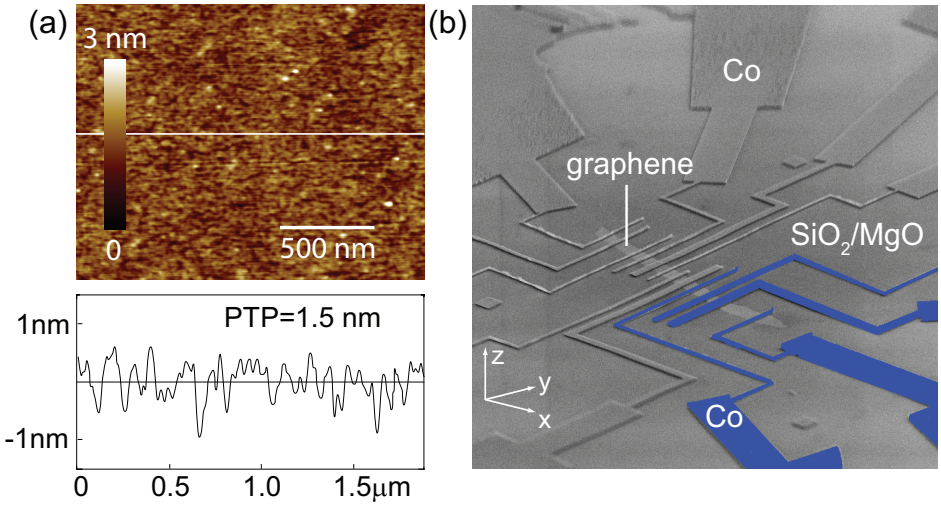

Figure 4.1: (a) Atomic force microscopy image of a bilayer graphene sample after MgO deposition: rms roughness $\sim$ 0.3 nm. (b) Scanning electron microscope image of a bilayer graphene sample with multiple non-local spin valves.

The single- and bi-layer exfoliated graphene spin-valve devices are prepared utilizing the method discussed in chapter 3. Unlike the previous reports on graphene spin-valves, where a thin layer of Al_2O_3 [1] was used as a thin tunnel barrier to combat conductivity mismatch between ferromagnetic electrode and graphene [17], in this work we utilize a thin (1.5 nm - 2 nm) magnesium oxide (MgO) tunnel barrier. The presence of crystalline/polycrystalline MgO tunnel barrier increases the spin injection

efficiency too [18]. Spin-valve devices are fabricated on two-types of MgO-covered exfoliated graphene samples using standard electron beam (e-beam) lithography. Figure 4.1 shows the AFM and SEM image of a bilayer graphene sample after MgO deposition. In type I samples, the thin MgO layer is deposited globally on the exfoliated graphene samples which is then followed by device patterning and Cobalt (Co) electrode deposition. In type II devices the electrodes are first patterned on the exfoliated graphene samples, followed by a single run deposition of MgO and Co; i.e. in type II devices the thin MgO tunnel barrier is present only locally beneath the ferromagnetic Co electrodes.

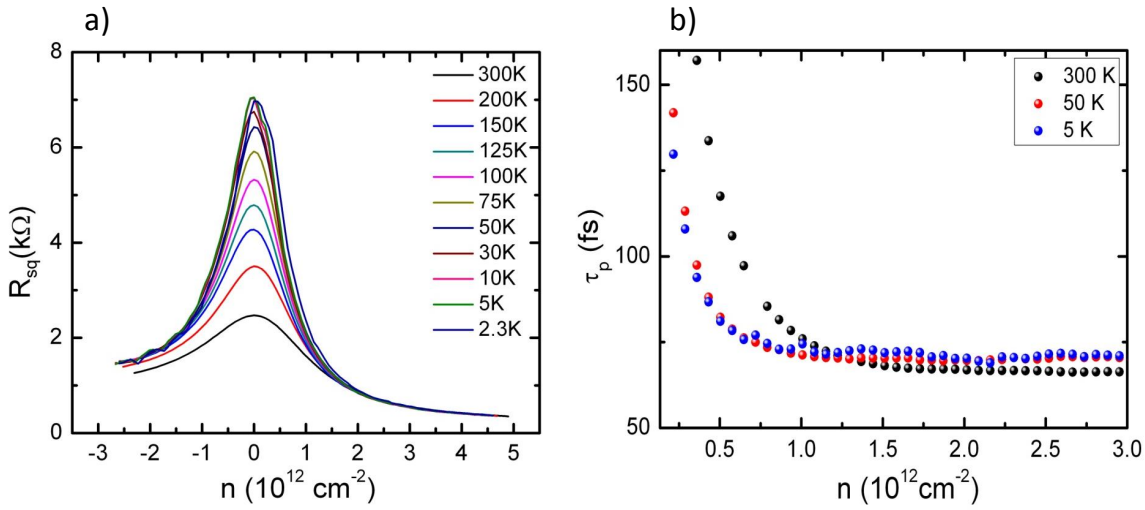

Figure 4.2: (a) Carrier density dependence of BLG resistivity for the temperature range 2.3-300 K. (b) The momentum relaxation time, $\tau_p = \sigma m^*/ne^2$ calculated in the Boltzmann framework as a function of carrier density n for BLG at T = 300 K (black circles), 50 K (red circles), and 5 K (blue circles).

Prior to any spin transport measurements, the graphene spin-valve devices are characterized for charge transport. Since the aim of our study is to differentiate and understand the spin transport properties of bilayer graphene, we will discuss in detail the bilayer graphene transport properties and the monolayer results will be discussed

when and where required for comparison. A characteristic R vs V_G curve clearly shows that, at the charge neutrality point, the bilayer graphene resistance shows significant insulating behaviour (see figure 4.2). This is unlike single layer graphene where the temperature dependence is weak even at the charge neutrality point. Such a thermally active behaviour at low temperature is attributed to the onset of an insulating phase at low temperature in bilayer graphene [19, 20]. In fact, such strong insulating behaviour also favours the importance of short range scatterers in bilayer graphene, since dominant Coulomb disorder in bilayer graphene is expected to produce a metallic behaviour even at low temperatures [20]. Moreover, the momentum relaxation time τ_p estimated from $\tau_p = \sigma \mathrm{m}^*/\mathrm{ne}^2$ where $\mathrm{m}^* = 0.03\mathrm{m}_e$) for our bilayer samples, shows a diverging behaviour near the charge neutrality point (see fig 4.2). This strong increase of τ_p near the charge neutrality point is qualitatively in good agreement with the recent experiments on bilayer graphene [21, 22]. Such an increase has also been attributed to the logarithmic corrections to τ_p arising from the presence of strong short range scatterers.

4.2.1 Spin injection and spin transport in bilayer graphene

4.2.1.1 Non-local spin valve measurements:

Once the devices are characterized for charge transport, four terminal non-local spin-valve measurements are performed. In the non-local geometry (see figure 4.3), the charge current path is separated from the active spin diffusion path, thus enabling the detection of pure spin currents [23].The non-local spin signal (ΔR), measured by sweeping the in-plane magnetic field in a loop from negative (-80 mT) to positive (+80 mT) and then back to negative values (-80 mT), corresponds to a value for the change in resistance between parallel and anti-parallel magnetizations of the injector

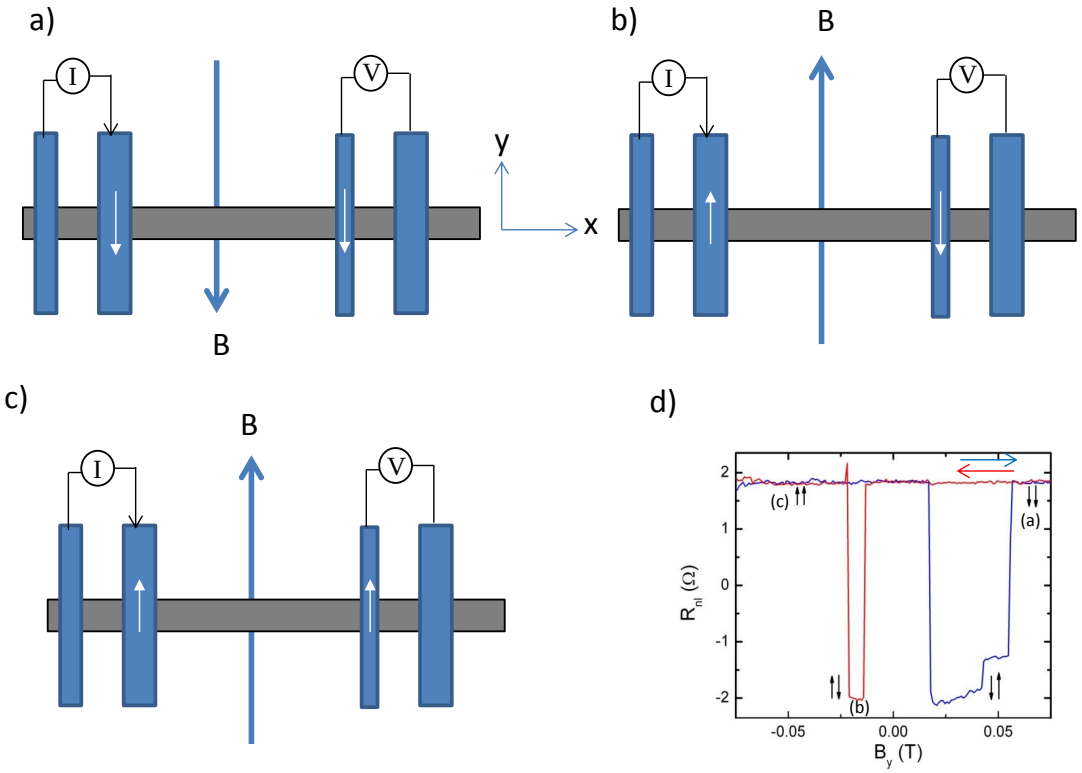

Figure 4.3: (a-c) Schematics of non-local spin valve showing the non-local measurement procedure in an in-plane magnetic field. Measurements are performed with standard a.c. lock-in techniques at low frequencies with currents in the range of 1-10 μA. (d) Non-local resistance for a bilayer graphene sample as a function of the in-plane magnetic field. The blue and red arrows show the field sweep direction while the black arrows show the relative magnetization orientations of the injector and detector electrodes.

and detector electrodes. A clear bipolar signal is observed at room temperature, with a positive value of the non-local resistance for parallel alignment of the electrodes' magnetization and a negative resistance for the anti-parallel alignment. For the device shown in figure 4.3(b), the measured ΔR has a value of around 4Ω at room temperature.

4.2.1.2 Hanle spin-precession measurements:

Though the non-local signal measured in the lateral spin-valve measurements suggests the diffusion of spins in bilayer graphene, for an unambiguous confirmation of the spin transport Hanle spin precession measurements in an external perpendicular magnetic field are performed [24]. For these experiments, first an in-plane magnetic field is applied along the easy-axis of the ferromagnetic electrode, so that the magnetization direction of the injector and detector are aligned parallel (anti-parallel). Now the non-local signal as a function of the perpendicular magnetic field will show an oscillatory behaviour due to the precession of the spins in an external magnetic field. Since, our transport is in the diffusive regime, the diffusing spins will travel different paths to reach the detector from the injector, which implies that there is a broadening of the spin precession angle. Hence the measured signal is the sum of the all the contributions from the diffusing spins and is given by [24]

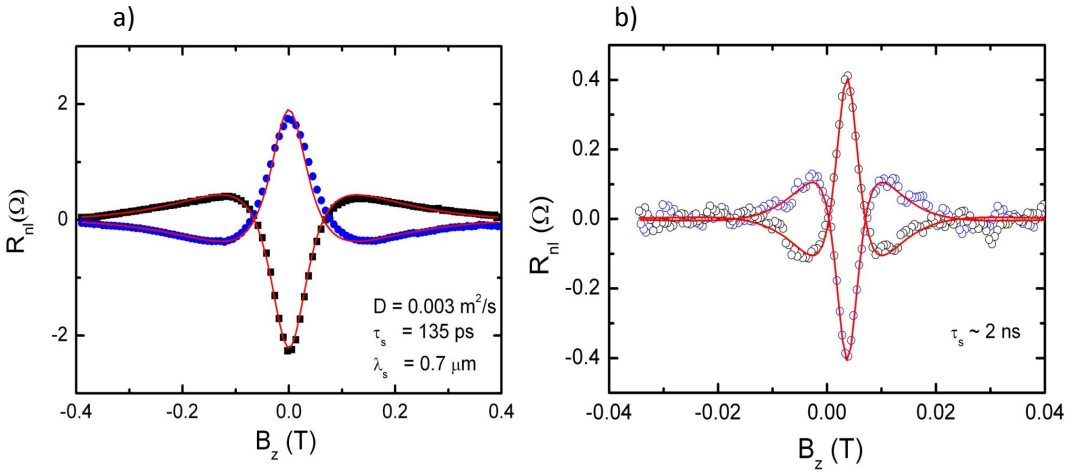

Figure 4.4: Hanle precession measurement for a perpendicular magnetic field B_z(T) sweep for (a) the same sample in figure 4.3(b) with $\mu \sim 2000\text{cm}^2/\text{Vs}$ and (b) for a sample with $\mu \sim 300\text{cm}^2/\text{Vs}$.

$$R_{nl} \propto \int_0^\infty \frac{1}{\sqrt{4\pi D_s t}} e^{\frac{-L^2}{4D_s t}} cos(\omega_L t) e^{\frac{-t}{\tau_s}} dt \tag{4.2.1}$$

Figure 4.4(a) shows the Hanle spin precession measurements for the same sample shown in figure 4.3(b). A fit to this signal using the above equation gives the values for the spin relaxation time τ_s = 135 ps and spin diffusion coefficient D_s = 0.0032 m^2/s. The spin relaxation length defined as $\lambda_s = \sqrt{\tau_s D_s}$, gives a value of around 0.7μm. Figure 4.4(b) shows the spin precession data for a sample of low mobility μ $\sim$ 300 cm^2/Vs with a spin relaxation time of τ_s = 2 ns. Comparing the figures 4.4 (a & b), it is clear that in addition to the characteristic oscillatory behaviour of the spin precession signal, in low mobility samples additional oscillations or wiggles are seen. One possibility for such wiggles is the contribution from orbital magnetoresistance as suggested by Tombros *et al.* [2, 25]. This induces a background which could contain non-periodic fluctuations as a function of the perpendicular magnetic field B_z. Since the estimated spin parameters are comparable to the values reported for monolayer graphene samples, we now focus to understand whether the spin scattering mechanisms in bilayer graphene are also similar to single layer graphene or not.

4.2.2 Identifying the spin scattering/dephasing mechanism in bilayer graphene

The possibility to open a band gap in bilayer graphene by the application of a gate voltage makes this material more promising from an application point of view. However, any future developments towards this requires a deeper understanding of the mechanisms that dephase spins in these systems. For this, we study the spin relaxation time τ_s as a function of (1) the charge carrier mobility μ, (2) the minimum conductivity σ_{min}, and (3) the charge carrier density n both at room temperature and at low temperature.

4.2.2.1 Spin relaxation time τ_s vs. charge carrier mobility μ:

As discussed in chapter 2, the major spin relaxation/dephasing mechanisms that could possibly dephase spins in graphene are (1) the Elliott-Yafet (EY) spin scattering mechanism [26] and (2) the D'yakonov-Perel' (DP) spin scattering mechanism [27]. In the EY spin scattering the conduction electron spins dephase via the momentum scattering by phonons or impurities; *i.e.* the spin relaxation time τ_s is directly proportional to the momentum relaxation time τ_p and hence to the mobility μ ($\tau_s \propto \tau_p \propto \mu$). In the DP spin scattering mechanism, in contrast to EY mechanism, the spin dephasing is due to the precession of spins under the influence of a local magnetic field (which varies in magnitude and direction with an average time period τ_p) induced by the spin-orbit coupling in the material between the momentum scattering events and translates to the condition that the spin relaxation time τ_s is inversely proportional to the momentum relaxation time τ_p and to the mobility μ ($\tau_s \propto 1/\tau_p \propto 1/\mu$). In order

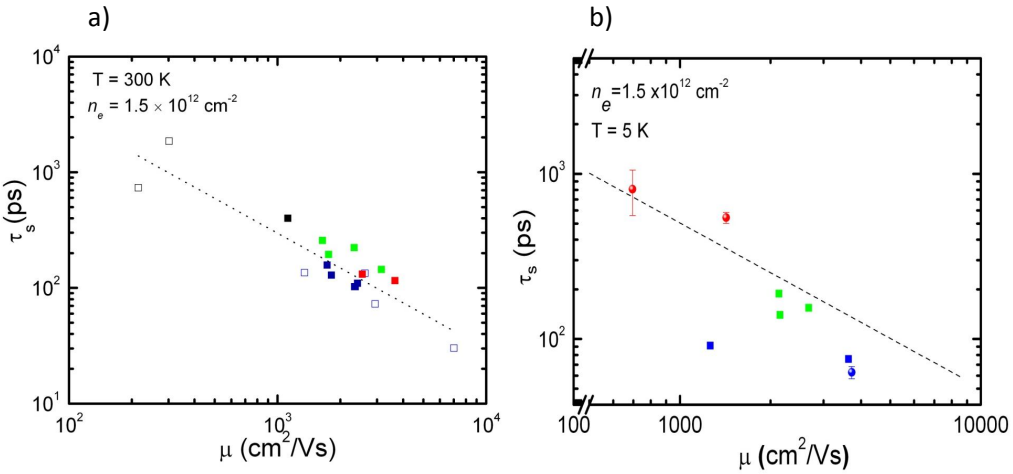

Figure 4.5: Results of Hanle precession measurements for BLG samples with mobility varying from 200-8000 cm^2/Vs .τ_s vs. μ plotted on a log-log scale (a) at room temperature and (b) at low temperature, 5 K.

to identify the dominant scattering mechanism in bilayer graphene, we selected 17

devices whose field effect mobilities varied by more than an order of magnitude from 200 cm^2/Vs to 8000 cm^2/Vs. Such mobility dependent studies have been useful in identifying spin scattering mechanisms in inorganic semiconductor systems [28]. Figure 4.5 shows the mobility dependence of the spin relaxation time in bilayer graphene at room temperature and at low temperature, respectively. The graph is plotted in log-log scale and shows a clear inverse relation of τ_s with μ. The samples with the highest mobility shows a $\tau_s \sim 30$ ps while the lowest mobility shows a $\tau_s \sim 2$ ns at RT. Such values of τ_s are longer by an order of magnitude when compared to the values reported so far in any single layer spin-valve experiments. Furthermore, this strong variation of τ_s with μ offers the most direct evidence for the correlation between spin and charge transport. Since higher mobility samples will typically involve higher momentum spin relaxation time $\mu \propto \tau_p$ in Boltzmann regime, the inverse dependence of τ_s on μ clearly demonstrates that the DP mechanism is the dominant spin scattering mechanism in bilayer graphene. Note that all the data are taken at electron density of $n = 1.5 \times 10^{12}/cm^2$. This is because near the charge neutrality point the mobility is ill-defined and an analysis based on the mobility dependence of the spin relaxation time is not valid.

4.2.2.2 Spin relaxation time τ_s vs. conductivity σ:

The dependence of the τ_s on the mobility of the sample cannot be employed for data acquired near the charge neutrality point. Hence, we study the dependence of the measured spin relaxation time at charge neutrality point as a function of the minimum conductivity $\sigma_{min}$of the samples. The value of the σ_{min} varies between clean and dirty samples and is higher for cleaner samples [29–31]. Figure 4.6 shows the τ_s vs.σ_{min} data at room temperature. The τ_s follows a $1/\sigma_{min}$ dependence indicating a higher spin relaxation time in dirtier samples. Therefore, this correlation is in good

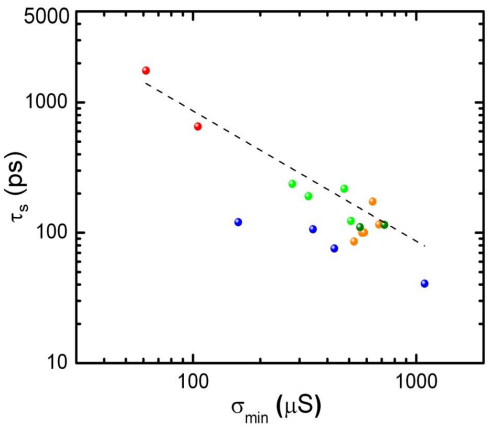

Figure 4.6: τ_s vs. σ_{min} for bilayer graphene samples of figure 4.5 at room temperature.

agreement with the above conclusion that the DP mechanism is dominant at room temperature. However, at low temperature the σ_{min} at the charge neutrality point is no longer a suitable parameter to study the scaling of τ_s. The available σ_{min} data scatters significantly at low temperature, but the overall variation in σ_{min} is small compared to room temperature. This is not surprising since σ_{min} is expected to take a disorder independent value of $3e^2/\pi h$ at $T = 0$ K [32].

An alternative way to conclude about the DP mechanism at CNP

An alternative way to look at the scattering mechanism is to compare the transport at the charge neutrality point with the transport in disordered semiconductors [33]. Near the metal-insulator transition (metallic part of the critical regime), the reduced conductivity is due to the non-Gaussian diffusion and hence the conductivity is proportional to the diffusion coefficient. Also, from the definition of the electron spin relaxation time, we have

$$\tau_s^{-1} = \int_0^\infty \langle \Omega_k(0)\Omega_k(t)\rangle dt \approx \Omega^2\tau \tag{4.2.2}$$

where Ω is the Larmor frequency and τ is the relaxation time.

Now near the charge neutrality point, the electrons can be considered to be in a

localized state and the transport is due to the tunnel hopping from one localized state to the next. This implies that we can define electron trajectory, wave vector and velocities for each trajectory and hence the diffusion coefficient can be defined as

$$D = \int_0^\infty \langle v(0)v(t)\rangle dt \approx \langle v^2 \rangle \tau \tag{4.2.3}$$

substituting equation (4.2.3) into (4.2.2) gives

$$\tau_s^{-1} \approx \Omega^2 \tau \approx D \frac{\Omega^2}{\langle v^2 \rangle} \propto \sigma \tag{4.2.4}$$

i.e. close to the charge neutrality point the spin relaxation time τ_s is inversely proportional to the conductivity and hence to the mobility of the sample, suggesting the dominance of DP spin scattering mechanism close to the neutrality point.

4.2.2.3 Spin relaxation time τ_s vs.charge carrier density n

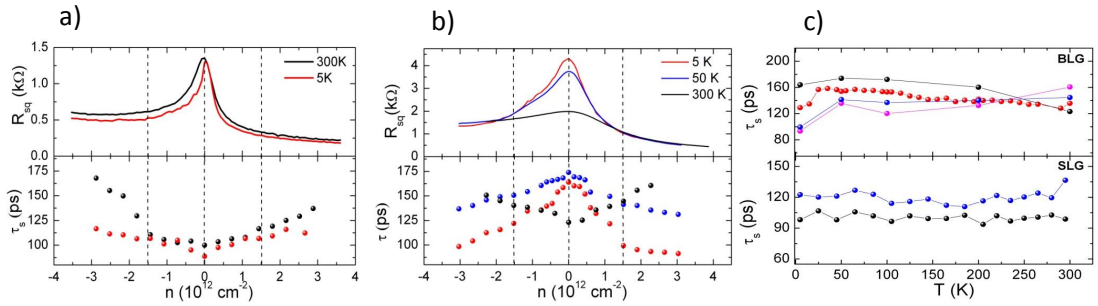

Figure 4.7: (a) Upper panel: Resistance vs. n for single layer graphene at 5 K and at 300 K; Lower panel: τ_s vs. n for T = 300 K (black circles) and 5 K (red circles), (b) Upper panel: Resistance vs. n for bi layer graphene at 5 K, 50 K and at 300 K; Lower panel: τ_s vs.n for T = 300 K (black circles), 50 K (blue circles), and 5 K (red circles) and (c) Upper panel: τ_s vs. T for four densities n = CNP (black circles), $0.7 \times 10^{12}/\text{cm}^2$ (red circles), $1.5 \times 10^{12}/\text{cm}^2$ (blue circles) and $2.2\times 10^{12}/\text{cm}^2$ (green circles) for bilayer graphene; Lower panel: τ_s vs. T for two densities n = CNP (black circles), $1.5 \times 10^{12}/\text{cm}^2$ (blue circles) for single layer graphene.

Since at low temperature (LT) σ_{min} is not a good parameter, we are left with the density dependence of τ_s to elucidate on what happens near the charge neutrality point. Figure 4.7 shows the comparison between the single and bilayer graphene non-local signal density and temperature dependence. It is clear that not only the density dependence but also the temperature dependence of the non-local signal is very distinct for bilayer graphene from that of the single layer graphene. For bilayer graphene at room temperature the density dependence of the spin relaxation time τ_s shows a minimum at the charge neutrality point. As the temperature is decreased this minimum in τ_s is gradually suppressed and the slope of τ_s(n) changes sign. Finally, at T = 5 K the density dependence shows a strong enhancement ($\geq$ 50 %) near the charge neutrality point. Now from references [21, 22] and from figure 4.2 (b), it is clear that the momentum relaxation time shows a diverging behaviour as we go close to the charge neutrality point. To understand the scattering mechanism at the charge neutrality point, we compare the density dependence of τ_p to that of τ_s close to the charge neutrality point. At room temperature, this clearly suggests an inverse relation between τ_p and τ_s. However, at low temperature, both τ_p and τ_s show similar density dependence and this correlation suggests a transition from DP to EY spin scattering mechanism at low temperature, around the charge neutrality point.

In order to unambiguously determine which scattering mechanism dominates, we also calculate the quantities $\tau_s\tau_p$ and $\frac{\tau_s}{\tau_p}$ in the density range n = 1-3 $\times$ $10^{12}/\text{cm}^2$. In this density range, at RT, the $\tau_s\tau_p$ almost remains a constant while $\frac{\tau_s}{\tau_p}$ show an increase of 28% with increase in charge density. This is consistent with the dominance of DP mechanism away from the charge neutrality point in bilayer graphene at RT, because for DP $\tau_s \propto \tau_p^{-1}$. However, at low temperature both quantities vary by a comparable amount, i.e. both $\tau_s\tau_p$ and τ_s/τ_p show in the density range 1- 3 $\times$ $10^{12}/\text{cm}^2$ a decrease by $\sim$ 10 % at 50 K and by $\sim$ 25 % at 5 K. This makes it difficult to deduce the dominant scattering mechanism from density dependence alone.

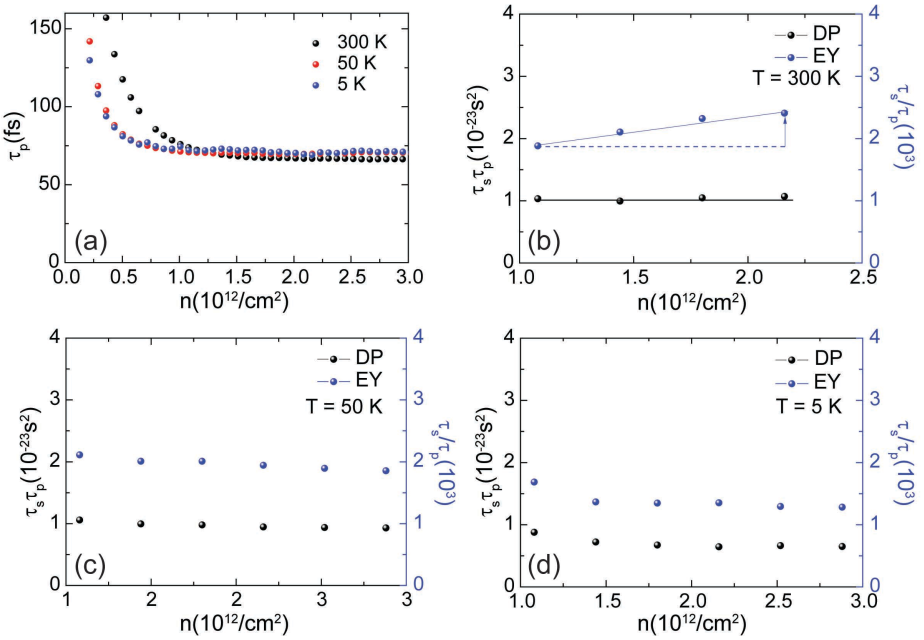

Figure 4.8: (a) The momentum relaxation time, $\tau_p = \sigma m^*/ne^2$ calculated in the Boltzmann framework as a function of carrier density n for BLG at T = 300 K (black circles), 50 K (red circles) and 5 K (blue circles); (b, c and d) The carrier density dependence of the product $\tau_s\tau_p$ and the ratio τ_s/τ_p, which identifies the dominant scattering mechanism for T = 300 K, 50 K and 5 K, respectively. A constant value for $\tau_s\tau_p$ indicates DP while a constant value for τ_s/τ_p indicates EY mechanism. The arrow in figure b shows the significant change in the ratio τ_s/τ_p with density at RT when compared to the change in$\tau_s\tau_p$.

4.2.2.4 Effect of electron-hole puddles at the charge neutrality point

As discussed, the logarithmic corrections arising from the presence of strong short-range scatterers, causes a strong increase in τ_p near the charge neutrality point in bilayer graphene. Thus, a comparison of the τ_p and τ_s values indicates a transition from DP to EY like spin scattering in bilayer graphene at LT near the charge neutrality point. Moreover, the presence of electron-hole puddles for these bias voltages may also suggest the possibility of spin scattering via the Bir-Aronov-Pikus (BAP) mechanism [34]. If such electron-hole scattering together with spin flip is present, the spin

scattering is expected to happen only at the boundaries of electron-hole puddles and not uniformly across the samples. This is because the BAP spin scattering requires a significant overlap in the electron and hole wave functions. Although we cannot completely rule out spin scattering of BAP-type, we believe that this is not likely because it is usually only relevant in hole-doped systems with large effective mass of the charge carriers [35]. However, precise theoretical studies on the electron-hole scattering near the CNP are required to fully estimate the influence of electron-hole exchange interaction in spin scattering.

Therefore, to sum up, at low temperatures the scattering mechanism is determined only by the mobility dependence of the spin relaxation time. Since the momentum scattering mechanism is different in bilayer graphene at low temperature near the charge neutrality point, it is not surprising that the spin relaxation mechanism is also different. However, we note that there remains to be resolved the fact that why there is a transition from DP to EY spin scattering mechanism in bilayer graphene at low temperature and at the charge neutrality point. We believe one possible explanation could be related to the thermally activated behaviour of charge carriers in this density regime in bilayer graphene.

4.2.3 Estimate of the spin-orbit coupling strength in bilayer graphene

Our analysis of the dependence of the spin relaxation time as a function of mobility, minimum conductivity and charge carrier densities at room temperature and at low temperature, clearly suggest that away from the charge neutrality point, the DP spin scattering mechanism dominates. This knowledge of the dominant spin scattering mechanism allows for an estimate of the spin-orbit coupling strength in bilayer

graphene. Since DP mechanism involves the precession of spins in a local magnetic field, the spin-orbit coupling strength can be calculated from the Larmor frequency as

$$\frac{1}{\tau_s} = \Omega_{eff}^2 \tau_p = \frac{4\Delta^2}{\hbar^2}\tau_p \tag{4.2.5}$$

where Ω_{eff} is the Larmor frequency of the precessing spins and Δ is the spin orbit coupling strength [36].The Larmor frequency can be calculated in two ways (1) from the τ_s vs σ plot and (2) from the τ_s vs. μ plot. A detailed analysis on how to estimate the Larmor frequency from both these methods is given below:

4.2.3.1 From conductivity data

$$\sigma = ne\mu = \frac{ne^2\tau_p}{m^*} \tag{4.2.6}$$

$$\sigma\tau_s = \frac{ne^2\tau_p\tau_s}{m^*} = An \tag{4.2.7}$$

Now by fitting the $\sigma\tau_s$ vs. n plot with the above equation we get the values for A and the standard error (ΔA) for A. Here we take the standard error ΔA obtained from the fitting as the error or uncertainity in A.

The Larmor frequency Ω defined as $\frac{1}{\sqrt{\tau_s\tau_p}}$ when substituted into the above equation gives

$$\Omega = \frac{e}{\sqrt{m^* A}} \tag{4.2.8}$$

and the uncertainity in Ω is given by

$$\frac{\Delta\Omega}{\Omega} = \frac{\Delta A}{2A} \tag{4.2.9}$$

4.2.3.2 From Mobility data

$$\mu = \frac{e\tau_p}{m^*} \tag{4.2.10}$$

$$\mu\tau_s = \frac{e\tau_p\tau_s}{m^*} \tag{4.2.11}$$

$$A = \mu\tau_s = \frac{e}{m^*\Omega^2}; \quad \Omega \pm \Delta\Omega = \sqrt{\frac{e}{m^*A}} = \sqrt{\frac{e}{m^*A}}(1 \pm \frac{\Delta A}{2A}). \tag{4.2.12}$$

Both these methods give the Larmor frequency for our samples as $\Omega = 407 \pm 25$GHz.

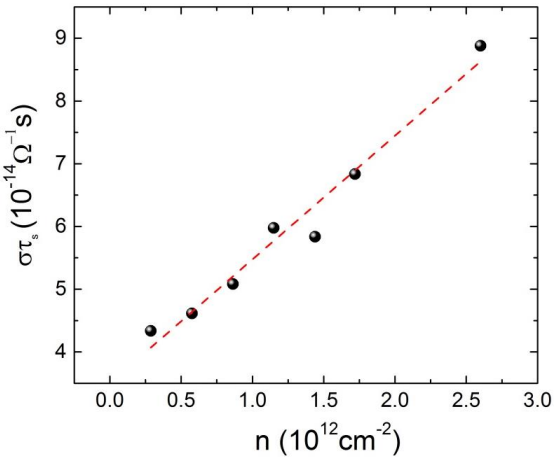

Figure 4.9: $\sigma\tau_s$ vs n for a bilayer graphene device. From the slope, the Larmor frequency for spins can be estimated.

Now in the case of DP mechanism the Larmor frequency with which the spins precess is related to the spin-orbit coupling constant through the equation

$$\Omega = \frac{2\Delta}{\hbar} \tag{4.2.13}$$

and gives a spin-orbit coupling strength in our bilayer samples to be $\Delta = 0.13$ meV. It should be noted that Δ depends weakly on the temperature. Therefore, it is unlikely that low energy phonons (such as acoustic phonons) are responsible for the observed spin scattering. Thus the most important question to be answered is whether the estimated spin-orbit coupling strength is intrinsic or extrinsic in nature. While theoretical calculations have shown the intrinsic spin-orbit coupling strength to be in

the range 25μeV - 0.1 meV in clean bilayer graphene samples, the influence of both the externally applied electric field and the role of the adatoms cannot be excluded [37,38]. Since inter-layer hopping is involved in bilayer graphene, electric field dependent modifications to the intrinsic spin-orbit coupling strength are expected. Adatoms on the other hand induce local curvature to an otherwise flat graphene lattice and can cause spin scattering by both EY and DP mechanisms [12, 36]. However, in the case of bilayer graphene the role of the adatoms in determining DP or EY spin scattering might be even smaller due to a higher lattice stiffness [39], thus reducing the adatom induced SO coupling strength. Thus, more detailed and thorough investigations are needed to clarify the type and concentration of spin scatterers in single and bilayer graphene and to differentiate the contribution from extrinsic and intrinsic factors to the spin-orbit coupling in bilayer graphene samples with disorder.

4.3 Conclusion

In conclusion, we have demonstrated spin injection and detection in bilayer graphene across MgO barriers and observed spin relaxation times up to 2 ns at room temperature. Our systematic study shows that at room temperature spin scattering in bilayer graphene follows an inverse dependence of τ_s on both the mobility μ and the room temperature minimum conductivity σ_{min}, indicating a DP spin scattering mechanism. We discuss the role of intrinsic and extrinsic factors that could lead to the dominance of DP spin scattering in bilayer graphene. While the inverse scaling of mobility with τ_s persists down to T = 5 K, the density dependence of τ_s indicates deviations from the DP mechanism at low temperatures near the charge neutrality point.

Bibliography

[1] N. Tombros, C. Jozsa, M. Popinciuc, H. T. Jonkman and B. J. van Wees, Nature **448**, 571 (2007).

[2] N. Tombros, S. Tanabe, A. Veligura, C. Jozsa, M. Popinciuc, H. T. Jonkman and B. J. van Wees, Phys. Rev. Lett. **101**, 046601 (2008).

[3] C. Jozsa, T. Masssen, M. Popinciuc, P. J. Zomer, A. Veligura, H. T. Jonkman and B. J. van Wees, Phys. Rev. B **80**, 241403(R) (2009).

[4] M. Popinciuc, C.Jozsa, P. J. Zomer, N. Tombros, A. Veligura, H. T. Jonkman and B. J. van Wees, Phys. Rev. B **80**,214427 (2009).

[5] C. Jozsa, M. Popinciuc, N. Tombros, H. T. Jonkman and B. J. van Wees, Phys. Rev. Lett. **100**, 236603 (2008).

[6] S. Cho, Y.-F. Chen and M. S. Fuhrer, Appl. Phys. Lett. **91**, 123105 (2007).

[7] W. Han, K. Pi, W. Bao, K. M. McCreary, Y. Li, W. H. Wang, C. N. Lau and R. K. Kawakami, Appl. Phys. Lett. **94**, 222109 (2009).

[8] W. Han, W. H. Wang, K. Pi, K. M. McCreary, W. Bao, Y. Li, F. Miao, C. N. Lau and R. K. Kawakami, Phys. Rev. Lett. **102**, 137205 (2009).

[9] K. Pi, W. Han, K. M. McCreary, A. G. Swartz, Y. Li, and R. K. Kawakami, Phys. Rev. Lett. **104**, 187201 (2010).

[10] W. Han, K. Pi, K. M. McCreary, Y. Li, J. I. Wong, A. G. Swartz and R. K. Kawakami, Phys. Rev. Lett. **105**, 167202 (2010).

[11] M. Shiraishi, M. Ohishi, R. Nouchi, N. Mitoma, T. Nozaki, T. Shinjo and Y. Suzuki, Adv. Funct. Mater. **19**,3711 (2009).

[12] A. H. Castro Neto and F. Guinea, Phys. Rev. Lett. **103**, 026804 (2009).

[13] D. Huertas-Hernando, F. Guinea and A. Brataas, Phys. Rev. Lett. **103**, 146801 (2009).

[14] K.S. Novoselov, A. K. Geim, S. V. Morozov, D. Jiang, Y. Zhang, S. V. Dubonos, I. V. Grigorieva, A. A. Firsov, Science **306**, 666 (2004).

[15] A. H. Castro Neto, F. Guinea, N. M. R. Peres, K. S. Novoselov and A. K. Geim, Rev. Mod. Phys. **81**, 109 (2009).

[16] S. Das Sarma, E. H. Hwang and E. Rossi, Phys. Rev. B **81**,161407(R) (2010).

[17] E. I. Rashba, Phys. Rev. B **62**, R16267 (2000).

[18] S. S. P. Parkin, C. Kaiser, A. Panchula, P. M. Rice, B. Hughes, M. Samant, S.-H. Yang, Nat. Mater. **3** , 862 (2004).

[19] S. V. Morozov, K. S. Novesolov, M. I. Katsnelson, F. Schedin, D. C. Elias, J. A. Jaszczak and A. K. Geim, Phys. Rev. Lett. **100**, 016602 (2008).

[20] S. Adam and S. Das Sarma, Phys. Rev. B **77**, 115436 (2008).

[21] Y.-.W. Tan, Y. Zhang, K. Bolotin, Y. Zhao, S. Adam, E. H. Hwang, S. Das Sarma, H. L. Stomer and P. Kim, Phys. Rev. Lett. **99**, 246803 (2007).

[22] M. Monteverde, C. Ojeda-Aristizabal, R. Weil, K. Bennaceur, M. Ferrier, S. Gueron, C. Glattli, H. Bouchiat, J. N. Fuchs and D. L. Maslov, Phys. Rev. Lett. **104**, 126801 (2011).

[23] F. J. Jedema, A. T. Filip and B. J. van Wees, Nature **410**, 345 (2001).

[24] F. J. Jedema, M. V. Costache, H. B. Heersche, J. J. A. Baselmans and B. J. van Wees, Appl. Phys. Lett. **81**,5162 (2002).

[25] N. Tombros, Ph.D Thesis, University of Groningen (2008).

[26] R. J. Elliott, Phys. Rev. **96**, 266 (1954).

[27] M. I. Dyakonov and V. I. Perel, Sov. Phys. Solid State **13**, 3023 (1972).

[28] R. I. Dzhioev, K. V. Kavokin, V. L. Korenev, M. V. Lazarev, N. K. Poletaev, B. P. Zakharchenya, E. A. Stinaff, D. Gammon, A. S. Bracker and M. E. Ware, Phys. Rev. Lett. **93**, 216402 (2004).

[29] S. Adam and M. D. Stiles, Phys. Rev. B **82**, 075423 (2010).

[30] T. Stauber, N. M. R. Peres and F. Guinea, Phys. Rev. B **76**, 205423 (2007).

[31] S. Xiao, J.-H. Chen, S. Adam, E. D. Williams and M. S. Fuhrer, Phys. Rev. B **82**, 041406(R) (2010).

[32] J. Nilsson, A. H. Castro Neto, F. Guinea and N. M. R. Peres, Phys. Rev. Lett. **97**, 266801 (2006).

[33] B. I. Shklovskii, Phys. Rev. B **73**, 193201 (2006).

[34] G. L. Bir, A. G. Aronov and G. E. Pikus, Zh. Eksp. Teor. Fiz. **69**, 1382 (1975); Sov. Phys. JETP **42**, 705 (1975).

[35] I. Zutic, J. Fabian and S. Das Sarma, Rev. Mod. Phys. **76**, 323 (2004).

[36] C. Ertler, S. Konschuh, M. Gmitra and J. Fabian, Phys. Rev. B **80**, 041405 (R) (2009).

[37] F. Guinea, New Journal of Physics **12**, 083063 (2010).

[38] S. Konschuh, M. Gnitra and J. Fabian, Phys. Rev. B **82**, 245412 (2010).

[39] J. C. Meyer, A. K. Geim, M.I. Katsnelson, K. S. Novoselov, D. Obergfell, S. Roth, C. Girit and A. Zettl, Solid State Commun. **143**, 101 (2007).

Chapter 5

Colossal Enhancement of Spin-Orbit Coupling in Weakly Hydrogenated Graphene[1]

5.1 Introduction

In the previous chapter, we discussed comprehensively the spin transport in bilayer graphene and compared the results to its single layer counterpart, employing the widely used non-local spin-valve geometry. This approach, however, required magnetic elements, i.e. applied parallel and perpendicular external magnetic fields and ferromagnetic electrodes, for both injection and detection of the diffusing spins in graphene. An alternate method to study the spin transport in a material is by invoking the spin Hall effect (SHE) [2, 14], thus avoiding magnetic elements in the device geometry. However, specific to graphene, the realization of the spin Hall effect requires an enhancement of its otherwise weak spin-orbit (SO) coupling. Such enhancement of the SO coupling strength is also essential for the realization of many interesting phenomena such as the topological insulator states [3–5] and the quantum spin Hall

[1] Jayakumar Balakrishnan et al., Nature Physics 9, 284 (2013)

effect [3]. In this chapter, we will discuss the adatom-induced enhancement of the SO coupling strength in graphene and it's effect on charge and spin transport. For this, weakly hydrogenated graphene has been used as the model system.

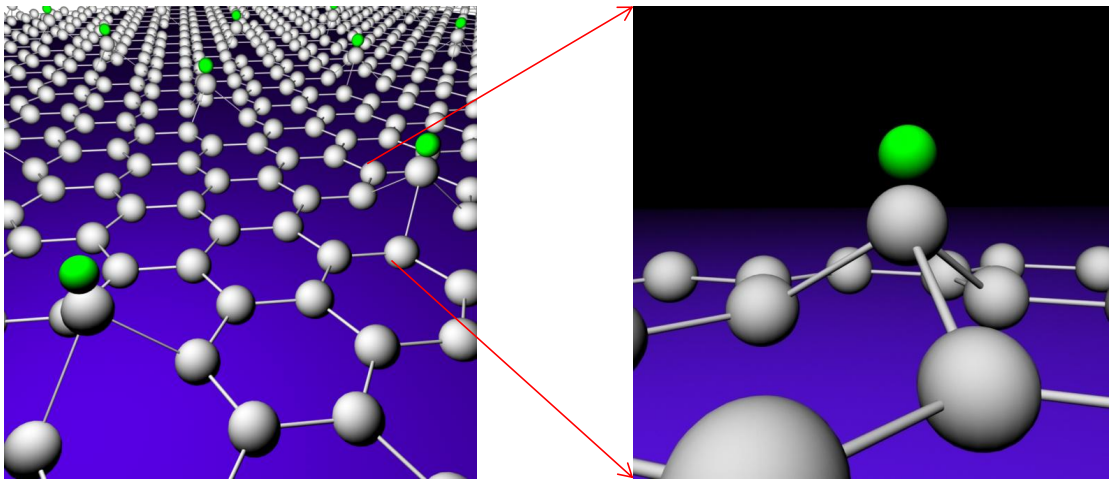

Figure 5.1: Schematics showing the lattice deformation due to the functionalization of graphene with adatoms like hydrogen.

5.2 Functionalization of Graphene

Graphene [6] is an ideal 2D system with large Young's modulus [7] and low bending rigidity [12]. Its extraordinary in-plane mechanical strength allows for large out-of-plane deformations, even at the atomic scale. This enables a broad class of chemical reactions/functionalizations which are not practical with other 2D materials [9]. For example, the functionalization of graphene with atoms such as hydrogen and fluorine enables the realization of graphene derivatives with novel physical and chemical properties [10, 11]. The out-of plane distortions of the planar carbon bonds, i.e. sp^2 to sp^3 hybridization accompanying the functionalization, are unique to graphene

and may allow for a strong enhancement in its otherwise weak intrinsic SO coupling strength [12–14]. This enhancement is unlike the enhancement in metals [41] and semiconductors [16], and is even distinct from the curvature-induced SO coupling in carbon nanotubes [17,18]. Since the sp^3 bond angle depends strongly on the graphene-substrate interaction the hydrogenation of graphene allows for a controllable SO strength ranging from a few tens of μeV up to 7 meV [12].

5.2.1 Hydrogenation of graphene

We introduce small amounts of covalently bonded hydrogen atoms to the graphene lattice by the e-beam dissociation of hydrogen silsesquioxane (HSQ) resist [19]. The HSQ is first spin-coated on graphene on a 300 nm SiO_2 substrate. For the experiments discussed in this chapter, we have used two different thickness of HSQ; 250 nm (fox 12) and 50 nm (DOW CRONING, Part No: XR-1541-002) and the parameters for spin-coating are

1. spin speed : 4000 rpm
2. acceleration : 110 rpm
3. duration: 100 sec.

An important point to be noted is that we do not bake our samples after HSQ spin-coating. Moreover, since HSQ is highly sensitive to humidity, it is also important not to expose/keep the resist in ambient conditions for long time.

The HSQ approach has a number of advantages over the hydrogenation of graphene using radio frequency (RF) hydrogen plasma [10,20]. First, it provides hydrogenation without introducing vacancies. Second, the degree of hydrogenation can be precisely controlled and kept minimal. Last but not least, it enables e-beam-controlled local

hydrogenation in the sub-micron size range.

5.3 Characterization of the hydrogenated graphene samples

5.3.1 Raman Characterization

As discussed, the basal plane hydrogenation of the graphene lattice is done by the e-beam dissociation of HSQ. In order to achieve varying concentration of hydrogen adatoms on graphene we expose the HSQ coated graphene devices to varying doses of e-beam dose in the range 200 μC/cm^2 to 8000 μC/cm^2. The e-beam-irradiated samples are then characterized by Raman spectroscopy measurements to estimate the percentage of hydrogenation. The evolution of the defect peak (D-peak)(see fig. 5.2 (a)) in the Raman spectrum is a clear indication for the progressive hydrogenation of graphene with increasing e-beam dose [19]. Moreover, an unambiguous conclusion on the hydrogenation of the graphene lattice can be reached (1) from the decrease in the Si-H peak intensity due to the dissociation of hydrogen from HSQ with e-beam dose and (2) from the change in the D-peak intensity with annealing in Ar environment [19]. Figure 5.2 (b) shows the evolution of the Si-H Raman peak at 2265 cm^{-1} as a function of the e-beam dose. With increasing dose the peak intensity decreases drastically indicating the dissociation of hydrogen from HSQ. This together with the increase in the D-peak intensity with e-beam dose points to the hydrogenation of the graphene lattice. Finally, the Raman spectrum showing the reversibility of hydrogenation upon annealing in Ar environment at 250°C for 2 hours is shown in fig. 5.2(c). A constant Ar gas flow of 0.3L/min is maintained throughout the annealing

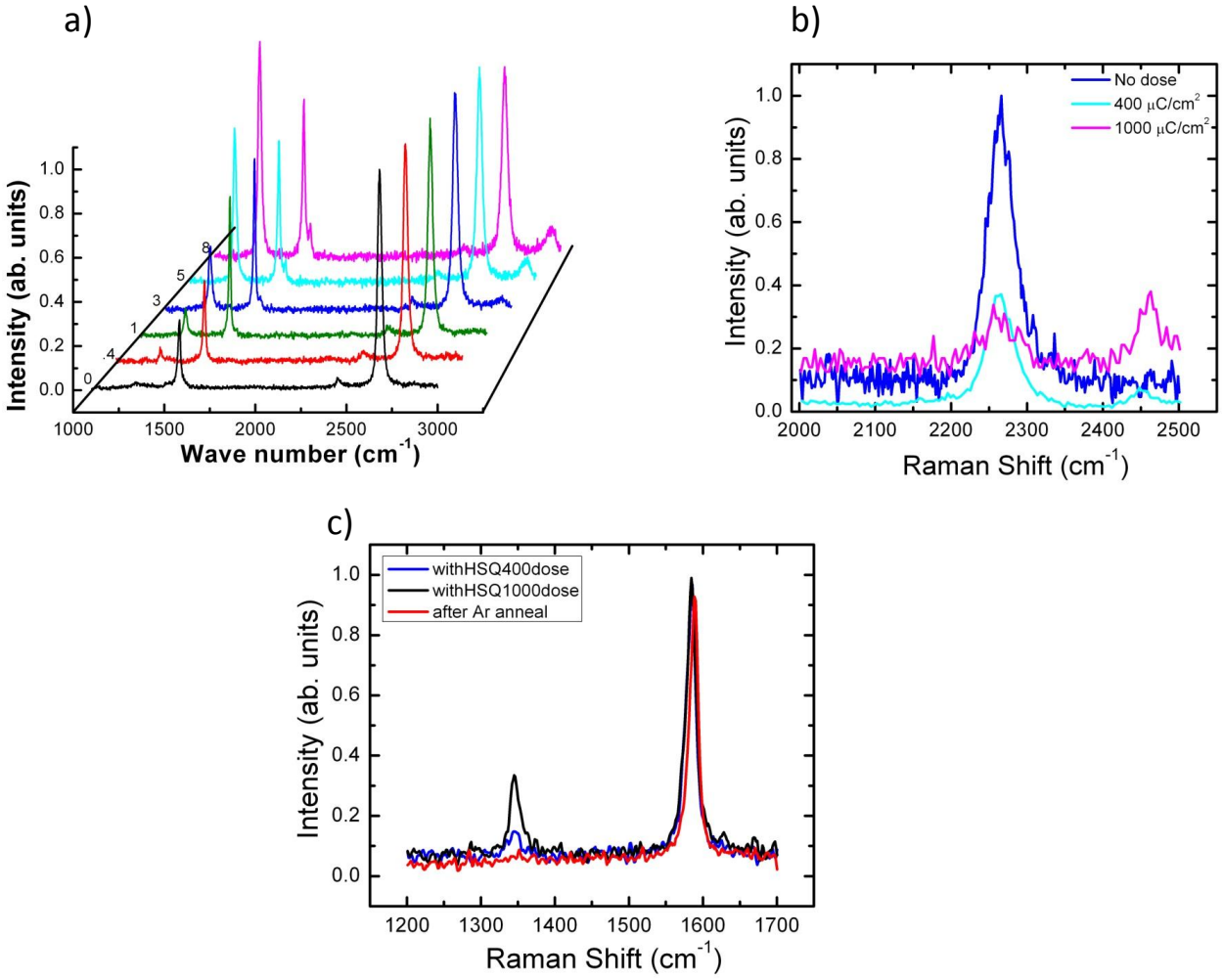

Figure 5.2: (a) The Raman spectrum of graphene coated with HSQ after irradiation with e-beam (dose 0-8 mC/cm^2). The progressive increase in the D-peak intensity results from the hydrogenation of the graphene sample. (b) The evolution of the Si-H peak at 2265 cm^{-1} as a function of e-beam dose. With increasing dose the peak intensity decreases drastically indicating the dissociation of the hydrogen from the HSQ. (c) The Raman spectrum for a single graphene device showing the reversibility of hydrogenation upon annealing in Ar environment at 250°C for 2 hours. A constant Ar gas flow of 0.3L/min is maintained throughout the annealing process. The near vanishing of the D-peak after annealing confirms that HSQ e-beam irradiation introduces minimum vacancies in the graphene system.

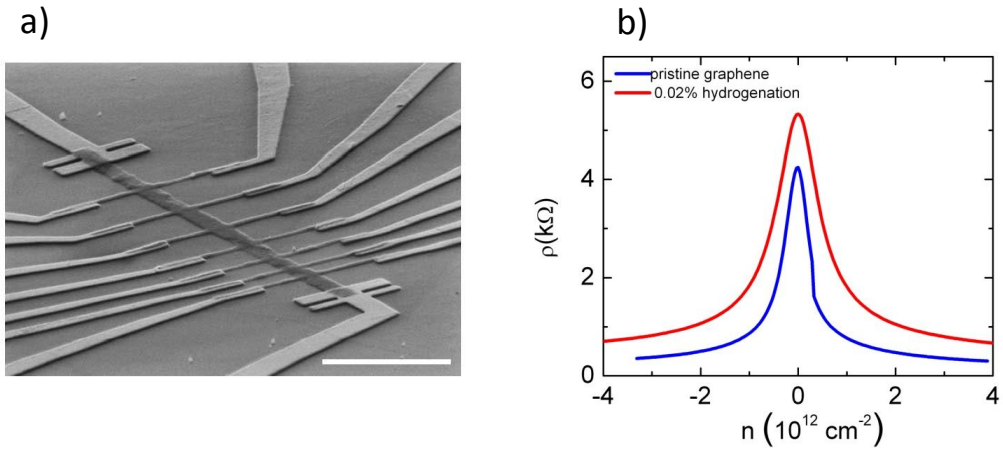

Figure 5.3: (a) Scanning electron micrograph of a hydrogenated graphene sample showing multiple Hall bar junctions. Scale bar, 5 μm (b) ρ vs. n for pristine and hydrogenated graphene.

process. The near vanishing of the D-peak after annealing confirms that HSQ e-beam irradiation introduces minimum vacancies in the graphene system.

5.3.2 Charge transport characterization

Most of the transport characterization involving functionalized graphene, hydrogenated and/or fluorinated, studied so far is in the highly insulating regime [10, 20]. However, for spin transport studies in a functionalized graphene system, the introduction of the adatoms should enhance the SO coupling strength while keeping the graphene system in the metallic regime with relatively long spin relaxation length. Hence, we focus our studies on graphene devices with low hydrogenation coverage. Moreover, hydrogen atoms are predicted to cluster at higher densities [21]. The charge transport measurements are characterized using standard Hall bar devices. The scanning electron microscope image of one such device with multiple Hall bar junctions is shown in fig. 5.3(a). Figure 5.3(b) shows the resistivity vs. carrier density

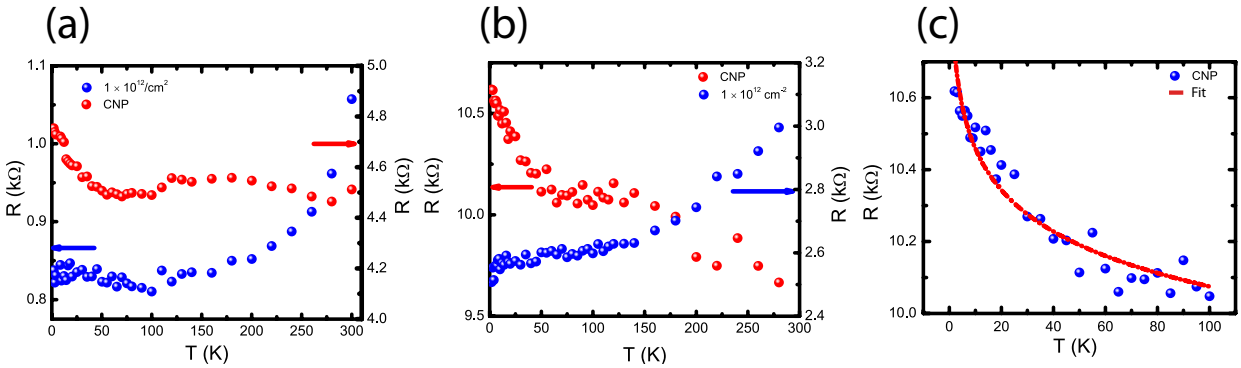

Figure 5.4: Resistance as a function of temperature at CNP (red solid circles) and at n =1 $\times 10^{12}/\mathrm{cm}^2$(blue solid circles) (a) for pristine graphene and (b) for weakly hydrogenated graphene. Note that the data presented in (a) and (b) are for two distinct samples. (c) low temperature R vs T for weakly hydrogenated graphene fitted for logarithmic corrections of the form $\rho = \rho_0 + \rho_1 \ln(\mathrm{T}_0/\mathrm{T})$; where $\rho_0 = 10251$ Ω, and $\rho_1 = 166$ Ω

plot for a graphene Hall bar device before and after hydrogenation at room temperature. When compared to previous hydrogenation studies [10, 20], the characteristic increase in the resistivity ρ and the broadening of the voltage plateau at the charge neutrality point are small. The mobility for these samples is calculated from the slope of the conductivity curve as $\mu = \frac{\partial \sigma}{\partial n}\frac{1}{e}$, and gives values of $\sim$ 1600 $\mathrm{cm}^2/\mathrm{Vs}$ for 0.02% hydrogenation.A detailed description on the determination of the percentage of hydrogenation is given in the next section. It is important to note that only junctions where the channel resistance (R vs. V_g) across all the four electrodes of the Hall bar show identical values are selected for any further measurements. In order to confirm that our samples are in the metallic regime, we compare the temperature dependence of the resistivity of a pristine graphene sample with that of a weakly hydrogenated graphene sample both at the charge neutrality point and at $n = 1\times 10^{12}/\mathrm{cm}^2$. At both doping levels the weakly hydrogenated graphene samples and pristine graphene samples show qualitatively similar temperature dependence (see

fig. 5.4(a&b)). A logarithmic increase in the resistivity at the CNP with decreasing temperature of the form $\rho = \rho_0 + \rho_1 \ln(T_0/T)$ (see fig.5.4(c)) is observed in both samples. Thus, in contrast to the strongly hydrogenated samples reported by Elias *et al.*, our samples are not in the strong localization regime, but are instead in the metallic regime (disordered Fermi liquid) [20, 22]. The logarithmic corrections to the resistivity likely originate from weak localization, disorder-induced electron-electron interaction (Altshuler-Aronov effect) [22], or the Kondo effect [23]. Further studies are needed to differentiate between the various contributions.

5.3.2.1 Is the transport in our devices in the diffusive regime or in the ballistic regime?

It is also important to confirm whether the charge transport in our devices is in the ballistic or in the diffusive regime. For this we calculate the electron mean free path for the weakly hydrogenated graphene sample with the largest mobility $\mu \sim$ 20,000 cm^2/Vs at 4 K and compare it with the dimensions of the device (W= 400 nm). The electron mean free path calculated from the equation $\sigma = 2\frac{e^2}{h} k_F l_e$ (where e is the electron charge, h is Planck's constant, k_F is the Fermi wave vector, and l_e is the electron mean free path) gives a l_e of 170 nm at $n = 5 \times 10^{11}/cm^2$. The calculated mean free path in our highest mobility sample is, thus, much less than the dimensions of our devices, and confirms that the transport in our weakly hydrogenated samples is in the diffusive regime.

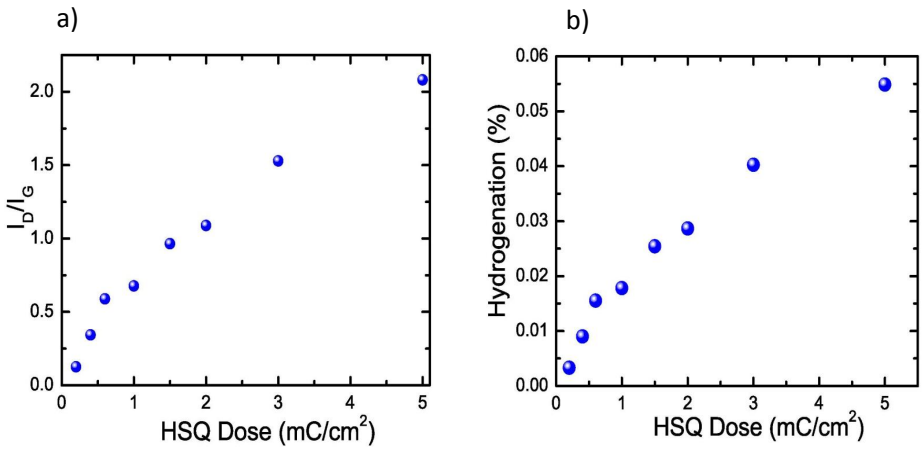

Figure 5.5: (a) The evolution of the integrated I_D/I_G ratio of graphene coated with HSQ samples irradiated with increasing e-beam dose (b) The evolution of the percentage of hydrogenation with increasing irradiation dose for HSQ (0- 5mC/cm^2) calculated from the I_D/I_G ratio

5.3.3 Determination of percentage of hydrogenation

5.3.3.1 Estimate from Raman Data

The concentration of impurities (n_i) and hence the percentage of hydrogenation can be estimated from the I_D/I_G ratio (see figure 5.3(a)) of the Raman peaks for different e-beam irradiation dose [24]. From the I_D/I_G ratio the spacing between the hydrogen atoms, and hence the impurity concentration can be determined using the relation [24] (see figure 5.5)

$$L_D^2(nm^2) = (1.8 \pm 0.5) \times 10^{-9} \lambda_L^4 (I_G/I_D) \tag{5.3.1}$$

$$n_i(cm^{-2}) = 10^{14}/(\pi L_D^2) \tag{5.3.2}$$

(where L_D = separation between hydrogen atoms, λ_L = wavelength of the Raman Laser = 514 nm, I_G = intensity of Raman G-peak, I_D = intensity of Raman D-peak).

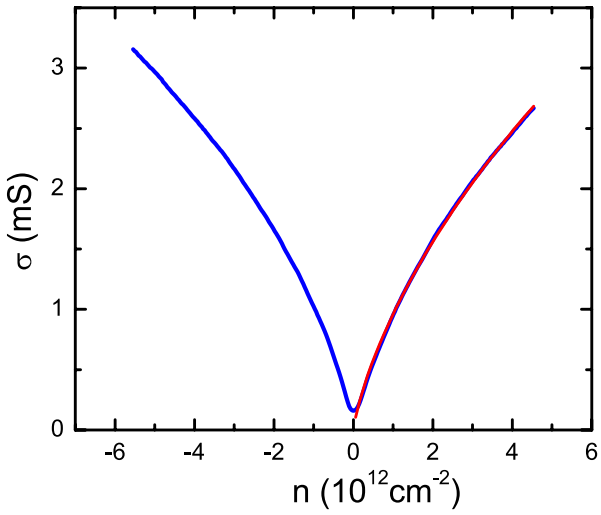

Figure 5.6: The σ vs n plot for one of the G/HSQ samples irradiated with an e-beam dose of 1mC/cm^2. The red curve is the fit to the conductivity for resonant scatterers which gives an impurity density $n_{imp} = 1 \times 10^{12}$/cm^2.

The I_D/I_G ratio for 1mC/cm^2 and 3mC/cm^2 HSQ dose gives L_D = 13 nm and 9 nm, and $n_i = 0.9 \times 10^{12}$/cm^2 and 1.6×10^{12}/cm^2 respectively. From the L_D values, an estimate of the fraction of hydrogenation is obtained as $\frac{3\sqrt{3}}{\pi}\left(\frac{a}{L_D}\right)^2 \times 100$. The calculated values of hydrogenation for 1mC/cm^2 and 3 mC/cm^2 HSQ dose are thus 0.018% and 0.05%, respectively.

5.3.3.2 Estimate from Transport data

An estimate of the impurity concentration (n_i) can also be done from the conductivity (σ) vs. carrier density (n) for the hydrogenated graphene samples. Figure 5.6 shows the σ vs. n data for the sample e-beam-irradiated with a HSQ dose of 1mC/cm^2. The conductivity due to resonant scatterers is given by the relation [25, 26]

$$\sigma = \left(\frac{4e^2}{h}\right)\left(\frac{k_F^2}{2\pi n_i}\right) ln^2(k_F R) \tag{5.3.3}$$

(where $k_F = (\pi n)^{1/2}$ is the Fermi wave vector, n_i is the concentration of impurity adatoms, and R is the impurity radius) and a fit to the experimental data with this equation gives $n_i \sim 1.2 \times 10^{12}/\text{cm}^2$ for 1mC/cm^2 and $2 \times 10^{12}/\text{cm}^2$ for 3 mC/cm^2 HSQ irradiation respectively. The adatom concentration increases by a factor of two from 1mC/cm^2 to 3 mC/cm^2 irradiation. The percentage of hydrogenation obtained as $\sim \left(\frac{n_i}{n_c}\right) \times 100$ gives 0.025% and 0.051% for 1mC/cm^2 and 3 mC/cm^2 HSQ irradiation respectively, where n_c is the density of carbon atoms in the hexagonal lattice. This estimate from the transport data is consistent with the above estimate from the Raman data.

5.4 Spin transport studies in weakly hydrogenated graphene devices

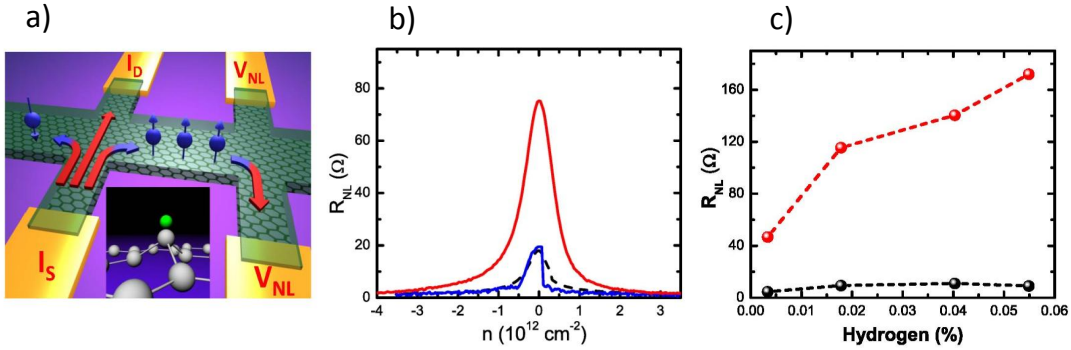

Figure 5.7: (a) Measurement schematics for the non-local spin Hall measurement. Inset: schematics showing the deformation of the graphene hexagonal lattice due to hydrogenation. (b) R_{NL} versus n for pristine graphene (blue) and hydrogenated graphene 0.02% (red) at room temperature. The dark grey dashed lines show the ohmic contribution to the measured signal for pristine graphene. (c) Dependence of the R_{NL} on the percentage of hydrogenation. The dark grey dashed lines show the calculated R_{Ohmic} contribution for this sample.

Once the charge transport and Raman characterizations are performed, samples with uniform hydrogenation are selected for spin transport measurements. Since, our aim is to study the spin Hall effect in the non-local geometry we employ the standard H-bar geometry for measuring the non-local spin Hall signal [27, 28]. Here, a charge current ($\sim 5\mu$A) is passed across the transverse contacts I_S and I_D and the non-local voltage (V_{NL}) is measured across the adjacent contacts (see figure 5.7(a)). Note that in the H-bar geometry neither the spin injection nor the spin detection requires ferromagnetic leads, since the former is achieved by the spin Hall effect (SHE), and the latter by the inverse spin Hall effect (iSHE). Figure 5.7 (b) shows the non-local resistance (R_{NL}) measurements for an exfoliated graphene Hall bar with length L = 2 μm and width W = 1 μm. The presence of a finite non-local signal at zero field is not intriguing since its value is comparable to the estimated Ohmic contribution

$$R_{Ohmic} = \rho e^{\frac{-\pi L}{W}} \tag{5.4.1}$$

This is expected for pristine graphene samples since the intrinsic SO coupling is so weak that any non-local signal due to spin Hall effect can be observed only at very low temperatures ($\sim$ 0.1 K) [3, 14]. However, after very weak hydrogenation ($\sim$ 0.02%), we observe a significant increase ($\sim$ 400%) in the non-local signal, well above what can be accounted for by Ohmic contribution. With increasing hydrogenation the measured R_{NL} shows a steep increase, reaching 170Ω at 0.05% hydrogenation (see figure 5.7 (c)). It should be noted that a strong increase in non-local signal is observed even at charge densities $\geq 1\times 10^{12}/\text{cm}^2$. Since the Ohmic contribution to the non-local signal remains negligible over the entire hydrogenation level, the only plausible explanation for the observed physical phenomenon, in the absence of an applied field and at room temperature, is the spin Hall effect. Here, the SO coupling induced external magnetic field exerts a spin-dependent force $F = 2\mu_B\vec{\nabla}(\vec{S}\cdot\vec{B})$ on the

charge carriers, leading to a pure spin current orthogonal to the charge current [29]. The diffusing spins in graphene, in turn, induce a transverse voltage via the iSHE, which is detected non-locally at the detector electrode.

5.4.0.3 Eliminating contributions from spurious thermoelectric effects to the measured non-local signal

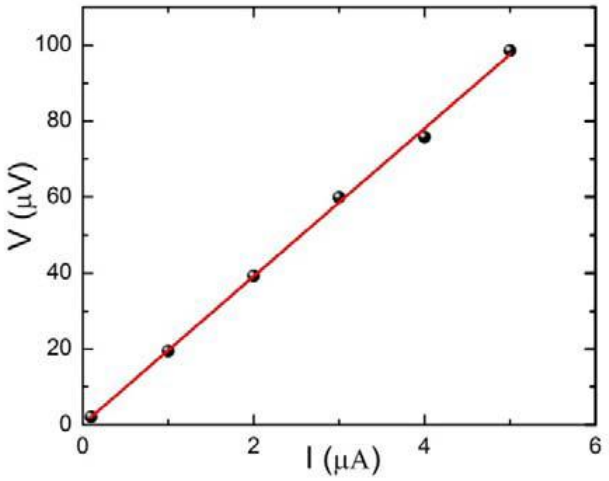

Figure 5.8: The I-V characteristics of the non-local signal. The linear dependence of the I-V curve clearly excludes the possibility of any dominant thermoelectric contribution to the non-local signal.

A possible source of the measured non-local signal, apart from the Ohmic contribution discussed above, is the contribution from thermoelectric effects, like contributions from Joule heating. To make sure that such thermoelectric effects are not responsible for the observed non-local signal, we studied the dependence of the non-local voltage as a function of the applied current. If the dominant contribution is from the thermoelectric effect the voltage should show a non-linear dependence with applied current. However, our data clearly shows a linear dependence, thus excluding any possible contribution from thermoelectric effect. Moreover, it should be noted that

the temperature gradient due to thermoelectric effect should be along the length of the sample, while the measured non-local voltage is across the width in the H-bar geometry, which also allows us to exclude any such contribution from thermoelectric effects on the measured non-local signal.

5.4.1 Carrier density dependence of the non-local signal

A comparison of the carrier density dependence of the non-local signal with that of the geometrical leakage contribution indicates a large enhancement of the non-local signal at the charge neutrality point. This is a consequence of the transport being bipolar at the charge neutrality point. The spin Hall resistivity ρ_{xy} is inversely proportional to the chare carrier density, n [30]. At the neutrality point due to disorder and two particle scattering smearing of the 1/n singularity of ρ_{xy} occurs, resulting in a steep linear dependence of ρ_{xy} in n [31]. This implies that the spin Hall coefficient, given by $\partial\rho_{xy}/\partial n$ has a larger value, giving rise to a giant SHE signal.

5.4.2 Spin precession measurements in an external in-plane magnetic field

The most direct way to confirm whether the observed non-local signal is due to the SHE is to study the in-plane magnetic field sweeps, where the presence of spin polarized current leads to an oscillating signal [27]. For the H-bar geometry, the non-local signal is predicted to oscillate in an in-plane magnetic field range given by the Larmor frequency ω_B=ΓB $\leq$(D_s/W^2), where Γ is the gyromagnetic ratio, B the applied magnetic field, D_s the spin diffusion coefficient and W is the width of the sample [27]. For this, devices with higher mobility$\mu \sim$ 20,000 cm^2/Vs (higher diffusion

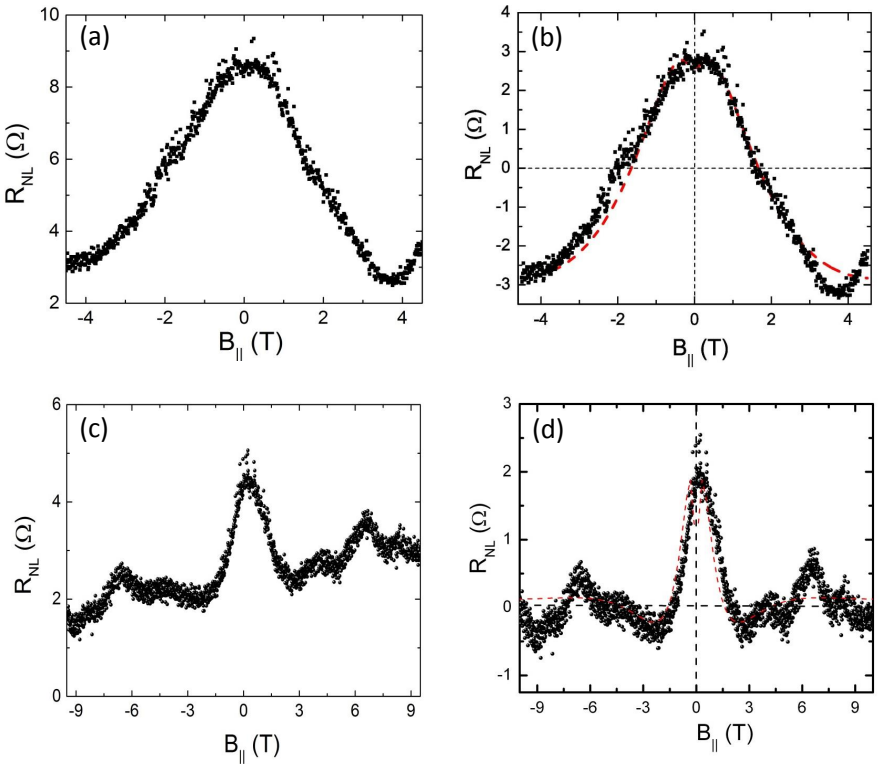

Figure 5.9: Parallel-field precession data for the sample with L/W $\sim$ 5 and mobility $\sim$ 20,000 cm^2 /Vs (a) raw data and (b) same data after a background has been subtracted from the raw data. The red dotted line is the fit for the experimental curves. The fitting gives $\lambda_s \sim 1.6$ μm. (c-d) for a second sample with $\lambda_s \sim 2.8$ μm

coefficient) and smaller W are selected so that the condition W $< \lambda_s$ is satisfied and the variation in the spin polarization across the strip is negligible. Figure 5.9(a) shows the in-plane field dependence of the non-local signal for the device with L/W $\sim$ 5 at T = 4 K. A fit to this oscillating signal using [27]

$$R_{NL} = \frac{1}{2}\gamma^2 \rho W Re\left[\frac{\sqrt{1+i\omega_B\tau_s}}{\lambda_s} e^{\left(-\frac{\sqrt{1+i\omega_B\tau_s}}{\lambda_s}\right)L}\right] \tag{5.4.2}$$

(where γ is the spin Hall coefficient, ρ is the graphene resistivity , W is the width of the sample, ω_B is the Larmor frequency, τ_s is the spin relaxation time and λ_s is the spin relaxation length) gives a spin relaxation length of $\lambda_s(B) \sim 1.6$ μm and

a spin Hall coefficient $\gamma \sim 0.18$. Figure 5.9(b) shows similar precession data for a second device with $\lambda_s \sim 2.08$ μm,$\tau_s \sim 40$ ps and $\gamma \sim 0.13$. It should be noted that such an oscillatory behaviour is not seen for pristine graphene samples. Thus, the oscillatory behaviour of R_{NL} is a direct signature of both the SHE arising from the hydrogenation of the pristine graphene lattice and the enhancement of an otherwise weak SO coupling strength in graphene upon hydrogenation.

5.4.2.1 Important note on precession measurements:

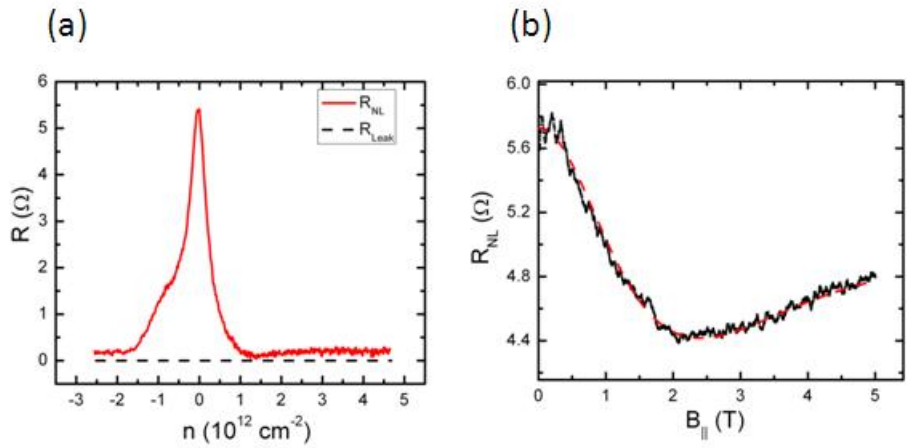

Figure 5.10: The non-local signal, R_{NL} vs. n. The black dashed lines show the calculated leakage current contribution and (b) the precession measurement for the same sample.

It is important to note that, the oscillating non-local signal in an in-plane field has an additional background signal (see figure 5.10). Such residual background signal can exist depending on the boundary conditions imposed on the spin current [32]. As shown by Hankiewicz et al. [32], the presence of additional leads perpendicular to the H-bar electrodes, does not influence the spin signal, but influences the residual background voltage. This appears to be the most plausible explanation for the offset in our data. The equation 5.4.2. used for fitting the data strictly explains the precession

part of the data and does not consider the offset involved.

5.4.2.2 Non-local signal as function of perpendicular magnetic field:

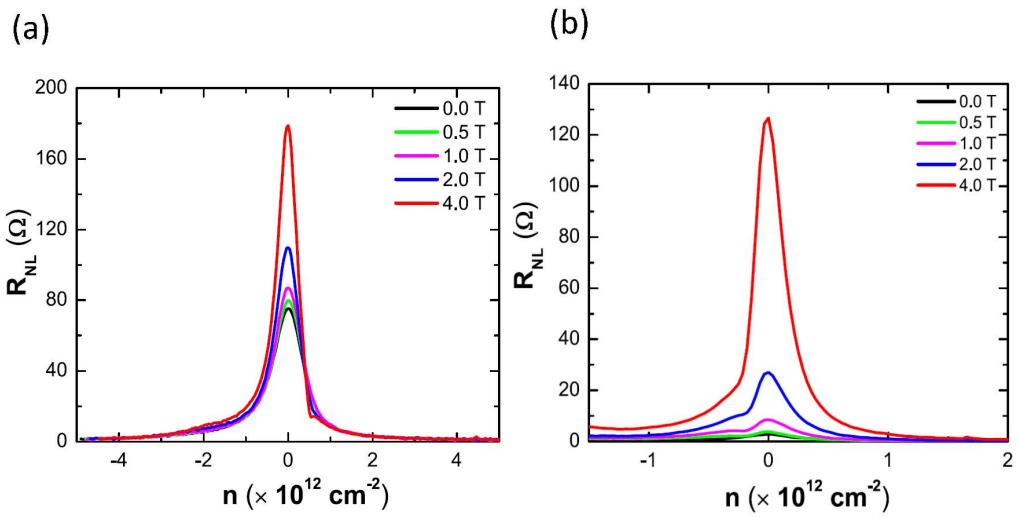

Figure 5.11: R_{NL} vs. n for different perpendicular magnetic fields in the range 0-4 T for (a) sample with L (2 μm)/W (1 μm) = 2 and (b) sample with L (2 μm)/W (0.4 μm) = 5

In addition to the in-plane magnetic field dependence, we also study the dependence of the non-local signal in a perpendicular magnetic field. Figure 5.11 represents the measured R_{NL} vs. n for perpendicular magnetic fields in the range 0-4T and shows an increasing R_{NL} with increasing B field. The large increase in the non-local signal near the charge neutrality point can be understood as the combined effect of the bipolar transport at charge neutrality point and the Zeeman splitting in an applied external magnetic field. Both result in a steep increase in the Hall resistivity at the CNP and hence to an enhancement of our non-local signal [31, 33]. Moreover, in the presence of an external field the percentage change in the non-local signal is comparable to the changes observed due to flavour Hall effect in pristine graphene

samples [33]. This, in addition to the recent results on the absence of ferromagnetic ordering in graphene due to point defects and in hydrogenated graphene, clearly supports the fact that magnetic ordering in our low hydrogenated graphene samples is, if at all, weak and can be neglected [34, 35]. In order to confirm that there are no ferromagnetic moments induced by hydrogenation in our experiments, we have performed anomalous Hall effect (AHE) measurements. Figure 5.12 shows the AHE measurements for one of our samples at 3.4 K. The absence of the AHE signal is a clear indication that there is no ferromagnetic ordering in our weakly hydrogenated samples also.

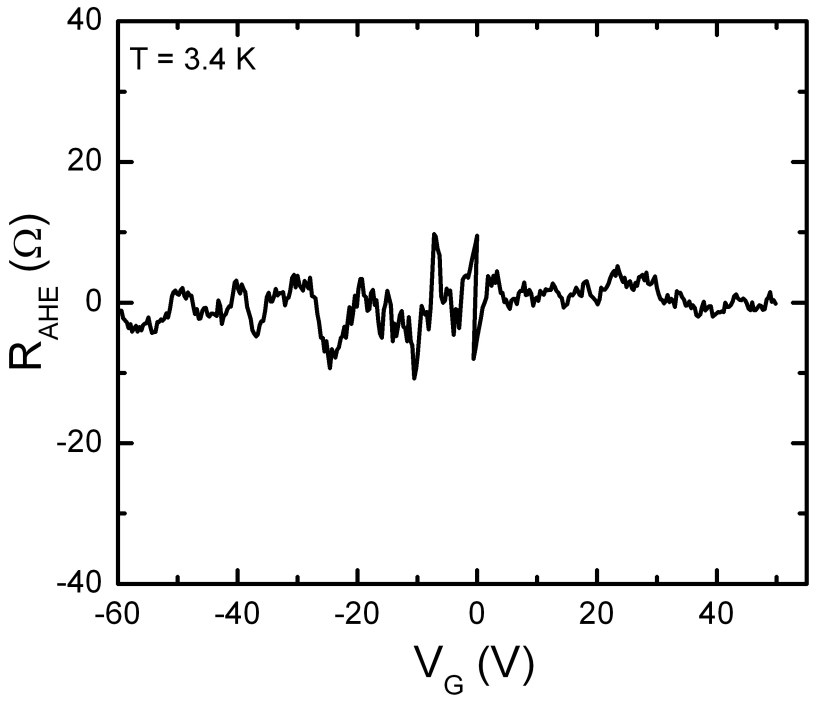

Figure 5.12: The absence of any anomalous Hall signal at zero magnetic field for the weakly hydrogenated sample at T = 3.4 K.

5.4.3 Length and width dependence of the Non-local signal

5.4.3.1 Length dependence

Further to the magnetic field dependence, we also study the length and width dependence of the non-local signal to confirm that the origin of the signal in weakly hydrogenated graphene samples is due to the SHE. We first discuss the length dependence by keeping the width W = 1 μm constant. Figure 5.13 shows the length dependence of the non-local signal both at the charge neutrality point and at $n = 1 \times 10^{12}/\text{cm}^2$, for the same sample hydrogenated first to 0.02% and then to 0.05%. The sample has mobilities of 1600 cm^2/Vs and 900 cm^2/Vs for 0.02% and 0.05% hydrogenation respectively. At zero applied field the equation (5.4.2) for the non-local signal for a device with length L and width W becomes [27, 28]

$$R_{NL} = \frac{1}{2}\gamma^2\rho\frac{W}{\lambda_s}e^{-\frac{L}{\lambda_s}} \tag{5.4.3}$$

By fitting the R_{NL}/ρ vs. L curve using the above equation (5.4.3), we determine the spin relaxation length $\lambda_s \sim (0.95\pm0.02)\mu$m and $\gamma \sim 0.58$ at CNP, and $\lambda_s \sim (1.12 \pm 0.06)\mu$m and $\gamma \sim 0.45$ at $n = 1 \times 10^{12}/\text{cm}^2$. These results are consistent and in good agreement with the results from conventional lateral spin-valve [25, 26, 28, 39] devices for hydrogenated graphene with ferromagnetic contacts [35, 46]

5.4.3.2 Width dependence

Next we study the width dependence of the non-local signal at a fixed length L = 2μm. For this specific sample, the mobility is $\sim$ 14,000 cm^2/Vs at room temperature. In such high mobility samples, the width dependence of the SHE signal shows a power law dependence (see fig 5.14 (a)). The Ohmic contribution on the other hand

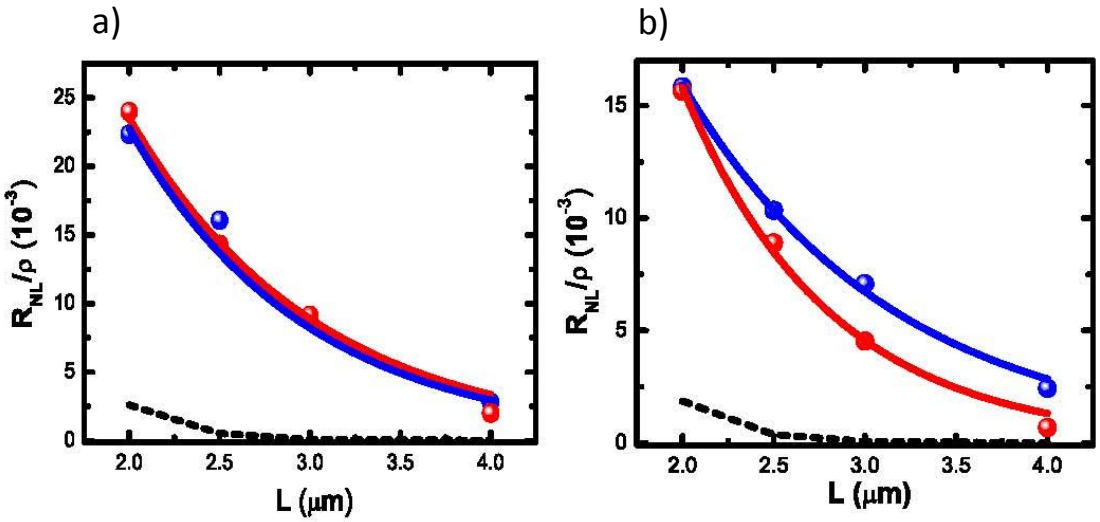

Figure 5.13: Length dependence of R_{NL} at room temperature. (a) At the CNP and (b) at n = 1×10^{12} cm^{-2} (b) for samples with 0.02%(red solid circles) and 0.05% (blue solid circles) hydrogenation. Here the length is the center-center distance between the injector and detector electrodes. The solid lines are the fit for the data and the dark grey dashed line is the calculated ohmic contribution at these charge carrier densities

depends on the width as $e^{\frac{-\pi L}{W}}$ and is orders of magnitude smaller. The distinction between the non-local signal and the expected Ohmic contribution is most apparent at the smallest width (W = 400 nm). This is in good agreement with the theoretical predictions of Abanin et al. [27] for narrow channels. The observed width dependence can be also explained by the theoretical model for clean wires, i.e. for high mobility devices in the limit W $< \lambda_{SO}$, where λ_{SO} is the spin precession length defined as the length scale in which the electron spin precess a full cycle in a clean ballistic 2D system [40, 41]. This length scale λ_{SO} remains unchanged as long as the width W of the wire is less than λ_{SO}. In such samples, the finite width of the devices can no longer be neglected and the spin relaxation length as a function of the width W is given by $\lambda_s(W) = \frac{\lambda_{SO}^2}{W}$. The relation for non-local signal can hence be modified as

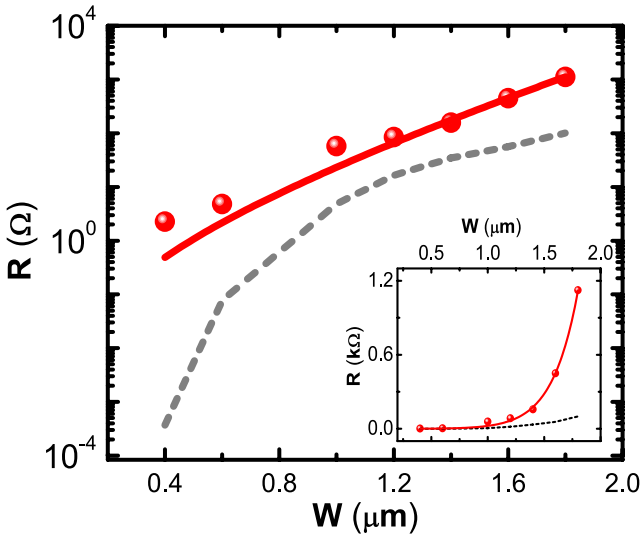

Figure 5.14: R_{NL} (red circles) as a function of width W (W= 400 nm -1.8 μm) for a fixed length L (2 μm). The solid red line is the fit for the data and the dark grey dashed line is the calculated ohmic contribution (inset: R versus W on a linear scale).

$$R_{NL} = \frac{1}{2}\gamma^2\rho\left(\frac{W}{\lambda_{SO}}\right)^2 e^{-\frac{LW}{\lambda_{SO}^2}} \tag{5.4.4}$$

For the case W << λ_{SO}, the expression can be Taylor expanded in W as

$$R_{NL} = \frac{1}{2}\gamma^2\rho\left(\frac{W}{\lambda_{SO}}\right)^2\left[1 - \frac{LW}{\lambda_{SO}^2} + ...\right] \tag{5.4.5}$$

i.e. for small W's the non-local signal has a power law dependence in W and a log-log plot of R vs. W should give a straight line as seen in Figure 5.14. The figure clearly follows the expected linear dependency and the fitting gives a self-consistent value for $\lambda_{SO} \sim 8\mu$m. It should also be noted that if the dominant signal came from Ohmic contribution, we should have seen a non-linear curve (grey dashed line in the figure).

5.5 Spin - orbit coupling in weakly hydrogenated graphene devices

The in-plane magnetic field spin precession measurements and the length and width dependence of the non-local signal unambiguously demonstrates that the observed signal is due to the spin Hall effect induced by the enhancement of the spin-orbit (SO) coupling strength in graphene by weak hydrogenation. In hydrogenated graphene, the dominant spin scattering mechanism is predicted to be the spin dephasing due to Elliott-Yafet (EY) scattering [12]. Within the EY mechanism the spin relaxation time τ_s is given by [43, 45]

$$\tau_s = \left(\epsilon_F/\Delta_{SO}\right)^2 \tau_p \tag{5.5.1}$$

where ϵ_F is the Fermi energy, Δ_{SO} is the spin-orbit coupling strength and τ_p the momentum relaxation time.

5.5.1 Estimation of τ_p and τ_s

As discussed in section 5.3.2, our weakly hydrogenated samples are in the diffusive regime. In this regime, the values for $\tau_p = 2\mathrm{D}/v_F^2$, $\tau_s = \lambda_s^2/\mathrm{D}$, where v_F is the Fermi velocity, D is the diffusion coefficient calculated from the conductivity σ as $\sigma = \nu e^2 \mathrm{D}$, where ν is the density of states and λ_s the spin diffusion length can be evaluated. For the typical hydrogenated samples with mobility 1600 $\mathrm{cm}^2/\mathrm{Vs}$ and 900 $\mathrm{cm}^2/\mathrm{Vs}$, the values for τ_p are 24 fs and 12 fs while the values for τ_s are 100 ps and 90 ps respectively at $n = 1.0 \times 10^{12}/\mathrm{cm}^2$. The Fermi energy, $\epsilon_F = \hbar \mathrm{v}_F \sqrt{\pi n}$ at $n = 1.0 \times 10^{12}/\mathrm{cm}^2$. Figure 5.15 shows the linear dependence of τ_s on τ_p for weakly hydrogenated samples

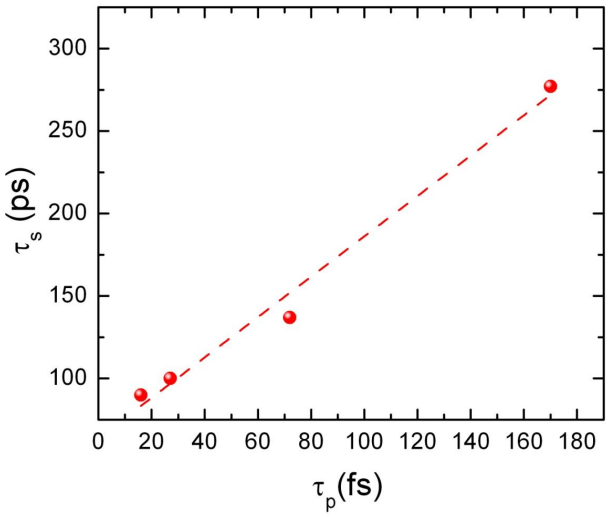

Figure 5.15: τ_s vs. τ_p for weakly hydrogenated graphene devices.

at a constant density $1.5 \times 10^{12}/\text{cm}^2$. The linear dependence clearly suggests that in weakly hydrogenated graphene the EY spin dephasing mechanism dominates.

5.5.2 Determination of SO coupling strength

From the calculated value of the τ_s, τ_p and ϵ_F, the spin-orbit coupling strength estimated using equation(5.5.1) gives a value of 2.5 $\pm$ 0.2 meV. Remarkably, this is three orders of magnitude higher than the values predicted for pristine graphene. In an undistorted graphene lattice all the bonds are sp^2 with the σ orbitals perpendicular to the π orbitals which are normal to the graphene plane. The σ orbitals are all coupled and the low energy physics of the problem is described by the 2D Dirac Hamiltonian for the π band:

$$H_0 = -i\hbar v_F \vec{\sigma} \cdot \vec{\nabla}, \tag{5.5.2}$$

where $\vec{\sigma}$ is the Pauli matrices that act on the subspace of the sublattice A and B, v_F is the Fermi-Dirac velocity ($\sim 10^6$ m/s), and $\vec{\nabla}$ is the gradient operator. The spectrum of H_0 is given by $E_0(k) = \pm v_F k$, and gives rise to two Dirac cones at the K and K' points in the Brillouin zone. The SO coupling given by :

$$H_{SO} = \Delta_{SO}^{at} \vec{L} \cdot \vec{S}, \tag{5.5.3}$$

where $\Delta_{SO}^{at} \approx 10$ meV is the SO strength for atomic carbon, $\vec{L}$ is the angular momentum operator (L = 1 for the carbon p-orbitals, with projections m=0, ± 1) and $\vec{S}$ (S= 1/2 with projections $s_z = \uparrow, \downarrow$) is the spin operator. The $\vec{L} \cdot \vec{S}$ operator induces transitions between orbitals of different values of m and s_z. Since the σ band is made of pure m = ± 1 states, and the π band is made out of pure m= 0 (*i.e.* p_z orbitals), the SO coupling always involves transition between the two bands. In a sp^2 bond, the σ and π bands are orthogonal and separated by an energy of the order of $\Delta_E \cong 10$ eV. Hence SO can occur only as a second order process with energy $\Delta_{SO}^{sp^2} = |\Delta_{SO}^{at}|^2/\Delta_E \cong$ 10 μeV, explaining the smallness of SO in flat graphene [44].

On the other hand, an adatom locally *breaks the reflection symmetry* across the graphene plane leading to an out-of-plane distortion by an angle φ relative to the plane (it varies from $\varphi = 0^\circ$ for sp^2 to $\varphi = 19.5^\circ$ for a full sp^3). For $\varphi \neq 0^\circ$ the distortion mixes the σ and π orbitals that are no longer orthogonal (for full sp^3 these states are degenerate). Hence, the SO becomes a first order effect leading to the large enhancement of SO coupling for covalently bonded hydrogen impurities in graphene. Following Ref. [12], we can show that the strength of the SO coupling can be written as:

$$r_{SO} = \Delta_{SO}^{H}/\Delta_{SO}^{at} \cong -3tan(\varphi)[1 - 2tan^2(\varphi)]^{1/2} \tag{5.5.4}$$

or equivalently,

$$\varphi = Arctan[1/4 - (9 - 8r_{SO}^2)^{1/2}/12]^{1/2}. \quad (5.5.5)$$

Our experimental results give $r_{SO} \cong 0.25$ which implies $\varphi = 5°$. This value is of the same order of magnitude to the value predicted theoretically, $\varphi_{DFT} \approx 16°$, by *ab initio* calculations for suspended graphene [45]. We assign the difference between the measured value and the one obtained by DFT to the interaction between graphene and its substrate, which is not taken into account in *ab initio* methods.

In the presence of this local spin orbit coupling two new terms can be added to the Hamiltonian H_0: (1) a Dresselhaus term,

$$H_D = \lambda_D \sigma_z s_z \tau_z \delta(r) a^2, \quad (5.5.6)$$

where $\tau_z = \pm 1$ represents either the K or K' points (a is the lattice spacing); and (2) a Rashba term,

$$H_R = 2\lambda_R(\sigma_x s_y \tau_z - \sigma_y s_x)\delta(r) a^2. \quad (5.5.7)$$

Notice that H_D is invariant under time reversal symmetry, T (T: $\sigma \rightarrow \sigma$, T: s $\rightarrow$ -s, T: $\tau \rightarrow$ -τ) and parity, P (P: $\sigma \rightarrow$ -σ, P: s $\rightarrow$ s, P: $\tau \rightarrow$ -τ). For a uniform system, it opens a gap in the spectrum of size λ_D . H_R is allowed in this case because reflection symmetry is broken. In a uniform system, this term does not open a gap but it splits the up and down spin bands into four hyperbolic bands of energy:

$$E_R(K) = \pm\lambda_R \pm [\lambda_R^2 + (v_F k)^2]^{1/2} \quad (5.5.8)$$

which are parabolic at low energies with an effective mass given by $m^* = \lambda_R / v_F^2$. These two terms are allowed by symmetry and, in a scattering process, lead to spin precession and hence to spin Hall effect.

5.5.3 Comparison with lateral spin valve data for hydrogenated Graphene

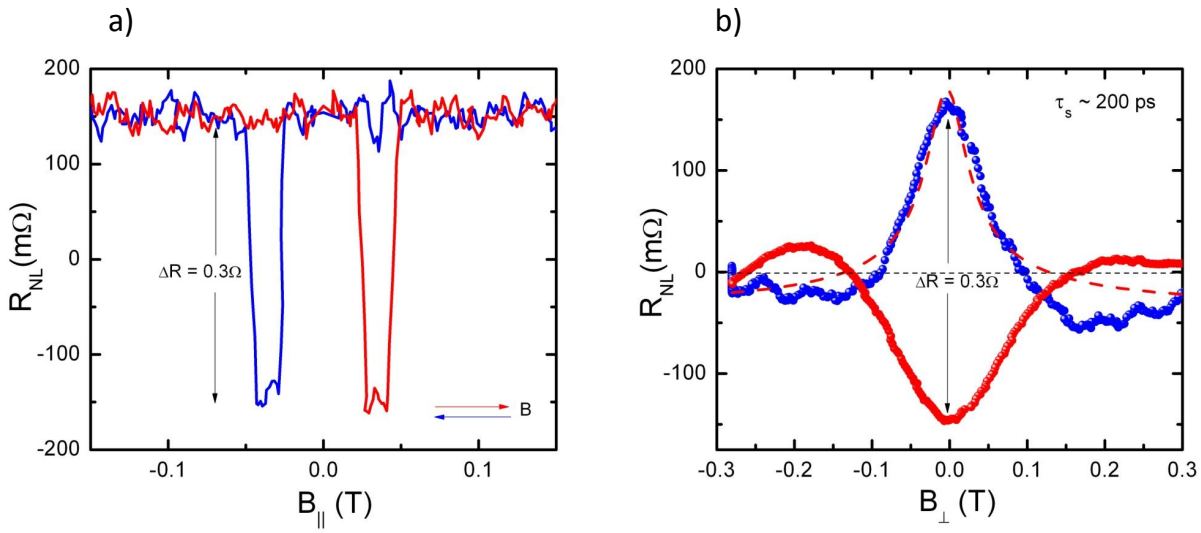

Figure 5.16: (a) The non-local spin-valve resistance as a function of the in-plane magnetic field.The horizontal arrows show the field sweep direction and (b) the Hanle precession measurement for perpendicular magnetic field for the same junction. The fitting gives a spin relaxation time of 200 ps which is in good agreement with the values extracted from the spin Hall measurements.

The spin relaxation times measured from our spin Hall measurements are in the picoseconds range. Since these spin Hall measurements in weakly hydrogenated graphene devices are performed for the first time in this work, it will be better to perform a consistency check on the extracted spin parameters using the conventional lateral spin-valve devices. For this, conventional spin-valve devices with MgO tunnel barrier and Co electrodes are made, followed by the HSQ coating. Here, while device fabrication, we do not develop the HSQ in TMAH (trimethyl ammonium hydroxide) solutions since the ferromagnetic electrodes easily degrade. Figure 5.16(a) shows the non-local bipolar spin-valve signal in an in-plane magnetic field sweeps in the range

± 150 mT. The clear bi-polar signal confirms the spin-transport in weakly hydrogenated graphene. Moreover, from the Hanle spin-precession measurements we can estimate the spin relaxation time in these samples. Figure 5.16(b) shows the Hanle spin precession measurements in an out-of plane magnetic field swept in the range ± 300mT. The fit to the Hanle curves, as explained in chapter 4, gives a spin relaxation time in the order of 200ps which is in excellent agreement with the values extracted independently from the spin Hall measurements. Moreover, these results are also in good agreement with the values reported by McCreary *et al.* [35] and by Wojtaszek *et al.* [46] in weakly hydrogenated graphene spin-valve devices.

5.5.4 Identification of the spin scattering mechanism

Finally, we identify the dominant microscopic mechanism for the observed spin Hall scattering. For the side jump mechanism the spin Hall resistivity ρ_{SHE} is independent of the impurity concentration n_{imp}, while for skew scattering $\rho_{SHE} \propto n_{imp}$ [30]. The ρ_{SHE} is estimated from the spin Hall angle, defined as $\gamma = (\sigma_{SHE}/\sigma_G) = (\rho_G/\rho_{SHE})$ and gives a value of $\rho_{SHE} = 12.9$ kΩ and 14.2 kΩ for 0.02% and 0,05% hydrogenation respectively. The value of ρ_{SHE}, thus, depends only weakly on n_{imp} ($n_{imp} \sim 0.9 \times 10^{12}/\text{cm}^2$ for 0.02% and $1.16 \times 10^{12}/\text{cm}^2$ for 0.05% hydrogenation) and hence, suggests the dominance of side-jump mechanism in hydrogenated graphene samples.

5.6 Conclusion

In this chapter, we have demonstrated that the spin-orbit coupling in graphene can be drastically enhanced by the controlled addition of covalently bonded adatoms without a significant suppression of conductivity. Hydrogenated graphene has been

used as a model system to demonstrate that this leads to a strong spin Hall effect. Such weak hydrogenation keeps the system in the metallic regime, without creating electronic (Anderson localization). The SHE is confirmed by directly measuring the non-monotonic oscillatory behaviour of the non-local signal in an applied in-plane magnetic field as also by studying the dependence of the non-local signal on the length, width and adatom density. From the length dependence of the non-local signal, we extract the spin transport parameters like the spin relaxation length $\sim$ 1μm, spin relaxation time $\sim$ 90 ps and spin-orbit coupling strength $\sim$ 2.5 meV for samples with 0.05% hydrogenation. These findings are crucial to the development of graphene based spintronics applications, as the need for ferromagnetic electrodes and magnetic field is eliminated from the device architecture. Last but not least, the demonstration of the non-local spin Hall effect due to impurity adatoms in graphene is a major step in the realization of a robust 2D topological states and a SHE based spin transistors (SHE-SFET) at RT.

Bibliography

[1] M. I. Dyakonov and V. I. Perel,Phys. Lett. A **35**, 459 (1971).

[2] J. E. Hirsch, Phys. REv. Lett. **83**, 1834 (1999).

[3] C. L. Kane and E. J. Mele, Phys. Rev. Lett. **95**, 226801 (2005).

[4] C. L. Kane and E. J. Mele, Phys. Rev. Lett. **95**, 146802 (2005).

[5] W. Conan, H. Jun, A. Jason, F. Marcel and W. Ruqian,Phys. Rev. X **1**, 021001 (2011).

[6] K. S. Novoselov, A. K. Geim, S. V. Morozov, D. Jiang, Y. Zhang, S. V. Dubonos, I. V. Grigorieva and A. A. Firsov, Science **306**, 666 (2004).

[7] C. Lee, X. D. Wei, J.W. Kysar, and J. Hone, Science **321**, 385 (2008).

[8] E. A. Kim and A. H. CastroNeto, Europhys. Lett. **84**, 57007 (2008).

[9] K. P. Loh, Q. L. Bao, P. K. Ang and J. X. Yang, J. Mater. Chem. **20**, 2277 (2010).

[10] D. C. Elias, R. R. Nair, T. M. G. Mohiuddin, S. V. Morozov, P. Blake, M. P. Halsall, A. C. Ferrari, D. W. Boukhvalov, M. I. Katsnelson, A. K. Geim and K. S. Novoselov, Science **323**, 610 (2009).

[11] R. R. Nair, W. Ren, R. Jalil, I.Riaz, V. G. Kravets, L. Britnell, P. Blake, F. Schedin, A. S. Mayorov, S. Yuan, M. I. Katsnelson, H.-M. Cheng, W. Strupinski, L. G. Bulusheva, A. V. Okotrub, I. V. Grigorieva, A. N. Grigorenko, K. S. Novoselov and A. K. Geim, Small **6**, 2877 (2010).

[12] A. H. Castro Neto and F. Guinea, Phys. Rev. Lett. **103**, 026804 (2009).

[13] M. J. Schmidt and D. Loss, Phys. Rev. B **81**, 165439 (2010).

[14] J. Zhou, Q. F. Liang and J. M. Dong, Carbon **48**, 1405 (2010).

[15] A. Fert and P. M. Levy, Phys. Rev. Lett. **106**, 157208 (2011).

[16] J. Wunderlich, B. Kaestner, J. Sinova and T. Jungwirth, Phys. Rev. Lett. **94**, 047204 (2005).

[17] F. Kuemmeth, S. Ilani, D. C. Ralph and P. L. McEuen, Nature **452**, 448 (2008).

[18] T. S. Jespersen, K. Grove-Rasmussen, J. Paaske, K. Muraki, T. Fujisawa, J. Nygard and K. Flensberg, Nat. Phys. **7**, 348 (2011).

[19] S. Ryu, M. Y. Han, J. Maultzsch, T. F. Heinz, P. Kim, M. L. Steigerwald and L. E. Brus, Nano Lett. **8**, 4597 (2008).

[20] M. Jaiswal, C. H. Y. X. Lim, Q. Bao, C. Y. Toh, K. P. Loh and B. Ozyilmaz , ACS Nano. **5**, 888 (2011).

[21] L. Hornekaer, E. Rauls, W. Xu, Z. Sljivancanin, R. Otero, I. Stensgaard, E. Laegsgaard, B. Hammer and F. Besenbacher, Phys. Rev. Lett. **97**, 186102 (2006).

[22] S. Lara-Avila, A. Tzalenchuk, S. Kubatkin, R. Yakimova, T. J. B. M. Janssen, K. Cedergren, T. Bergsten and V. Fal'ko, Phys. Rev. Lett. **107**, 166602 (2011).

[23] J.-H. Chen, L. Li, W. G. Cullen, E. D. Williams and M. S. Fuhrer, Nat. Phys. **7**, 535 (2011).

[24] L. G. Concado, A. Jorio, E. H. Martins Ferreria, F. Stavale, C. A. Achete, R. B. Capaz, M. V. O. Moutinho, A. Lombardo, T. S. Kulmala and A. C. Ferrari, Nano Lett. **11**, 3190 (2011).

[25] Z. H. Ni, L. A. Ponomarenko, R. R. Nair, R. Yang, S. Anissimova, I. V. Grigorieva, F. Schedin, P. Blake, Z. X. Shen, E. H. Hill, K. S. Novoselov and A. K. Geim, Nano Lett. **10**, 3868 (2010).

[26] S. Jo, D. K. Ki, D. Jeong, H. J. Lee and S. Kettemann, Phys. Rev. B **84**, 075453 (2011).

[27] D. A. Abanin, A. V. Shytov, L. S. Levitov and B. I. Halperin, Phys. Rev. B **79**, 035304 (2009).

[28] G. Mihajlovic, J. E. Pearson, M. A. Garcia, S. D. Bader and A. Hoffmann, Phys. Rev. Lett. **103**, 166601 (2009).

[29] M. I. Dyakonov and A. V. Khaetskii, Springer Series in Solid-State Sciences 157, (2008).

[30] S. Maekawa, Ed., Concepts in Spin Electronics, Ch 8, p363-367 (Oxford University Press, 2006).

[31] D. A. Abanin, R. V. Gorbachev, K. S. Novoselov, A. K. Geim, L. S. Levitov, Phys. Rev. Lett. **107**, 096601 (2011).

[32] E. M. Hankiewicz, L. W. Molenkamp, T. Jungwirth and J. Sinova, Phys. Rev. B **70**, 241301 (2004).

[33] D. A. Abanin, S. V. Morozov, L. A. Ponomarenko, R. V. Gorbachev, A. S. Mayorov, M. I. Katsnelson, K. Watanabe, T. Taniguchi, K. S. Novoselov, L. S. Levitov and A. K. Geim, Science **332**, 328 (2011).

[34] R. R. Nair, M. Sepioni, I-Ling Tsai, O. Lehtinen, J. Keinonen, A. V. Krasheninnikov, T. Thomson, A. K. Geim and I. V. Grigorieva, Nat. Phys. **8**, 199 (2012).

[35] K. M. McCreary, A. G. Swartz, W. Han, J. Fabian and R. Kawakami, Phys. Rev. Lett. **109**, 186604 (2012).

[36] N. Tombros, C. Jozsa, M. Popinciuc, H. T. Jonkman, B. J. van Wees, Nature **448**, 571 (2007).

[37] T.-Y. Yang, J. Balakrishnan, F. Volmer, A. Avsar, M. Jaiswal, J. Samm, S. R. Ali, A. Pachoud, M. Zeng, M.Poinciuc, G. Guntherodt, B. Beschoten and B. Ozyilmaz, Phys. Rev. Lett. **107**, 047206 (2011).

[38] A. Avsar, T.-Y. Yang, S. Bae, J. Balakrishnan, F. Volmer, M. Jaiswal, Z. Yi, S. R. Ali, G, Guentherodt, B.-H. Hong, B. Beschoten and B. Ozyilmaz, Nano Lett. **11**, 2363 (2011).

[39] A. Patra , S. Singh, B. Barin, Y. Lee, J. H. Ahn, E. del Barco, E. R. Mucciolo and B. Ozyilmaz, Appl. Phys. Lett. **101**, 162407 (2012).

[40] S. Kettamann, Phys. Rev. Lett. **98**, 176808 (2007).

[41] W. Paul and K. Stefan *in Handbook of Nanophysics: Nanotubes and Nanowires* Ch 28, (CRC Press) (2010).

[42] D. Huertas-Hernando, M. Gmitra, F. Guinea and A. Brataas, Phys.Rev.Lett. **103**, 146801 (2009).

[43] H. Ochoa, A. H. Castro Neto and F. Guinea, Phys. Rev. Lett. **108**, 206808 (2012).

[44] S. Konschuh, M. Gmitra and J. Fabian, Phys. Rev. B **82**, 245412 (2010).

[45] E. J. Duplock, M. Scheffler and P. J. D. Lindan, Phys. Rev. Lett. 92, 225502 (2004).

[46] M. Wojtaszek, I. J. Vera-Marun, T. Maassen and B. J. van Wees, Phys. Rev. B **87**, 081402 (2013).

Chapter 6

Giant Spin Hall Effect in CVD Graphene[1]

6.1 Introduction

The integration/utilization of graphene into commercial spintronics devices and topological quantum computation schemes requires a control over graphene's intrinsic properties like the spin-orbit coupling (SOC) strength, while preserving its long spin relaxation length [1, 2]. Here, the introduction of dilute adatoms is expected to hold significant potential as adatoms can enhance the SO interaction by several orders of magnitude. Covalently bonded hydrogen atoms have already been shown to enhance graphene's SOC strength [3]. Recently, it has been predicted that electron tunneling from graphene to heavy adatoms and back locally enhance graphene's SOC by several orders of magnitude [2, 4–6]. Decoration with adatoms, preserving time reversal symmetry and primarily inducing intrinsic SOC type, are the key factors to achieve a robust 2D topological insulator (TI) state in graphene [2]. The realization of such a quantum spin Hall state in conjunction with the electric field effect in graphene

[1] Jayakumar Balakrishnan et al., manuscript in preparation

is of great significance since TIs in proximity with superconductors are predicted to host Majorana fermions which can be used as building blocks for a topological quantum computer [2]. Most importantly, the detection of the spin-polarized current on the surface of the topological insulator is extremely difficult and requires the experiment to be performed in the ballistic transport regime [7, 8]. This is because due to the helical spin polarization of the surface states the spin relaxation length and the electron mean free path in the TI surface states becomes equal. Graphene, with its ultra-high mobility even at room temperature, is thus an ideal candidate for the direct experimental detection of the spin-polarized current, which until now has only been observed in 2D HgTe quantum wells at low temperatures [7, 9].

In this chapter, we show that the presence of dilute residual Cu adatoms on CVD graphene grown on Cu foil (Cu-CVD) [10–13], is sufficient to enhance the SOC strength by several orders of magnitude. This allows the generation of spin currents via spin Hall effect (SHE) [14, 15] with exceptionally large spin Hall coefficient (angle), $\gamma \sim 0.2$ comparable to what has been observed in thin films of heavy metals like gold (Au) [16], platinum (Pt) [17] or tungsten (W) [18]. Such large spin Hall coefficient is an important step towards graphene based spintronics devices within the existing CMOS technology. The results are confirmed independently by intentionally introducing metallic adatoms (Cu, Ag and Au) on pristine exfoliated graphene samples. Similar to the hydrogenated graphene samples, the enhancement in the SOC strength will be determined by studying the non-local spin Hall effect in the H-bar geometry.

6.2 Cu-CVD graphene

The growth of CVD graphene on Cu foil and the subsequent etching of Cu in ammonium per sulfate (7 gm dissolved in 1-litre of DI water) and transfer onto a Si/SiO2 substrate are performed following ref. [10]. The transferred samples are annealed in Argon/Hydrogen (90:10) environment at 320°C for 5 hours to remove any organic contaminants. Two steps of e-beam lithography, first to etch the Hall bar and the second for Cr/Au contacts are performed. The final device is again annealed in Argon/Hydrogen (90:10) environment at 300°C for 3 hours.

The CVD growth process is an ideal way to introduce metallic adatoms to graphene since it utilizes metallic thin films as substrate for growth. The presence of residual Cu atoms in CVD graphene has already been established by high resolution transmission electron microscopy images [19]. Moreover, Cu has also been used as an extrinsic impurity to induce spin-orbit coupling and spin Hall effect in metals like Pt [17]. Figure 6.1 shows the AFM image of a graphene sample decorated with Cu nanoparticles with average particle diameter of $\sim$ 30 nm and are in good agreement with the TEM results [19].

6.3 Characterization graphene samples

Prior to any transport (charge and spin) measurements, CVD graphene samples are characterized by (1) Raman spectroscopy, (2) X-ray photoelectron spectroscopy (XPS) and (3) energy dispersive X-ray spectroscopy (EDS), to estimate the quality as well as the amount of residual Cu adatoms on graphene. Figure 6.2(a) shows the Raman mapping of the G, 2D and D peak intensities of a CVD graphene Hall bar device. The Raman spectroscopy data shows that the defect peak (D-peak) in our

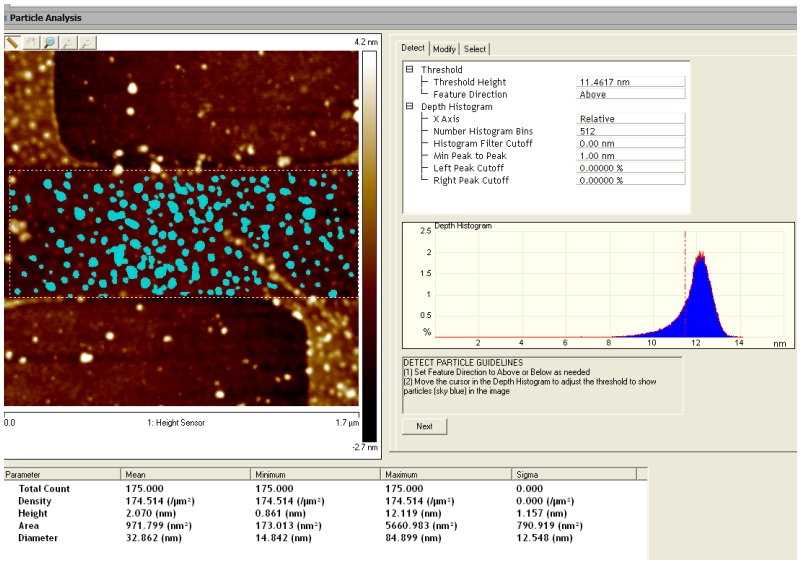

Figure 6.1: (a) AFM data for graphene sample decorated with Cu nanoparticles. The Particle Analysis function gives the details of the distribution of the particle sizes on graphene and the average Cu nanoparticle size for this sample is about 32 nm

samples is negligible compared to the G and 2D peak intensities, confirming the good quality of CVD graphene with minimum defects and/or vacancies. However, in such samples, our XPS and EDS spectrum shows the characteristic peaks for Cu (figure 6.2 (b-c)). The shape and position of the Cu peaks in the XPS spectrum also confirms that the Cu adatom on graphene is not oxidized [21].

6.3.1 Nature of Cu adsorption on Graphene

As discussed above, the XPS and EDS data clearly shows the presence of Cu adatom in CVD graphene. An idea of how the Cu adatoms are adsorbed on to the graphene lattice can be understood by analyzing the Raman data carefully. Figure 6.3 (a&b) shows the comparison of the Raman 2D and G peak position for pristine exfoliated graphene samples and Cu-CVD graphene samples. With respect to the pristine exfoliated graphene samples, the Raman 2D peak for Cu-CVD graphene shows a blue

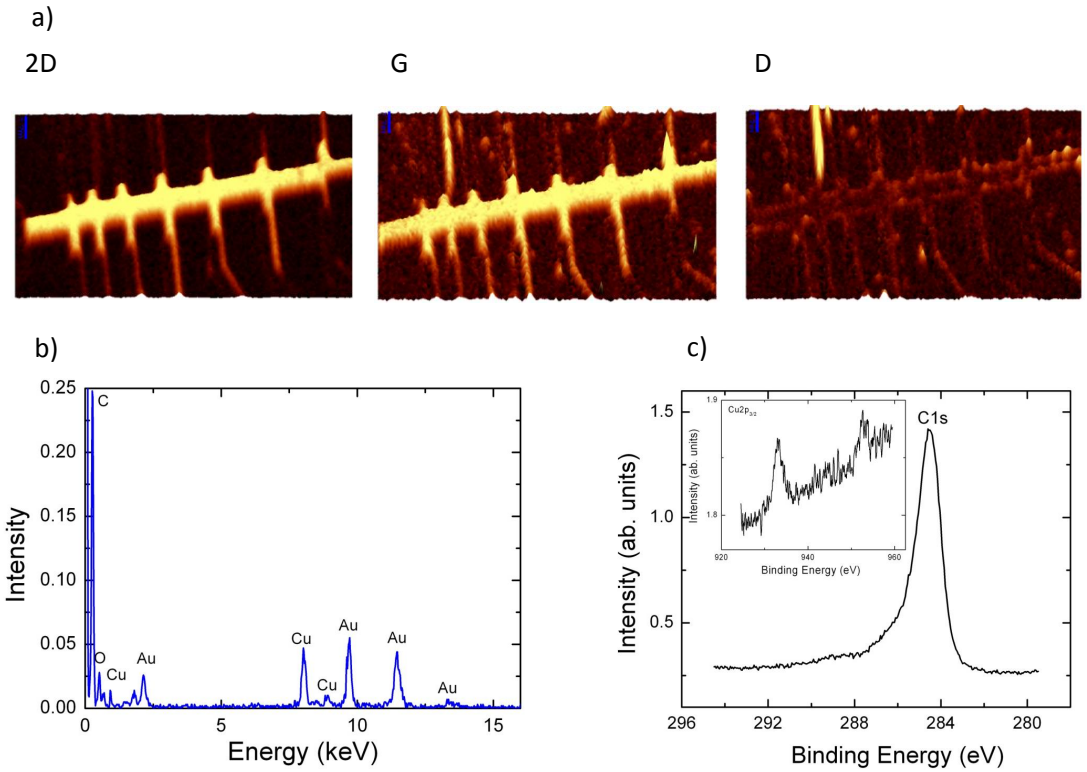

Figure 6.2: (a) Raman mapping of a Cu-CVD graphene spin Hall device showing 2D, G and D bands. The high quality of the CVD graphene can be inferred from the weak D-band intensities. The D-peak intensities are more prominent along the edges of the device which is due to the oxygen plasma induced defects at the edges, (b) Energy dispersive X-ray spectroscopy (EDS) using TEM. The samples for TEM measurements are prepared on a standard TEM gold grids. The size of each grid is 7 μm X 7 μm. The additional Au peaks in the EDS spectrum is due to the presence of Au TEM grids on which the graphene samples are prepared and (c) XPS data for CVD graphene showing the C1s peak and the inset shows the measured Cu 2p peaks.

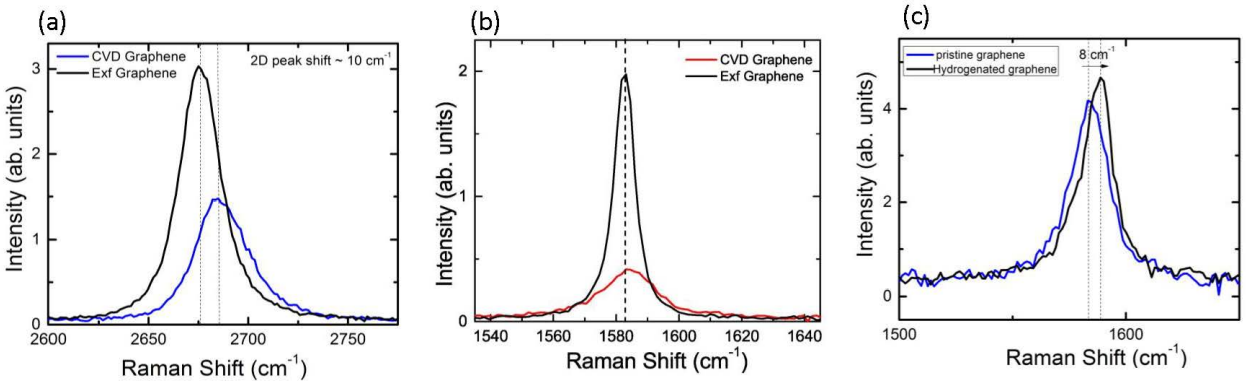

Figure 6.3: (a & b) Comparison of Raman 2D and G peak positions for Cu-CVD and exfoliated graphene samples and (c) Raman G-peak shift for hydrogenated graphene sample showing the chemisorbed nature of the adsorption.

shift of $\sim$ 10 cm^{-1} in wavenumber while the G peak shows negligible shift. The blue shift of 10 cm^{-1} in 2D peak indicates a strain of 0.3% and the relatively small G-peak shift validates the physisorbed nature of the Cu-adatom [22]. If the adatoms were chemisorbed, i.e. forms chemical bonding with the carbon atoms like in hydrogenation, the G-peak position shows a large shift of $\sim$ 10 cm^{-1} while graphene with physisorbed adatoms show negligible G-peak shift. Figure 6.3c shows the G-peak shift in weakly hydrogenated ($\sim$0.01%) graphene sample when compared with the pristine exfoliated samples. The negligible G-peak shift in our CVD graphene samples together with the XPS and EDS spectra strongly suggests not only the presence of residual Cu, but also clearly demonstrates the physisorbed nature of the Cu adatoms on graphene.

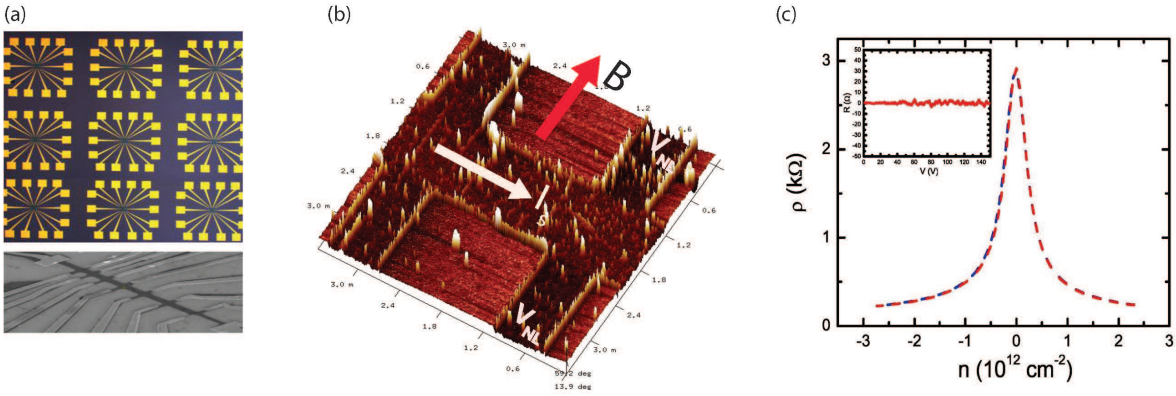

Figure 6.4: (a) Optical image of 3×3 array of devices on Si/SiO_2 substrate together with the SEM image of the active area of a typical spin Hall device. (b) AFM 3D surface topography of a typical CVD spin Hall device with details of actual measurement configurations and (c) the longitudinal resistivity as a function of carrier density for opposite pair of contacts (blue and red curves). Inset: Transverse resistance as a function of gate voltage showing the absence of any zero field Hall signal, thus eliminating the possibility of magnetic moments due to adatoms.

6.4 Transport measurements

6.4.1 Charge transport measurements

Figure 6.4 (a&b) shows the optical picture of a 3 x 3 array of spin Hall devices on a Si/SiO_2 wafer together with the scanning electron micrograph (SEM) and AFM images. Prior to any spin transport measurements, the Cu-CVD graphene devices are first characterized for charge transport using the conventional four-terminal local geometry to ensure homogeneity of the sample and only Hall junctions where the opposite pair of contacts shows identical resistivity are selected (see figure 6.4(c)). Moreover, the absence of any transverse Hall resistivity (inset figure 6.4(c)) at zero external magnetic fields confirms the uniformity of the sample [23, 24]. The absence of this anomalous Hall signal also eliminates the possibility of (Ferro) magnetic moments due to the introduction of adatoms, the presence of which could break the

required time-reversal symmetry for the realization of a 2D topological insulator state in graphene.

6.4.2 Non-local measurements

Once the devices are characterized for charge transport, non-local spin transport measurements are performed first via the conventional lateral spin-valves using ferromagnetic contacts [25–28] and then by the spin Hall measurements using gold contacts [14, 15].

6.4.2.1 Spin-valve measurements

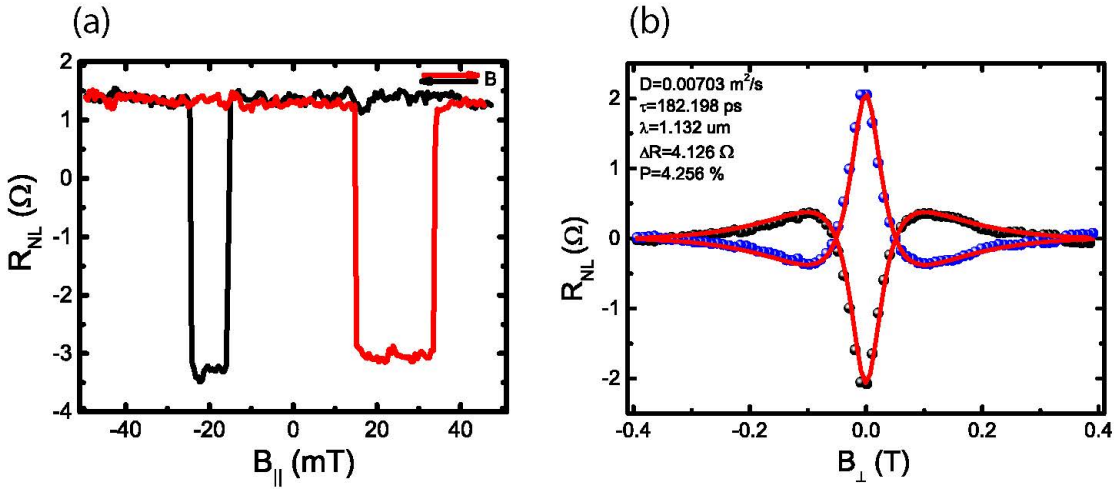

Figure 6.5: Non-local spin-valve measurements: (a) RNL vs $B_{||}$ and (b) Hanle precession measurements for Cu-CVD graphene samples.

The CVD spin-valves has the Co (35 nm) /MgO (2 nm)/CVD graphene/MgO (2 nm)/Co (35 nm) structure with a final Au capping layer, 5 nm thick, to prevent oxidation of the Co electrodes. The non-local spin-valve signals for parallel and

perpendicular magnetic field sweeps are performed following the procedure discussed in chapter 4 and is shown in figure 6.5. A fitting to the Hanle precession curve using the relation [26]

$$R_{nl} \propto \int_0^\infty \frac{1}{\sqrt{4\pi D_s t}}\, e^{\frac{-L^2}{4D_s t}}\, cos(\omega_L t)\, e^{\frac{-t}{\tau_s}} dt \tag{6.4.1}$$

gives a spin relaxation length of 1.3 μm.

6.4.2.2 Spin Hall measurements

The ferromagnet free spin Hall measurements are performed by employing only Au/Cr contacts in the non-local H-bar geometry both at room temperature (RT) and at liquid He temperatures at zero magnetic fields. In the presence of an enhanced SOC, passing a charge current through the first leg of the H-bar (contacts C1 and C2 in fig. 6.6(a)) should result in the creation of a longitudinal spin current in the graphene channel via SHE which can then be detected as a non-local voltage across the adjacent contacts (contacts C3 and C4) on the second leg by invoking the inverse spin Hall effect (iSHE) (see figure 6.6 (a) for measurement geometry). In fig. 6.6(b), we compare the non-local signal (R_{NL}) as a function of the charge carrier density n at RT, for exfoliated pristine graphene and CVD graphene with identical length to width ratio L/w = 2 and comparable mobilities ($\sim$ 5000 cm^2/Vs). We observe an exceptionally high R_{NL} $\sim$ 160 Ω for CVD graphene. On the other hand in exfoliated grapheme the measured signal is indistinguishable from the expected Ohmic contribution ($\sim$ 20). The latter follows [29, 30],

$$R_{Ohmic} = \rho e^{-\pi L/W} \tag{6.4.2}$$

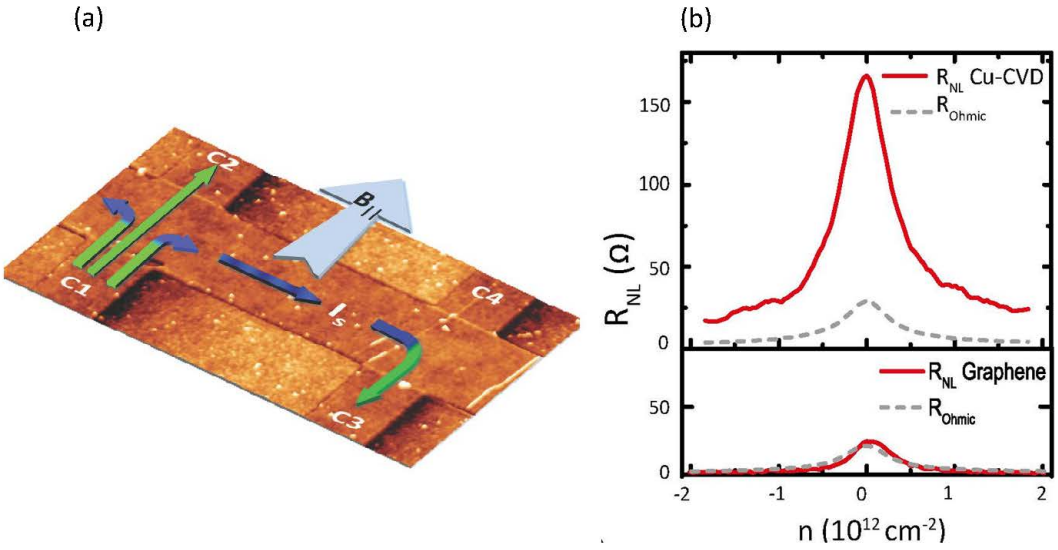

Figure 6.6: (a) Schematics showing the non-local measurement geometry and (b)non-local signal R_{NL} vs. charge carrier density for pristine graphene samples and Cu-CVD graphene samples. The dotted lines represent the calculated Ohmic leakage contribution. The L/W ratios for all the samples are ~ 2

where ρ is the resistivity of the channel, L is the length of the channel and w is the width of the channel. Since, the thermo-magneto electric effect, as discussed in ref. [31], are only present in an externally applied perpendicular magnetic field, the only remaining physical phenomenon that would give rise to a zero magnetic field non-local signal is the SHE. [14,15,32] The SHE, however, requires exceptionally large SOC strength and points to an enhanced SOC in Cu-CVD graphene when compared to exfoliated pristine graphene. Hence an unambiguous confirmation of the SHE in Cu-CVD graphene is essential. Towards this, we perform three independent experiments, viz.

1. Length dependence of the non-local signal
2. Width dependence of the non-local signal and
3. the in-plane magnetic field dependence, spin precession, of the non-local signal

6.4.3 Length and width dependence of the non-local signal

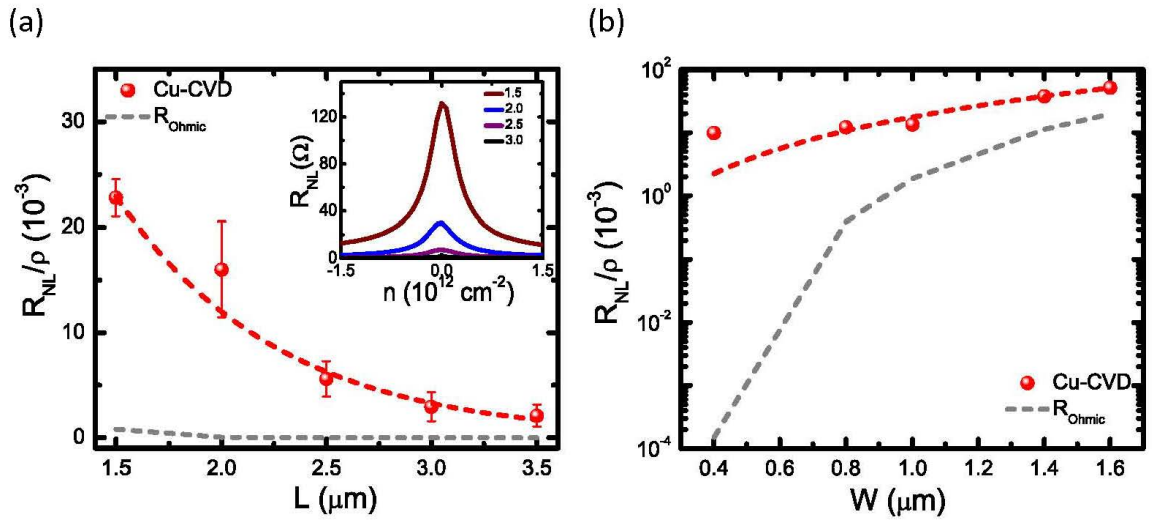

Figure 6.7: Length and width dependence of the non-local signal for Cu-CVD graphene. The inset shows the R_{NL} vs. n for different L/W ratio

For the length dependence measurement, we fix the width W of the channel and vary the length L and for the width dependence case we fix the length L of the sample and vary the width W. Here,we first discuss the length dependence of the non-local signal (fig. 6.7(a)) by fixing W = 0.5 μm and varying length L = 1.5 - 4 μm. The length dependence of the non-local signal at the charge neutrality point decays exponentially with L. Here, the exponential decay cannot be accounted for by the length dependence of the Ohmic contribution R_{Ohmic} (dashed grey line). Instead, assuming a spin-based origin our data can be fit well with the formula [29, 30]

$$R_{NL} = \frac{1}{2}\gamma^2\rho\frac{W}{\lambda_s}e^{-\frac{L}{\lambda_s}}. \tag{6.4.3}$$

Here, γ is the spin Hall coefficient (angle) defined as $\frac{spin Hall conductivity}{longitudinal resistivity} = \frac{\sigma_{xy}}{\sigma_{xx}}$, ρ is the local resistivity of the channel, and λ_s is the spin relaxation length. From this, we extract a spin relaxation length of 0.8 μm and exceptionally large spin Hall coefficient γ of 0.18. However, since both R_{NL} and R_{Ohmic} depend exponentially on the length

L, we also study the dependence of the non-local signal on the width of the device to eliminate any ambiguity arising on the measured non-local signal. For the width dependence sample, we fix the length of the sample L = 2 μm and vary the width W $\sim$ 0.6 - 1.6 μm (see figure 6.7 (b)). The width dependence of the non-local signal for Cu-CVD graphene samples show a power law dependence distinct from the Ohmic contribution (shown as grey dotted line in figure 6.7 (b)). This power law dependence can be explained by including the dependence of the λ_s on the width w of the sample. It has been theoretically predicted that λ_s varies with the width W as [33, 34]

$$\lambda_s(W) = \frac{\lambda_{so}^2}{W} \tag{6.4.4}$$

whereλ_{so} is the spin precession length defined as the length scale in which the electron spin precess a full cycle in a clean ballistic 2D system. For such samples, the non-local resistance R_{NL} at zero magnetic fields gets modified to

$$R_{NL} = \frac{1}{2}\gamma^2\rho\left(\frac{W}{\lambda_{SO}}\right)^2\left[1 - \frac{LW}{\lambda_{SO}^2} + ...\right] \tag{6.4.5}$$

The fitting of figure 6.7(b) with equation (6.4.5) gives a spin relaxation length and γ. A comparison of the values obtained from the length and the width dependence of the non-local signal is shown in Table 6.1. These values are in excellent agreement with values extracted from the length dependence data for the non-local signal and provides extra support for extrinsically generated spin Hall effect in graphene.

Table 6.1: Fitting parameters from L and W dependence

	Adatom	λ_s (μm)	γ
L dependence	Cu-CVD	0.8	0.20
W dependence	Cu-CVD	1.1	0.18

6.4.4 In-plane magnetic field dependence of the non-local signal

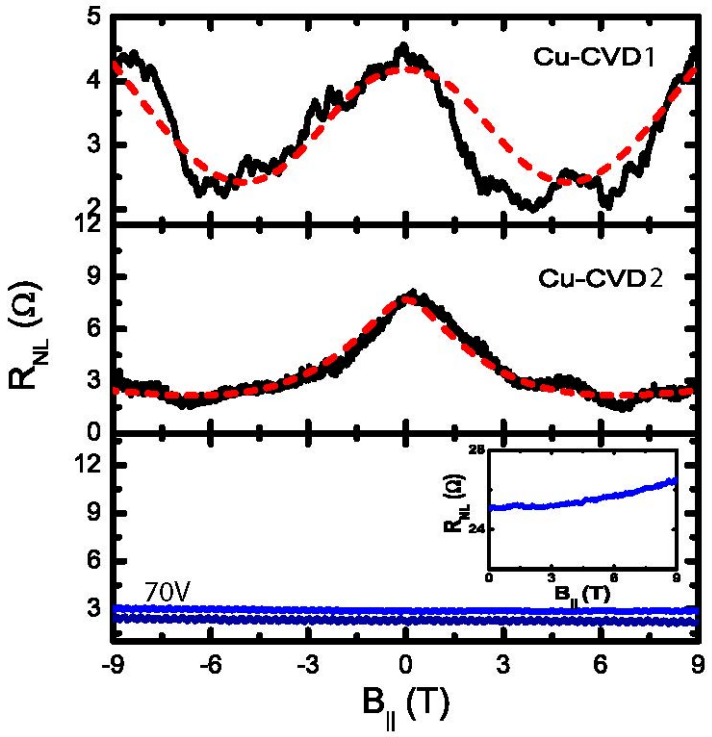

Figure 6.8: In-plane magnetic field dependence of the non-local signal for two Cu-CVD graphene samples. The amplitude of the oscillatory signal diminshes as we move away from the charge neutrality point. Inset: In-plane field dependence for a pristine exfoliated sample.

For the narrow strip geometry, as in our case, the non-local transresistance should show a monotonic oscillatory dependence with multiple sign change and damping as a function of the in-plane magnetic filed due to the precession of spins in the external field. Hence, demonstration of the spin precession is essential for the unambiguous confirmation of spin Hall effect in Cu-CVD graphene. Figure 6.8 shows the R_{NL} vs $B_{||}$ for two CVD graphene samples (CVD1 and CVD2) and pristine exfoliated graphene

sample (inset). For pristine graphene samples the characteristic oscillatory behavior is absent while the CVD show the non-monotonic oscillatory dependence of the non-local signal. The magnitude of the oscillatory signal diminishes as we move away from the Dirac point. The oscillating signal, within the diffusive regime, can be fitted with [29]

$$R_{NL} = \frac{1}{2}\gamma^2 \rho W Re\left[\frac{\sqrt{1+i\omega_B\tau_s}}{\lambda_s} e^{\left(-\frac{\sqrt{1+i\omega_B\tau_s}}{\lambda_s}\right)L}\right] \tag{6.4.6}$$

(where $\omega_B = \Gamma B_{||}$ is the Larmor frequency with Γ the gyromagnetic ratio for electron and $B_{||}$ is the applied in-plane magnetic field). The fitting gives a λ_s of 1.6 μm and 1.1 μm and a spin Hall coefficient γ of $\sim$ 0.14 and 0.18 for CVD1 and CVD2 respectively.

6.5 Identifying the cause for giant spin Hall effect in CVD graphene

The length, width and Hanle precession measurements not only confirm that the observed non-local signal is due to SHE, but also gives comparable spin parameters. It is worth noting that the spin parameters obtained from spin Hall measurements are also in good agreement with values obtained from both the conventional non-local spin-valve (see fig.6.5) [28] and spin pumping [35] measurements. All these point to a strong enhancement of the SOC in CVD graphene. Furthermore, since we do not observe SHE in exfoliated pristine graphene, its origin are extrinsic and must be due to growth defects such as wrinkles, grain boundaries, ripples, vacancies, or the organic residues coming from the Cu etching solution or the residual Cu adatoms [19]. We can rule out defects as the main contributor to the observed non-local signal since Raman mapping shows no D-peak for the entire device. We further rule out organic

residues as the dominant source by immersing identically prepared exfoliated graphene samples in the same Cu etching solution (ammonium per sulfate). In such devices the measured non-local signals are much smaller than in CVD graphene and remain comparable to the expected Ohmic contribution (see fig.6.9).

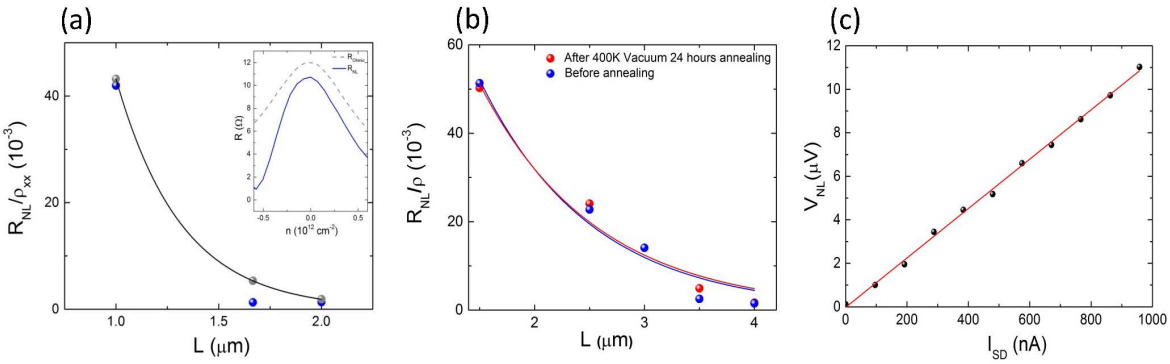

Figure 6.9: (a) Length dependence of the non-local signal for exfoliated graphene samples dipped in the etchant solution, ammonium per sulfate. The measured non-local signal is comparable to the calculated Ohmic contribution. (Inset: RNL vs. n for one junction) (b) Length dependence of the non-local signal for Cu-CVD graphene sample, before and after vacuum annealing at 400K for 24 hours. (c) Measured non-local voltage as a function of the source-drain current (V_{NL} vs. I_{SD}).

Since the growth of CVD graphene involves hydrogen environment, the possibility of the hydrogen getting bonded with the carbon atoms cannot be neglected. One way to identify the presence of hydrogen is to look at the Raman D-peak. As shown in fig.6.2, in our CVD graphene samples the Raman D-peak is prominent only at the sample edges, which can be assigned to the uneven edges of the sample due to oxygen plasma etching. However, to make sure that the contribution from any remnant hydrogen is not present to the non-local signals, we vacuum anneal the sample at 400K (limited by the maximum temperature set point of our probe) for 24 hours. Our results,fig.6.9(b), shows very little effect of annealing on the measured signal and the non-local signal before and after annealing remains the same, thus eliminating

hydrogen as the possible cause for the measured non-local signal. This leaves only residual copper adatoms as main cause for the large increase of non-local signal. This has been also recently confirmed directly by TEM measurements [19]. Indeed detailed AFM measurements show adatom clustering with average size $\sim$ 20 nm in radius and particle density of $0.6 \times 10^{10}/\text{cm}^2$) (see fig 6.1).

We directly confirm the presence of Cu also by both XPS and EDS measurements (see fig 6.2(b&c)). Note that here and unlike in ref. [3], a comparison of the Raman G-peak position in CVD graphene with that in exfoliated graphene rules out bond-angle deformation as a potential cause for the SOC enhancement [22]; in hydrogenated graphene, the Raman G-peak shows a shift of ~ 10 cm^{-1} in wavenumber (see fig.6.3). [22] However, the negligible G-peak shift in our CVDG demonstrates the physisorbed nature of the Cu adatoms on graphene (see fig.6.3). Furthermore, the Raman mapping of the D-peak intensity on the entire device shows negligible D-peak in the active device channel (see fig.6.2). All this strongly suggests proximity induced enhancement of the SOC.

Eliminating Thermo-electric contributions to non-local signal

As discussed in ref. ([31]), the measured non-local signal could have significant contributions from thermo-magneto-electric effects. However, these contributions play an important role only in the presence of a perpendicular magnetic field. In the absence of an external field in the length and width dependence measurements and in the presence of in-plane field in the spin precession measurements, the only thermal effect which could contribute to the non-local signal is the Joule heating. Since in Joule heating, the measured signal is proportional to the square of the source drain current, studying the I-V characteristics of the non-local device should provide the clear evidence, if any. Figure 6.9c shows the I-V curve for a Cu-CVD graphene device. The linear I-V clearly demonstrates that the contributions from Joule heating, if any,

to the measured non-local signal is negligible.

6.6 Control experiments on exfoliated graphene with metallic adatoms

To unambiguously establish that Cu adatoms are the dominant cause for the observed SHE in CVD graphene, we exfoliate graphene onto a Cu foil and repeat the same etching and transfer process used for CVD graphene. Lastly, similar measurements have been also performed on exfoliated pristine graphene samples decorated with Ag and Au by both solution process and thermal evaporation to confirm that the SHE is due the proximity effect caused by physisorbed metal adatoms .

6.6.1 Sample preparation

6.6.1.1 Introduction of Cu adatoms

Two different methods have been used to introduce Cu adatoms on exfoliated graphene.

1. The graphene samples are first exfoliated on to a SiO_2 substrate with Au markers. Using the standard transfer technique for graphene/boron nitride heterostructures [20], the exfoliated graphene samples together with the Au markers are peeled off with a polymer layer and then transferred on to a Cu foil. The transferred samples are first baked at 120°C in a hot plate for better adhesion. The sample on Cu foil is then placed in the Cu etchant (ammonium per sulfate, 7gm dissolved in 1-litre of DI water) [10]. The etching process which is exactly the same as the process performed for CVD graphene introduces Cu particles

on graphene.

2. A second way to introduce the Cu adatoms is to dissolve the Cu foil in the Cu etchant (ammonium per sulfate). This is followed by immersing the graphene spin Hall device on SiO_2 into the solution containing dissolved Cu.

6.6.1.2 Au and Ag deposition

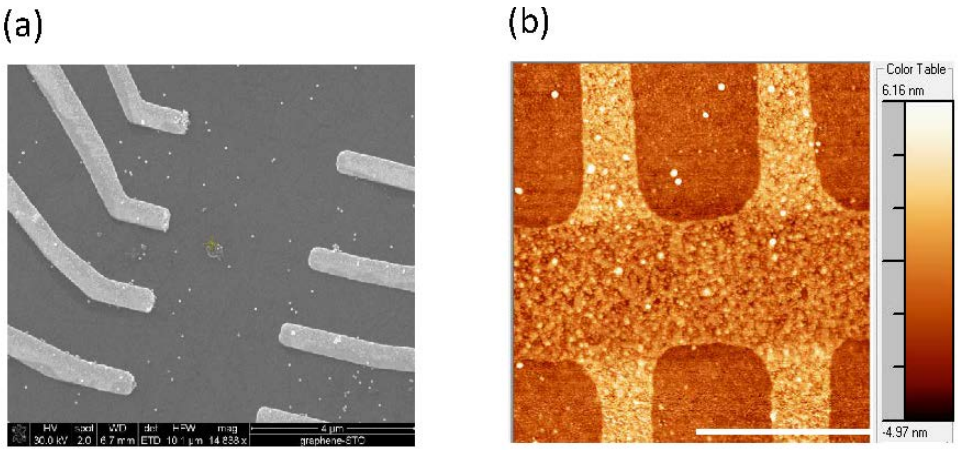

Figure 6.10: (a) SEM data for graphene sample decorated with Au nanoparticles and (b) AFM data on final spin Hall device with Au nanoparticles.

1. The Au and Ag adatoms are introduced onto the graphene by drop-casting commercially available Au/Ag colloidal solutions. The Au and Ag nanoparticles are of average size $\sim$ 30 nm. For the experiments shown in this paper, we have used the colloidal solutions bought from BBI solutions (Product code: CIKITDIAG (for Au) and ArraySC40 (for Ag)). These solutions are diluted with DI water to get different concentrations of the nanoparticles, i.e. 10^{10} particles/ml to 10^{7}particles/ml.

2. By thermal deposition of Au. Here, the deposition is performed by using the lowest deposition rate of $0.01\mathring{A}$/s and by opening and closing the shutter for

the sample for a short time period $\sim$ a second. This allows deposition of Au nanoparticles on graphene lattice with average size $\sim$ 25 nm. Figure 6.2 shows the AFM image for a graphene spin Hall device with Au adatoms and Table 6.2 shows the average diameter and particle distribution of various adatoms in our samples

Table 6.2: Adatom distribution

Adatom	Avg. Diameter (nm)	Stand. Dev.(diameter, nm)	Particle Density (cm^{-2})
Cu	40	12.6	0.6×10^{12}
Au	29	8	1.1×10^{12}

6.6.2 Transport measurements

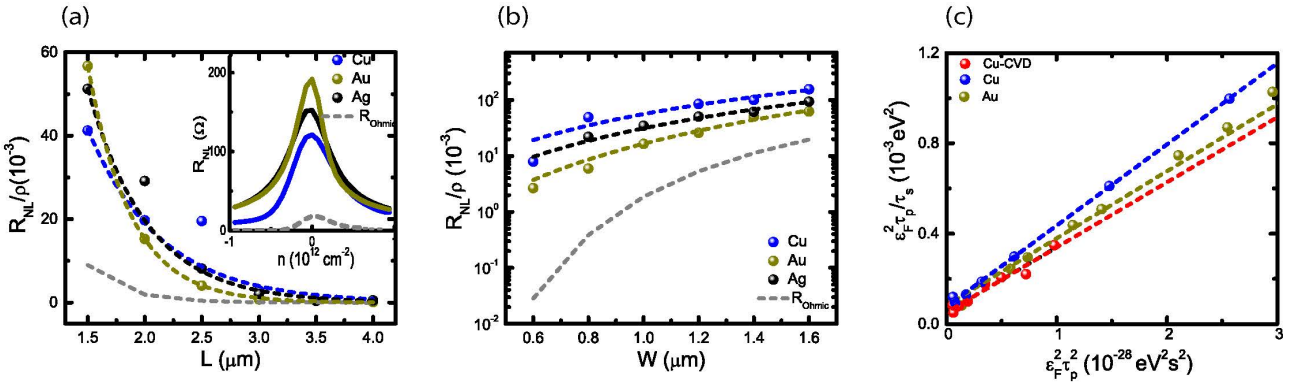

Figure 6.11: (a & b) Length and width dependence of the non-local signal for exfoliated graphene decorated with Cu, Ag and Au adatoms. The grey dotted line shows the measured non-local signal (which is equal to the Ohmic contribution) for a pristine graphene sample (Inset: R_{NL} vs n) (c) $\epsilon_F^2\tau_p/\tau_s$ vs $\epsilon_F^2\tau_p^2$ plot for various adatoms.

In exfoliated graphene samples decorated with metallic adatoms, we perform identical local and non-local measurements. In such samples, we find non-local signals comparable to the one observed for CVD samples. Figure 6.11 summarizes the length,

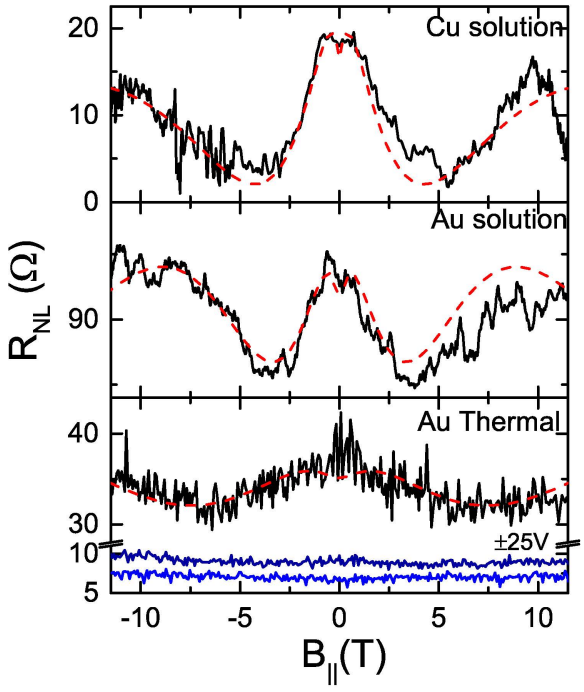

Figure 6.12: In-plane magnetic field precession measurements for graphene with Cu and Au adatoms. Far away from the charge neutrality point the oscillatory behaviour of the spin signal diminishes. The red dotted lines are fit to the experimental data.

width and Fermi energy dependence of the non-local signal for all three types of metal decoration. The fits give comparable spin relaxation lengths and spin Hall angle (see Table 6.3). The spin natures of the signals are again confirmed by Hanle precession measurements (fig. 6.12). In contrast to the exfoliated graphene dipped in etching solution only, samples with metallic adatoms show the characteristic oscillatory behavior when an in-plane magnetic field is swept.

The demonstration of SHE in exfoliated graphene decorated with metallic adatoms like Cu, Au and Ag clearly confirms our inference of residual Cu atom induced SHE in CVD graphene.

Table 6.3: Spin parameter for graphene decorarted with metallic adatom

Adatom	Mobility (cm^2/Vs)	$\lambda_s(\mu m)$	γ
Cu-CVD	11000	1.6	0.14
Cu-Exf	9000	1.1	0.27
Au-Exf	15000	2.0	0.15

6.6.2.1 Additional note on in-plane magnetic field dependence

As discussed in the previous section, as we move away from the charge neutrality point the amplitude of the oscillating signal diminishes. This is consistent with the fact that the amplitude of the non-local signal is proportional to the resistivity of the sample. Figure 6.13 shows the in-plane magnetic field dependence of the non-local signal at different back gate voltages for the same exfoliated graphene sample decorated with Au adatoms.

6.7 Estimate of spin-orbit coupling strength

The length, width and in-plane magnetic field dependence of the non-local signal unambiguously confirms the spin Hall effect in graphene decorated with metallic adatom. This inturn demonstrates that the addition of the metallic adatom enhances the spin-orbit coupling (SOC) strength in graphene and an estimate of this enhanced SOC can be determined by understanding the dominant spin relaxation mechanism in these systems. For this, we study the dependence of the spin relaxation time τ_s to the momentum relaxation time τ_p and a linear relation $\tau_s \propto \tau_p$ indicates the dominance of the EY spin scattering mechanism [36] while $\tau_s \propto \tau_p^{-1}$indicates the dominance of DP spin scattering mechanism [37]. Figure 6.14(a) shows the dependence of τ_s to the τ_p for graphene decorated with various adatoms. The data in 6.14(a) taken at a constant density $n = 1.5 \times 10^{12} cm^{-2}$ clearly shows that unlike the hydrogenated case, where a

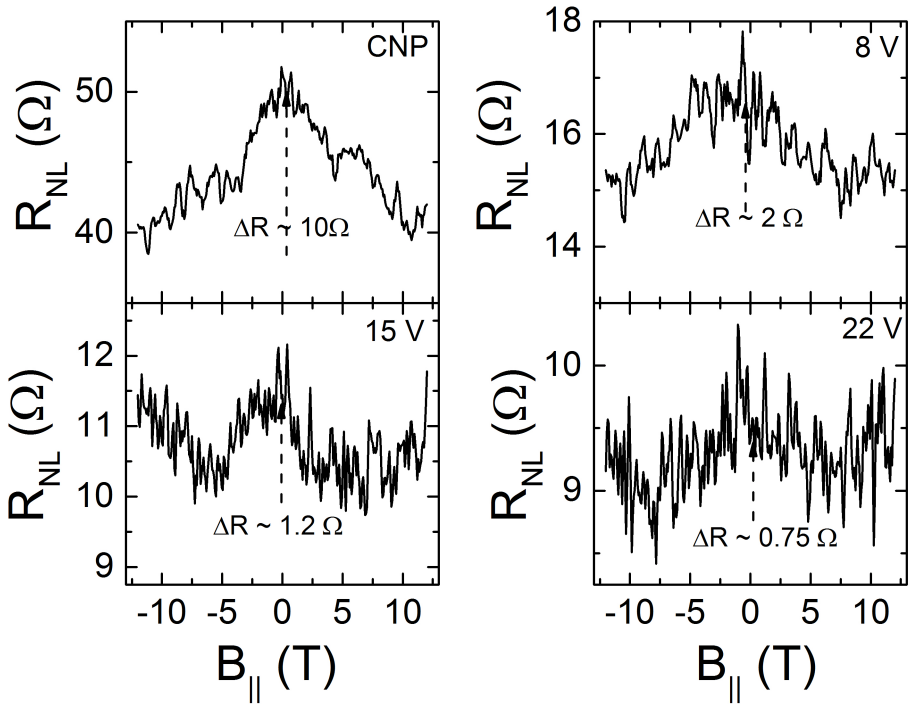

Figure 6.13: In-plane magnetic field dependence of non-local signal at different back gates for graphene decorated with Au adatoms.

clear linear relation is seen between τ_s and τ_p, in graphene with metallic adatoms, τ_s remains almost a constant with τ_p. The relation that τ_s is independent of τ_p is consistent with the EY spin scattering mechanism, if the microscopic mechanism causing spin scattering is different from that causing the charge (momentum) scattering; i.e. for instance the enhanced SOC in graphene due to adatoms cause the spin scattering while the momentum scattering is determined by the additional charge impurities introduced into the system by the adatoms [38]. However, for an unambiguous determination of the dominant spin relaxation mechanism in graphene decorated with metallic adatoms, we follow the approach employed in reference [39]. Assuming that both EY and DP scattering mechanisms are present, the spin scattering rate can be written as [39]

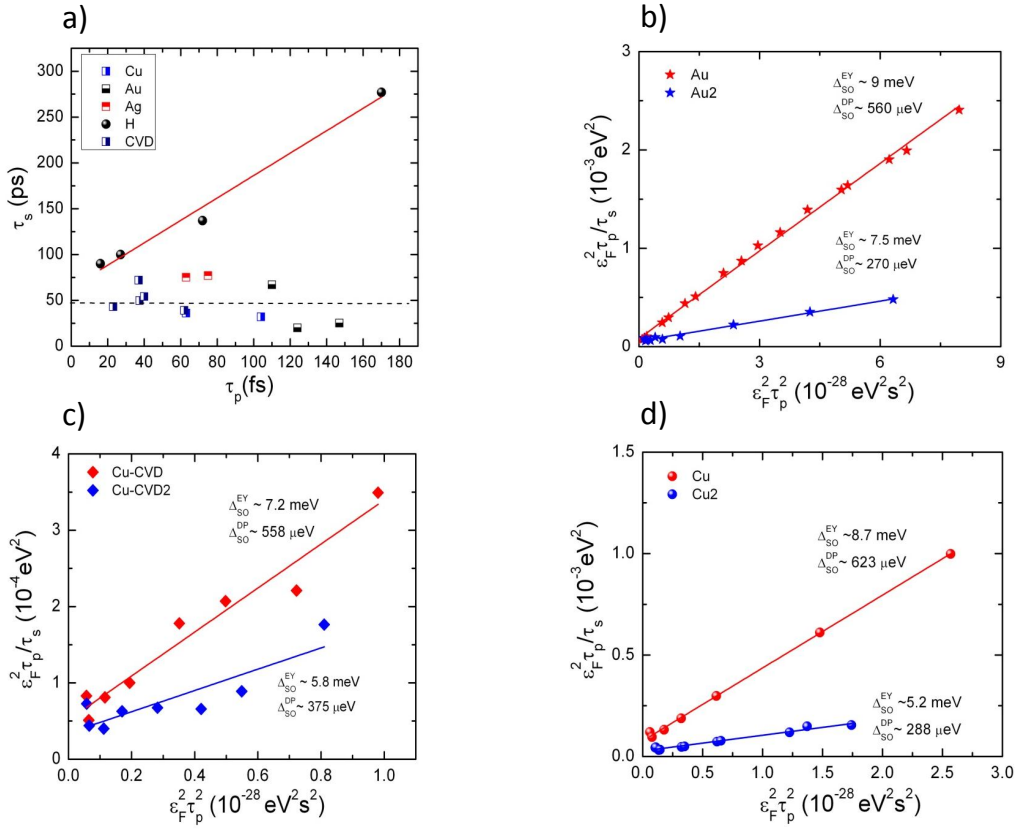

Figure 6.14: (a) τ_s vs τ_p for graphene decorated with adatoms. $\epsilon_F^2\ \tau_p/\tau_s$ vs. $\epsilon_F^2\ \tau_p^2$ for graphene decorated with (b) Au, (c) Cu (CVD) and (d) Cu (exfoliated). From the slope and y-intercept the SOC strength due to EY and DP spin scattering mechanisms are estimated.

$$\frac{1}{\tau_s} = \frac{1}{\tau_s^{EY}} + \frac{1}{\tau_s^{DP}} \tag{6.7.1}$$

where

$$\tau_s^{EY} = \frac{\epsilon_F^2}{\Delta_{EY}^2}\tau_p \tag{6.7.2}$$

and

$$\frac{1}{\tau_s^{DP}} = \frac{4\Delta_{DP}^2}{\hbar^2}\tau_p \tag{6.7.3}$$

Substituting equation (6.5.2) and (6.5.3) in equation (6.5.1), we get the relation

$$\frac{\epsilon_F^2 \tau_p}{\tau_s} = \Delta_{EY}^2 + \frac{4\Delta_{DP}^2}{\hbar^2} \epsilon_F^2 \tau_p^2 \tag{6.7.4}$$

Now from the density dependence of the longitudinal resistivity and that of the non-local signal, the quantities ϵ_F, τ_p and τ_s can be calculated for each sample, which can then be used to plot $\epsilon_F^2\ \tau_p/\tau_s$ vs. $\epsilon_F^2\ \tau_p^2$. Figure 6.14 (b-d) shows the $\epsilon_F^2\ \tau_p/\tau_s$ vs. $\epsilon_F^2\ \tau_p^2$ plot for graphene samples decorated with Au, Cu (CVD) and Cu (exfoliated) adatoms. From the slope and the y-intercept, the SOC strength contribution from both the EY and DP spin relaxation mechanisms can be estimated. Surprisingly, the estimated SOC strength is only weakly dependent on the atomic number (Z), and falls in the range of 7.5 $\pm$ 1.3 meV for CVD graphene and graphene decorated with Cu adatoms and 9 $\pm$ 2 meV for graphene decorated with Au adatoms. Note that similar to metallic thin films such a weak dependence of Z is expected [40].

6.8 Identifying dominant spin Hall scattering mechanisms

Finally, we discuss how SOC enhancement leads to the establishment of a robust SHE with such a large spin Hall coefficient (angle), γ. A large γ in pure metals such as Pt (0.01-0.1) has been ascribed to resonant scattering on impurity states split by the spin-orbit interaction [16, 41]. The importance of such resonant scatterers in graphene is also well established [42,43]. The SHE originates in asymmetric scattering in the presence of SOC: charge carriers of opposite spins are deflected in opposite directions transverse to the applied electric field. Two extrinsic mechanisms produce SHE: skew scattering (SS) and quantum-side jump (QSJ) [44]. The former arises

from asymmetry of cross sections in up/down spin channels. On the other hand, QSJ produces anomalous spin currents via spin-dependent shift (side jump) of wave packets in materials endowed with momentum-space Berry curvature. Although the latter is negligible in pristine graphene (due to very weak SOC), non-trivial Berry phase-related effects emerge in adatom-doped graphene via proximity-induced effect. In the SS (QSJ) scenario the magnitude of induced spin currents is proportional to n_{SO}^{-1} (n_{SO}^{0}) [44] where n_{SO} denotes the density of SOC active adatoms. Since all samples measured are relatively clean (i.e., small n_{SO}) we expect SS to be critical. In order to identify the SHE driving mechanism we carried out realistic transport calculations taking into account adatoms originating the observed SOC enhancement and uncontrolled sources of disorder diminishing the delivered spin Hall coefficient (angle). Our results confirm the dominance of SS mechanism in the experiments and show that the γ for Cu-CVD graphene in and around the neutrality point ($\pm$ 1×10^{12} cm^{-2}) remains almost a constant, due to the wide distribution of adatom cluster sizes. This is significant in applications for it allows the generation of robust spin currents irrespective of the initial doping level in graphene. The combination of enhanced SOC and the resonant character of large Cu clusters ($\sim$ 10 nm) make the SS mechanism extremely efficient in the production of spin currents with giant γ in the range 0.1-0.3. With respect to the absence of a strong Z dependence it is important to note that a large SOC at the impurity site is not the only criteria which can gives rise to a large SHE. A strong perturbation of the potential at the impurity site can become equally important [40]. Indeed in both CVD and EPG the perturbation of the potentialdue to the presence of metallic adatom clusters-is large and thus is likely the dominant mechanism.

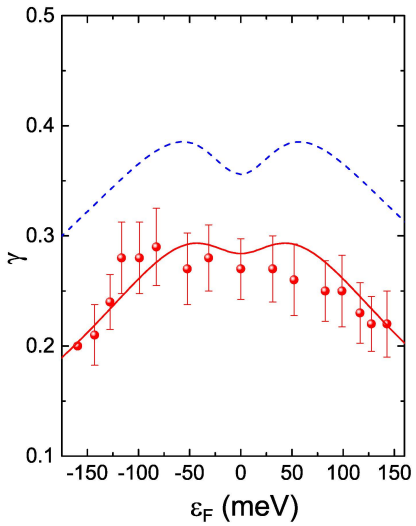

Figure 6.15: the Fermi energy dependence of the spin Hall coefficient (angle) at room temperature for the Cu-CVD graphene sample. The (dashed) blue line is the ideal spin Hall angle as generated by SOC active dilute Cu clusters in otherwise perfect graphene generated via SS. The (solid) orange line shows the realistic γ taking into account other sources of disorder (modelled here as resonant scatterers). Calculations performed at room temperature; other parameters as given in main text.

6.8.1 Theoretical modelling for giant γ

Here, we show that the giant spin Hall coefficient (angle) $\gamma \sim 0.2$ have origin in the enhancement of spin-orbit coupling (SOC) due to decoration with clusters of heavy adatoms. These SOC active clusters act as efficient (resonant) scattering centers, highly sensitive to the spin orientation of electronic currents (skew scattering), thus explaining the unusually robust spin Hall effect. Our theoretical modeling applies both to Cu-CVD graphene and decorated exfoliated graphene samples; for concreteness the discussion below is focused on the Cu-CVD samples.

The effective potential exerted by residual adatoms V_{SO} $(\vec{r})$ is an 8-dimensional Hermitian matrix (acting on valley, sub-lattice and spin subspaces), whose functional form in a realistic setup is difficult to predict *a priori*. We posit our study on a minimal model for V_{SO} $(\vec{r})$ derived from the following experimental evidence: (1) residual Cu adatoms cluster (AFM images show clusters of average size R $\sim$ 20 nm much larger than graphene's lattice spacing) justifying the neglect of inter-valley terms in V_{SO} $(\vec{r})$; and (2) the dependence of non-local resistivity curves with the Fermi energy R_{NL} (ϵ_F) present relatively small electron-hole asymmetry ($\leq 10\%$) indicating that (scalar) electrostatic terms play little role. Finally, the high-quality transport characteristics of all samples investigated justify modeling the adatoms as independent scattering centers. We are hence lead to the following minimal model:

$$V_{SO}(\vec{r}) = \sum_{i=1}^{N_{SO}} \left[\Delta_I \sigma_z s_z + \Delta_R(\sigma_x s_y - \sigma_y s_x)\right] S\delta(\vec{r} - \vec{r_i}) \tag{6.8.1}$$

In the above, $\vec{\sigma}$ and $\vec{s}$ denote Pauli matrices, with $\sigma_z = \pm 1$ [$s_z = \pm 1$] describing states on A(B) sub-lattice [with spin projections $\uparrow$ ($\downarrow$)], Δ_I and Δ_R stand for the strength of intrinsic and Rashba SOC terms, respectively, $\vec{r_i}$=(x_i, y_i) are the positions of scattering centers (areal density $n_{SO} = N_{SO}/A$) and S=$2\pi R^2$ their areal range. Higher-order SOC terms (proportional to the electronic momentum) have been neglected.

Rashba SOC arises from the breaking of reflection symmetry z $\rightarrow$ -z and is always non-zero in disordered graphene. On the other hand, intrinsic-like SOC being present in the band structure of graphene preserves the basic symmetries of the honeycomb lattice. Although this form of SOC is very weak in pristine samples (of the order of 10 μeV) [45], physisorbed species can enhance Δ_I by several orders of magnitude [2]. The Raman, XPS and EDS studies demonstrate the physisorbed nature of the SOC active scattering centers (see fig.6.2) and hence Δ_I is expected to play a central role

in the reported spin Hall effect. Likewise, the colossal enhancement of Δ_R seen in hydrogenated samples due to sp^2 to sp^3 bond conversion [3] is not expected here.

A recent study [42] also shows that the magnitude of spin Hall z-polarized currents with origin in particle-hole symmetric interactions [such as $V_{SO}(\vec{r})$] is dictated byΔ_I, being little sensitive to the Rashba coupling strength. This observation allows us to considerably simplify calculations by setting Δ_R =0 and working in subspaces of definite spin projection along z (see below).

To compute the charge and spin conductivity tensor, we solve for the semi-classical transport equations taking into account two distinct types of scattering centers: (1) adatom clusters inducing spin Hall currents via the effective potential $V_{SO}(\vec{r})$; and (2) other impurities/defects affecting charge transport. The transport characteristics of Cu-CVD graphene strongly suggest that residual Cu adatoms give the main contribution to inverse transport lifetimes (and thus transport cross sections). The inclusion of (2) in the transport calculations is needed for a rigorous comparison with the experimental data (impurities/defects uncorrelated with the SOC-active adatoms diminishes the magnitude of the spin Hall current). The total inverse transport lifetime is therefore computed as $\tau_{\|}^{-1} = \tau_i^{-1} + \tau_{SO}^{-1}$, where $\tau_{SO}(\tau_i)$ denotes the transport lifetime of SOC active clusters (other impurities/defects).

The analytic expression for the full charge and spin conductivity tensor at finite temperature can be obtained in closed form as shown in Ref. [42]. In the presence of SOC the exact solution of the Boltzmann transport equations involves two distinct lifetimes: the usual longitudinal (transport) scattering time $\tau_{\|}$ and a transverse lifetime $\tau_{\perp}$ associated with asymmetric (skew) scattering. SOC active clusters contribute with finite skew relaxation time determined by [42]

$$\tau_{\perp}^{-1}(\vec{k},s)=\frac{2\pi n_{SO}}{\hbar}\int\frac{d^2\vec{p}}{(2\pi)^2}\left|T(\vec{p},\vec{k})\right|^2 sin(\theta_{\vec{p}}-\theta_{\vec{k}})\delta(\epsilon_{\vec{p}}-\epsilon_{\vec{k}}), \tag{6.8.2}$$

where $T(\vec{p},\vec{k}) = \left\langle \vec{p},s\left|T\right|s,\vec{k}\right\rangle$ are matrix elements of the T-matrix associated with eq. 6.8.1, $\left|s,\vec{k}\right\rangle$ are the graphene eigenstates of definite momentum $\vec{k}$ and spin projection $s = \vec{s}\cdot\vec{e_z}$, $\theta_{\vec{r}}$ is the angle that the vector $\vec{r}$ forms with the direction of the external electric field, and $\epsilon_{\vec{k}} = \lambda\hbar v_F|\vec{k}|$ is the graphene's dispersion relation ($\lambda=\pm1$ denotes the carrier polarity and v_F the Fermi velocity). A finite value $\tau_\perp<\infty$ (skew scattering) has two effects: (1) the emergence of spin transverse currents and hence non-zero spin Hall conductivity i.e., $\sigma_{sH}=((2e^2)/h)(\epsilon_F/\hbar)\tau_\perp/[1+(\tau_\perp/\tau_\parallel)^2]$ (here all quantities being evaluated at the Fermi surface $\epsilon_{\vec{k}}=\epsilon_F$), and (2) the modification of the standard longitudinal conductivity according to $\sigma=((2e^2)/h)\epsilon_F\ \tau_\parallel^{eff}/\hbar$, with $\tau_\parallel^{eff}=\tau_\parallel/[1+(\tau_\parallel/\tau_\perp)^2]$. Below, we compute carrier lifetimes and present the general formula for spin Hall angle produced via skew scattering.

To make contact with the experiments, we model the (non-SOC) disorder by resonant impurities, whose importance in graphene is well established [43]. The inverse lifetime of resonant scatterers (areal density n_i) is given by $\tau_i^{-1}=n_i(2\hbar v_F)^{-2}\ v_F\left|\vec{k}\right|/|g(a)|^2$. Here, a is the scatterer range and $g(x)=\frac{\lambda|\vec{k}|}{2\pi\hbar v_F}\ln(\left|\vec{k}\right|x)-\frac{|\vec{k}|}{4\hbar v_F}i$ stands for the Dirac fermion propagator with short-distance cut-off x. The inverse lifetime associated with the clusters (Eq. 6.8.1) is given by the familiar golden rule

$$\tau_{SO}^{-1}=\frac{2\pi n_{SO}}{\hbar}\int\frac{d^2\vec{p}}{(2\pi)^2}\left|T(\vec{p},\vec{k})\right|^2[1-cos(\theta_{\vec{p}}-\theta_{\vec{k}})]\delta(\epsilon_{\vec{p}}-\epsilon_{\vec{k}}). \tag{6.8.3}$$

We obtain $\tau_{SO}^{-1}=n_{SO}(2\hbar v_F)^{-2}\ |T|^2$, where $|T|^2=|t_1|^2+|t_{-1}|^2$ - $\mathrm{Re}(t_1t_{-1}^*)$ and $t_{\pm1}=\pm\Delta_I S/[1\pm\Delta_I Sg(R)]$. Finally, evaluation of eq. 6.8.2 yields the inverse skew lifetime: $\tau_\perp^{-1}=n_{SO}(2\hbar v_F)^{-2}sv_F\left|\vec{k}\right|\ |T_\perp|^2$, where $|T_\perp|^2=\mathrm{Re}(t_1)\mathrm{Im}(t_{-1})$- $\mathrm{Re}(t_{-1})\mathrm{Im}(t_1)$. From

the knowledge of these lifetimes, the charge and spin polarized conductivity tensor at finite temperature can be easily computed. The non-zero entries are

$$\sigma_{sH}^{yx}(T) = -e^2 \frac{g_v}{2\hbar} \sum_{s=\pm 1} \int_{-\infty}^{\infty} d\epsilon \, |\epsilon| \, \frac{\partial f(T)}{\partial \epsilon} \frac{s\tau_{\perp}(\epsilon, s)}{1 + (\frac{\tau_{\perp}(\epsilon,s)}{\tau_{\parallel}(\epsilon,s)})^2}, \tag{6.8.4}$$

$$\sigma^{xx}(T) = -e^2 \frac{g_v}{2\hbar} \sum_{s=\pm 1} \int_{-\infty}^{\infty} d\epsilon \, |\epsilon| \, \frac{\partial f(T)}{\partial \epsilon} \frac{\tau_{\parallel}(\epsilon, s)}{1 + (\frac{\tau_{\parallel}(\epsilon,s)}{\tau_{\perp}(\epsilon,s)})^2}, \tag{6.8.5}$$

σ_{sH}^{xy} = -σ_{sH}^{yx} and $\sigma^{yy} = \sigma^{xx}$. In the above, $g_v = 2$ (valley degeneracy) and *f(T)* = 1/[1 + $e^{(\epsilon-\epsilon_F)/k_BT}$] denotes the Fermi-Dirac distribution function.

The spin Hall coefficient (angle) γ is defined as the ratio of the spin z-polarized transverse current to the steady state longitudinal current for a system driven by an electric field along the x direction, i.e.,

$$\gamma(T) = \frac{\sigma_{sH}^{yx}(T)}{\sigma^{xx}(T)}. \tag{6.8.6}$$

In our model, s_z is conserved and thus lifetimes have the symmetry properties: $\tau_{\perp} \equiv \tau_{\perp}(\vec{k}, 1) = -\tau_{\perp}(\vec{k}, -1)$ and $\tau_{\parallel} \equiv \tau_{\parallel}(\vec{k}, 1) = -\tau_{\parallel}(\vec{k}, -1)$ which allows simplification of the conductivity tensor. At zero temperature Eq. (6.8.6) acquires a particularly enlightening form: $\gamma(0)=\tau_{\parallel}/\tau_{\perp}$, clearly showing the role of skew scattering in establishing pure spin (transverse) currents. The expected spin Hall angle (Eq. 6.8.6) and the experimental γ are shown in Fig.6.15. The most salient features are: (1) remarkably largeγ due to resonant skew scattering as recently predicted in a related model [42] and (2) small amplitude of variations in γ as the Fermi energy is swept. The latter is explained by the wide distribution of cluster sizes R in the Cu-CVD sample (see below) that quenches otherwise pronounced variations of transport quantities with Fermi energy. As anticipated above, the non-SOC impurities (here

modeled by resonant scatterers) considerably diminish the magnitude of the spin Hall angle for they decrease $\tau_{\|}$ and produce no effect on $\tau_{\perp}$.

6.8.1.1 Choice of parameter

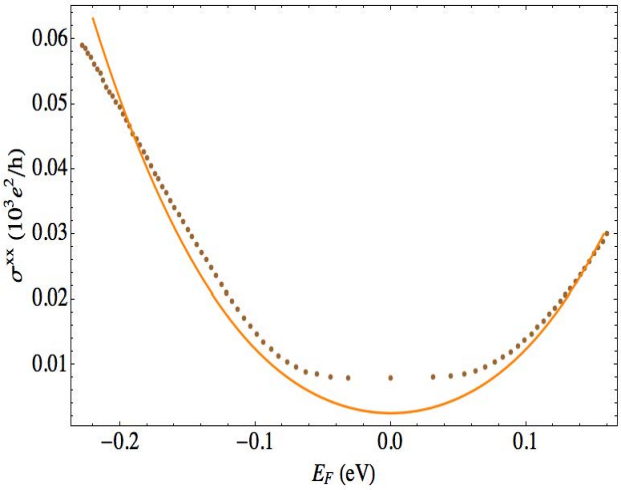

Figure 6.16: the Fermi energy dependence of the longitudinal (charge) conductivity at room temperature for the Cu-CVD graphene sample. The (solid) orange line shows the theoretical value of the conductivity as computed from Eq. 6.8.5. The excellent qualitative agreement shows that fit parameters are consistent with charge transport characteristics of the system. (Parameters as in Fig. 6.15.)

The parameters used in Fig. 6.15 are representative of the Cu-CVD sample. Cluster geometric features have been taken directly from the experiment (AFM studies show an average cluster radius R≈ 2 0nm with standard deviation ≈ 6 nm) as to perform realistic disorder averaging in Figures 6.15 and 6.16; Gaussian distributions have been used. From the spin precession data (see manuscript) we estimate a lower bound [46] for Δ_I in the range 6.2 - 11 meV. In our calculations we have taken a conservative value $\Delta_I \simeq 9.5$ meV. Finally, the values for (a,n_i) and n_{SO} were found by requiring a fine agreement between theory and experiment in both γ(T) and σ^{xx}(T) (see Fig. 6.16). The obtained values-a $\simeq 2.5$ nm, $n_i \simeq 3.84\times 10^{10}$ cm^{-2} and $n_{SO} \simeq 1.04\times 10^{11}$

cm^{-2} are consistent with preparation methods of the CVD graphene samples. The estimated concentration of SOC active dilute Cu clusters $n_{SO} \simeq 1.04\times10^{11}$ cm^{-2} is one order of magnitude larger than the lower bound set by the AFM images.

6.8.1.2 Driving mechanisms for the spin Hall effect

The quality of the fits shown in Fig. 6.15 and 6.16, as well as their consistency with the main characteristics of the Cu-CVD graphene sample, emphasizes the importance of skew scattering (SS) in the experiment. We should note, however, that transverse spin currents could also arise from another mechanism, namely the quantum side jump (QSJ). The latter results from the shift of wave-packets associated with charge carriers as they scatter from SOC potentials (see Ref. [47] for a comprehensive review on the QSJ). Our calculations show that QSJ provides corrections to up to 30%. However, we were not able to find consistent parameter ranges for which QSJ would dominate over SS (this would require dirty samples with much larger n_{SO}). For this reason, we are lead to conclude that SS is the driving mechanism for the large spin Hall angles reported in this work.

6.9 Conclusion

In conclusion, we have shown that the Cu-CVD graphene has a spin-orbit coupling three orders of magnitude larger than that of pristine exfoliated graphene samples. The enhancement in the SOC in Cu-CVD graphene is due to the presence of residual Cu adatoms introduced during the growth and transfer process. We confirm this by introducing Cu adatoms to exfoliated graphene samples and extract a SOC value comparable to the one in Cu-CVD graphene $\sim$ 7.5 meV. In addition to Cu, we also

show that adatoms like Au and Ag can also be used to induce such enhancement of SOC in pristine graphene. An enhancement of graphenes SOC is key to achieving a robust 2D topological insulator state in graphene [5, 49]. Also, the observation of a robust SHE with exceptionally large $\gamma \sim 0.2$ at room temperature is a first but important step towards introducing graphene for spin based concepts such as spin transfer torque based magnetic memory and spin logic applications [18, 48]. Since the effect is equally strong with commonly used non-magnetic metals such as Cu, these applications would be also compatible with existing CMOS technology.

Bibliography

[1] A. H. Castro Neto and F. Guinea, Phys. Rev. Lett. **103**, 026804 (2009).

[2] W. Conan, H. Jun, A. Jason, F. Marcel, W. Ruqian, Phys. Rev. X **1**, 021001 (2011).

[3] J. Balakrishnan, G. K. W. Koon, M. Jaiswal, A. H. Castro Neto and B. Oezyilmaz, Nat. Phys. **9**, 284 (2013).

[4] K.-H. Jin and S.-H. Jhi, Phys. Rev. B **87**, 075442 (2013).

[5] D. W. Ma, Z. Y. Li, Z. Q. Yang, Carbon **50**, 297 (2012).

[6] J. Ding, Z. H. Qiao, W. X. Feng, Y. G. Yao and Q. Niu, Phys Rev B 84, 195444 (2011).

[7] C. Brune, A. Roth, E. G. Novik, M. Konig, H. Buhmann, E. M. Hankiewicz, W. Hanke, J. Sinova and L. W. Molenkamp, Nat. Phys. **6**, 448 (2010).

[8] Y. Ando, arXiv: 1304.5693

[9] C. Brune, A. Roth, H. Buhmann, E. M. Hankiewicz, L. W. Molenkamp, J. Maciejko, X.-L. Qi and S.-C. Zhang, Nat. Phys. **8**, 485 (2012).

[10] S. Bae, H. Kim, Y. Lee, X. Xu, J.-S. Park, Y. Zheng, J. Balakrishnan, T. Lei, H. R. Kim, Y. Song, Y.-J. Kim, K.S. Kim, B. Oezyilmaz, J.-H. Ahn, B. H. Hong and S. Iijima, Nat. Nano. **5**,574 (2010).

[11] X. Li, W. Cai, J. An, S. Kim, J. Nah, D. Yang, R. Piner, A. Velamakanni, I. Jung, E. Tutuc, S. K. Banerjee, L. Colombo and R. S. Ruoff, Science **324**,1312 (2009).

[12] K.S. Kim, Y. Zhao, H. Jang, S. Y. Lee, J. M. Kim, K. S. Kim, J.-H. Ahn, P. Kim, J.-Y. Choi and B. H. Hong, Nature **457**, 706 (2010).

[13] A.Reina, X. Jia, J. Ho, D. Nezich, H. Son, V. Bulovic, M. S. Dresselhaus and J. Kong, Nano Lett. **9**,30 (2009).

[14] M. I. Dyakonov and V. I. Perel, Jetp Letters-Ussr **13**, 467 (1971).

[15] J. E. Hirsch, Phys. REv. Lett. **83**, 1834 (1999).

[16] T. Seki, Y. Hasegawa, S. Mitani, S. Takahashi, H. Imamura, S. Maekawa, J. Nitta and K. Takanashi, Nat. Mater. **7**, 125 (2008).

[17] H. Nakayama, K. Ando, K. Harii, Y. Kajiwara, T. Yoshino, K. Uchida, T. Ota and E. Saitoh, J. Phys.: Conf. Ser. **200**, 062014 (2010).

[18] C. F. Pai, L. Liu, Y. Li, H. W. Tseng, D. C. Ralph and R. A. Buhrman, arXiv: 1208.1711 (2012).

[19] Y.-C. Lin, C.-C. Lu, C.-H. Yeh, C. Jin, K. Suenaga and P.-W. Chiu, Nano. Lett. **12**, 414 (2012).

[20] C. R. Dean, A. F. Young, I. Meric, C. Lee, L. Wang, S. Sorgenfrei, K. Watanabe, T. Taniguchi, P. Kim, K. L. Shepard and J. Hone, Nat. Nano. **5**, 722 (2010).

[21] S. Chen, L. Brown, M. Levendorf, W. Cai, S.-Y. Ju, J. Edgeworth, X. Li, C. W. Magnuson, A. Velamakanni, R. D. Piner, J. Kang, J. Park and R. S. Ruoff, ACS Nano **5**, 1321 (2011).

[22] R. He, L. Zhao, N. Petrone, K. S. Kim, M. Roth, J. Hone, P. Kim, A. Pasupathy and A. Pinczuk, Nano Lett. **12**, 2408 (2012).

[23] W van der Wel, C. J. P. M. Harmans and J. E. Mooij, J. Phys. C: Solid State Phys. **21**,L171 (1988).

[24] J. Guignard, D. Leprat, D. C. Glattli, F. Schopfer and W. Poirier, Phys. Rev. B. **85**,165420 (2012).

[25] N. Tombros, C. Jozsa, M. Popinciuc, H. T. Jonkman and B. J. van Wees, Nature **448**, 571 (2007).

[26] T.-Y. Yang, J. Balakrishnan, F. Volmer, A. Avsar, M. Jaiswal, J. Samm, S. R. Ali, A. Pachoud, M. Zeng, M.Poinciuc, G. Guntherodt, B. Beschoten and B. Ozyilmaz, Phys. Rev. Lett. **107**, 047206 (2011).

[27] W. Han and R. K. Kawakami, Phys. Rev. Lett. **107**, 047207 (2011).

[28] A. Avsar, T.-Y. Yang, S. Bae, J. Balakrishnan, F. Volmer, M. Jaiswal, Z. Yi, S. R. Ali, G, Guentherodt, B.-H. Hong, B. Beschoten and B. Ozyilmaz, Nano Lett. **11**, 2363 (2011).

[29] D. A. Abanin, A. V. Shytov, L. S. Levitov and B. I. Halperin, Phys. Rev. B **79**, 035304 (2009).

[30] G. Mihajlovic, J. E. Pearson, M. A. Garcia, S. D. Bader and A. Hoffmann, Phys. Rev. Lett. **103**, 166601 (2009).

[31] J. Renard, M. Studer and J. Folk, arXiv: 1309.7016v1 (2013).

[32] M. I. Dyakonov and V. I. Perel,Phys. Lett. A **35**, 459 (1971).

[33] S. Kettamann, Phys. Rev. Lett. **98**, 176808 (2007).

[34] W. Paul and K. Stefan *in Handbook of Nanophysics: Nanotubes and Nanowires* Ch 28, (CRC Press) (2010).

[35] A. K. Patra, S. Singh, B. Barin, Y. Lee, J.-H. Ahn, E. del Barco, E. R. Mucciolo and B. Oezyilmaz, Appl. Phys. Lett. 101, 4761932 (2012).

[36] R. J. Elliott, Phys. Rev. **96**, 266 (1954).

[37] M. I. Dyakonov and V. I. Perel, Sov. Phys. Solid State **13**, 3023 (1972).

[38] W. Han, J.-R. Chen, D. Wang, K. M. McCreary, H. Wen, A. G. Swartz, J. Shi and R. Kawakami, Nano Lett. **12**, 3443 (2012).

[39] P. J. Zomer, M. H. D. Guimaraes, N. Tombros, and B. J. van Wees, Phys. Rev. B **86**, 161416(R) (2012).

[40] M. Gradhand, D. V. Fedorov, P. Zahn and I. Mertig, Phys. Rev. Lett. **104**, 186403 (2010).

[41] A. Fert and P. M. Levy, Phys. Rev Lett. **106**, 157208 (2011).

[42] A. Ferreira, T. G. Rappoport, M. A. Cazallila and A. H. Castro Nato, arXiv:1304.7511v2 (2013).

[43] A. Ferreira, J. Viana-Gomes, J. Nilsson, E. R. Mucciolo, N. M. R. Peres and A. H. Castro Neto, Phys. Rev. B **83**, 165402 (2011).

[44] S. Maekawa, Ed., Concepts in Spin Electronics, Ch 8, p363-367 (Oxford University Press, 2006).

[45] D. Huertas-Hernando, F. Guinea,and A. Brataas Phys. Rev. B **74**, 155426 (2006).

[46] Intrinsic SOC conserves spins polarized in the z direction; hence Δ_I can be larger than the SOC strength as estimated from the conventional Elliot-Yafet formula.

[47] N. A. Sinitsyn, J. Phys. Condens. Matter **20**, 023201 (2007).

[48] P. Nemec, E. Rozkotova, N. Tesarova, F. Trojanek, E. De. Ranieri, K/ Olejnik, J. Zemen, V. Novak. M. Cukr, P. Maly and T. JUngwirth, Nature Phys. **8**, 411 (2012).

[49] J. Hu, J. Alicea, R. Wu, and M. Franz, Phys. Rev. Lett.**109**, 266801 (2012).

Chapter 7

Summary and Outlook

In this thesis, an effort has been made to understand the spin transport properties of bilayer and functionalized graphene. The experiments performed for these systems are based on

1. the non-local spin valve structure employing ferromagnetic electrodes for injection and detection of spin currents.
2. the non-local spin Hall effect employing the H-bar geometry without the need for any ferromagnetic elements in the device architecture.

7.1 Spin-valve experiments

For the non-local spin valve experiments, unlike the previous works on single layer graphene, we identified bilayer graphene as our system of study due to

1. the unique electronic properties of bilayer graphene which differ from that of single layer graphene,*viz.* effective mass of charge carriers, electric field induced band gap and

2. the efficient screening of charge impurities and hence reduced scattering from charge impurities. This is important since in single layer graphene it is currently believed that the spin relaxation is dominated by momentum scattering from charge impurities and hence bilayer graphene due to its enhanced charge screening is a unique system by itself. This also implies the importance of short range scatterers in determining the transport properties.

In order to understand and to identify the nature of spin relaxation in bilayer graphene, the dependency of the spin relaxation time, estimated from the non-local spin valve measurements, was studied as a function of (1) the field effect mobility μ (2) the minimum conductivity σ_{min}, (3) the charge carrier density n and (4) the temperature T. Our systematic analysis showed that the spin relaxation in bilayer graphene is dominated by the D'yakonov-Perel' type spin scattering with spin relaxation times up to 2 ns at room temperature [1].

An interesting direction to proceed further on the studies of the spin relaxation in bilayer graphene could well be

1. the influence of a band gap opening in the spin transport properties of bilayer graphene and

2. studying the influence of the second sub band on the spin transport properties of bilayer graphene. This can be achieved by using a top ionic gate which would allow the filling of high energy subbands in bilayer graphene at densities $\geq 2.4 \times 10^{13}/\mathrm{cm}^2$ [2].

7.2 Spin Hall experiments

In the second half of the thesis, we focused on methods to enhance the spin-orbit coupling in graphene. Towards this, the method identified was to functionalize graphene with adatoms like hydrogen. Here the out-of-plane deformation of the graphene lattice due to the sp^3 bonding with the hydrogen atoms results in the enhancement of the spin-orbit coupling from a few μeV to a few meV. Our non-local spin Hall measurements show the spin-orbit strength in the weakly hydrogenated samples to be of the order of 2.5 meV. Such large enhancement of the spin-orbit coupling is important for the realization of the graphene based spin-FET's and an ideal 2D topological insulator state. In such hydrogenated samples, the enhancement of the spin-orbit coupling was demonstrated by non-local spin Hall measurements and spin precession measurements [3].

As an independent measurement, the spin splitting in hydrogenated graphene can also be demonstrated by studying the longitudinal resistance as a function of the magnetic field applied at tilted angles. Here, the magnitude of the perpendicular component of the magnetic field is kept constant while varying the in-plane parallel magnetic field component. Figure 7.1 shows the longitudinal resistance as a function of the back gate voltage for varying in plane magnetic field and a constant perpendicular field $B_\perp$ = 4.94 T at $T = 3.45$ K. The Shubnikov-de-Haas (SdH) oscillations show a graduate phase shift with the increase of the parallel field and reverses its phase at the highest field of $B_\parallel$ = 15.2 T. Such a phase reversal has been explained by Fang and Stiles in their seminal work [4] as due to the fact that the spin splitting is not fully resolved; *i.e.*, the energy separation of the spin levels of the adjacent Landau states ($\hbar\omega_c$ - $g\mu_B B$) is smaller than the spin splitting and cannot be resolved in this case resulting in the phase reversal of the SdH oscillations. These initial results are promising and require further measurements to be performed for any quantitative analysis and this

will be our next step.

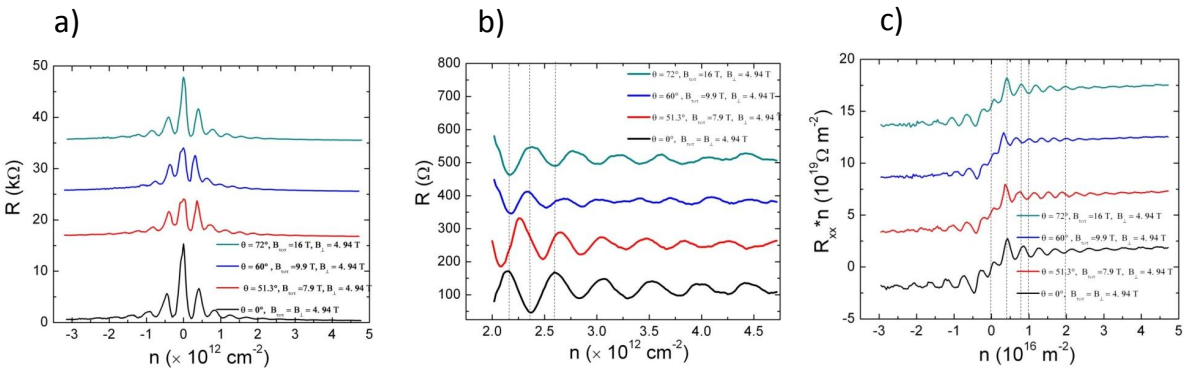

Figure 7.1: a) Resistance of the weakly hydrogenated graphene sample as a function of the carrier density for different tilt angles. Here the perpendicular magnetic field is kept at a constant value while varying the in-plane field. The graph is shifted in the y-axis for better visibility. (b) the same graph showing the change in the phase of the SdH peaks with varying tilt angle.(c) R*n vs n of the weakly hydrogenated graphene sample for different tilt angles the graph shifted in the y-axis for better visibility.

Moreover, the demonstration of spin Hall effect in functionalized graphene also opens the door for many other interesting experiments. Some of the experiments which are of interest are

1. understanding the effect of the substrate on the deformation of the graphene lattice upon functionalization by performing similar experiments on graphene deposited on BN, MoS_2 etc.

2. functionalize graphene with other adatoms like fluorine. Here, since fluorine atoms are known to form both covalent and ionic bonding, performing non-local spin Hall measurements on this system will be quite interesting.

3. studying the influence of substrates with very high spin orbit coupling on graphene.

Bibliography

[1] T.-Y. Yang*, J. Balakrishnan*, F. Volmer, A. Avsar, M. Jaiswal, J. Samm, S. R. Ali, A. Pachoud, M. Zeng, M. Popinciuc, G. Güntherodt, B. Beschoten and B. Özyilmaz, Phys .Rev. Lett **107**, 047206 (2011).

[2] D. B. Efetov, P. Maher, S. Glinskis and P. Kim, Phys. Rev. B **84**, 161412 (2011).

[3] J. Balakrishnan, G. K. W. Koon, M. Jaiswal, A. H. Castro Neto, B. Özyilmaz, Nat. Phy. **9**, 284 (2013).

[4] F. F. Fang and P. J. Stiles, Phys. Rev. **174**, 823 (1968).

List of Publications

1. Jayakumar Balakrishnan*, Gavin Kok Wai Koon*, Manu Jaiswal, A. H. Castro Neto, Barbaros Özyilmaz, Colossal Enhancement of Spin-Orbit Coupling in Weakly Hydrogenated Graphene, Nature Physics **9**, 284 (2013).

2. Tsung-Yeh Yang*, Jayakumar Balakrishnan*, F. Volmer, A. Avsar, M. Jaiswal, J. Samm, S. R. Ali, A. Pachoud, M. Zeng, M. Popinciuc, G. Güntherodt, B. Beschoten and Barbaros Özyilmaz," Observation of Long Spin Relaxation Times in Bilayer Graphene at Room Temperature", Physical Review Letters **107**, 047206 (2011).

3. A. Avsar*, T.-Y. Yang*, S. Bae*, J. Balakrishnan, F. Volmer, M. Jaiswal, Z. Yi, S. R. Ali, G. Güntherodt, B.-H. Hong,B. Beschoten and Barbaros Özyilmaz, "Toward Wafer Scale Fabrication of Graphene Based Spin Valve Devices", Nano Letters **11**, 2363 (2011).

4. S. Bae, H. Kim,Y. Lee, X. Xu, J.-S. Park, Y. Zheng, J. Balakrishnan, T. Lei, H. R. Kim, Y. I. Song, Y.-J. Kim, K. S. Kim, B. Özyilmaz , J.-H. Ahn, B. H. Hong and S. Iijima," Roll-to-roll production of 30-inch graphene films for transparent electrodes", Nature Nanotechnology **5**, 574 (2010).

5. Surajit Saha, Orhan Kahya, Manu Jaiswal, Amar Srivastava, Anil Annadi, Jayakumar Balakrishnan, Alexandre Pachoud, Chee-Tat Toh, Byung-Hee Hong,

Jong-Hyun Ahn, T. Venkatesan , and Barbaros Özyilmaz, "Anomalous field effect of graphene on $SrTiO_3$: A plausible effect of $SrTiO_3$ phase-transitions", manuscript under review (2013).

6. A. Avsar, J. Y. Tan, J. Balakrishnan, G. K. W. Koon, J. Lahiri, A. Carvalho, A. S. Rodin, T. Taychatanapat, G. Eda, A. H. Castro Neto, and B. Özyilmaz, "Spin-Orbit Proximity Effect in Graphene", manuscript under review (2013).

7. Jayakumar Balakrishnan*, Gavin Kok Wai Koon*,Ahmet Avsar, Yuda Ho, Jong Hak Lee, Manu Jaiswal, Seung-Jae Baeck, Jong-Hyun Ahn, Aires Ferreira, Miguel A. Cazalilla, A. H. Castro Neto, and Barbaros Özyilmaz, "Giant Spin Hall Effect in CVD Graphene", manuscript submitted (2013).